

DESIGN AND IMPLEMENTATION OF LOW LEAKAGE MEMS  
MICROVALVES

A THESIS SUBMITTED TO  
THE GRADUATE SCHOOL OF NATURAL AND APPLIED SCIENCES  
OF  
MIDDLE EAST TECHNICAL UNIVERSITY

BY

ENDER YILDIRIM

IN PARTIAL FULFILLMENT OF THE REQUIREMENTS  
FOR  
THE DEGREE OF DOCTOR OF PHILOSOPHY  
IN  
MECHANICAL ENGINEERING

SEPTEMBER 2011

Approval of the thesis:

**DESIGN AND IMPLEMENTATION OF LOW LEAKAGE  
MEMS MICROVALVES**

submitted by **ENDER YILDIRIM** in partial fulfillment of the requirements for the degree of **Doctor of Philosophy in Mechanical Engineering Department, Middle East Technical University** by,

Prof. Dr. Canan Özgen  
Dean, Graduate School of **Natural and Applied Sciences**

\_\_\_\_\_

Prof. Dr. Süha Oral  
Head of Department, **Mechanical Engineering**

\_\_\_\_\_

Prof. Dr. M. A. Sahir Arıkan  
Supervisor, **Mechanical Engineering Dept., METU**

\_\_\_\_\_

Assoc. Prof. Dr. Haluk Külâh  
Co-Supervisor, **Electrical and Electronics Eng. Dept., METU**

\_\_\_\_\_

**Examining Committee Members:**

Prof. Dr. Mustafa İ. Gökler  
Mechanical Engineering Dept., METU

\_\_\_\_\_

Prof. Dr. M. A. Sahir Arıkan  
Mechanical Engineering Dept., METU

\_\_\_\_\_

Prof. Dr. Tayfun Akın  
Electrical and Electronics Eng. Dept., METU

\_\_\_\_\_

Prof. Dr. Can Çoğun  
Mechanical Engineering Dept., METU

\_\_\_\_\_

Asst. Prof. Dr. Şenol Mutlu  
Electrical and Electronics Eng. Dept., Boğaziçi University

\_\_\_\_\_

Date: 16 September 2011

**I hereby declare that all information in this document has been obtained and presented in accordance with academic rules and ethical conduct. I also declare that, as required by these rules and conduct, I have fully cited and referenced all material and results that are not original to this work.**

Name, Last name : Ender Yıldırım

Signature :

# ABSTRACT

## DESIGN AND IMPLEMENTATION OF LOW LEAKAGE MEMS MICROVALVES

Yıldırım, Ender

Ph.D., Department of Mechanical Engineering

Supervisor: Prof. Dr. M. A. Sahir Arıkan

Co-Supervisor: Assoc. Prof. Dr. Haluk K ulah

September 2011, 139 pages

This thesis presents analysis, design, implementation, and testing of electrostatically actuated MEMS microvalves. The microvalves are specifically designed for lab-on-a-chip applications to achieve leakage ratios below 0.1 at pressure levels in the order of  $10^1$  kPa.

For this purpose, two different microvalves are presented in the study. In the proposed designs, electrostatic actuation scheme is utilized to operate the microvalves in normally open and normally closed modes. Characterization of normally open microvalves show that, microvalves with radii ranging between 250  $\mu\text{m}$  and 450  $\mu\text{m}$  can be operated by applying voltages between 40 and 100 V with air and oil. It is also shown that the actuation potential becomes minimum for working fluids with dielectric constant around 3-5. During the tests, it could not be possible to operate normally open electrostatic microvalves with DI water, due to its high dielectric constant and conductivity. During flow tests with air, 17 % leakage is observed under 10 kPa inlet pressure, when actuated by applying 85 V. On the other hand, it is shown that this leakage can be controlled precisely by tuning the actuation potential with sensitivity of  $10^{-3} \text{ V}^{-1}$ .

To solve the problems observed in normally open microvalve, a normally closed electrostatic microvalve design is proposed. The design isolates the working fluid from electric field, hence makes it possible to operate the microvalve with any working fluid. Moreover, unique and reconfigurable valve seat design enables low leakage. Pull-in tests are carried out with air and DI water under no-flow condition. During the tests, 46-66 V pull-in voltage is observed, independent of the working fluid. Besides, during flow tests with DI water, no leakage is detected up to 20 kPa inlet pressure.

Considering actuation and leakage properties of these microvalves, a multi-drug effect analysis system is proposed. The system utilizes normally closed microvalves to generate micro-droplets of different drug with cells entrapped inside. Prototypes of the system are fabricated and tested with 3  $\mu\text{m}$  diameter polystyrene micro-beads. The tests show that it can be possible to entrap single bead in 135 pL volume droplets. The prototypes are also tested with living yeast cells. It could also be possible to entrap yeast cells in micro-droplets using the proposed system.

As an extension to the multi-drug effect analysis system, a microvalve controlled droplet metering technique is proposed. The technique uses normally open microvalves to control the flow rate of the carrier fluid in a droplet based system. Initial tests show that it can be possible to generate pL size micro-droplets with 6 % precision. During the tests, voltage sensitivity of the technique is measured as 0.4 pL/V.

**Keywords:** Microvalve, Electrostatic actuation, Microelectromechanical Systems (MEMS), Parylene-C, Lab-on-a-Chip, Droplet Microfluidics

## ÖZ

### DÜŞÜK SIZDIRMALI MEMS MİKROKAPAKLARIN TASARIMI VE GERÇEKLEŞTİRİLMESİ

Yıldırım, Ender

Doktora, Makina Mühendisliği Bölümü

Tez Yöneticisi: Prof. Dr. M. A. Sahir Arıkan

Ortak Tez Yöneticisi: Doç. Dr. Haluk Külâh

Eylül 2011, 139 sayfa

Bu tez elektrostatik tahrikli MEMS mikrokapakların analizini, tasarımını, gerçekleştirilmesini ve test edilmesini sunmaktadır. Mikrokapaklar özellikle çip-üstü-laboratuvar uygulamalarında,  $10^1$  kPa mertebesindeki basınç seviyelerinde 0.1'in altında sızdırma oranı sağlamak için tasarlanmıştır.

Bu amaçla, bu çalışmada iki farklı mikrokapak sunulmuştur. Önerilen tasarımlarda, mikrokapakları normalde açık ve normalde kapalı modlarda çalıştırmak için elektrostatik tahrik yöntemi kullanılmıştır. Normalde açık mikrokapakların karakterizasyonu sonucunda, yarıçapları 250  $\mu\text{m}$  ile 450  $\mu\text{m}$  arasında değişen mikrokapakların, hava ve yağ ortamında 40 ile 100 V arasında voltaj uygulanarak çalıştırılabileceği gösterilmiştir. Ayrıca, tahrik voltajının dielektrik sabiti 3-5 arasında olan çalışma sıvılarında en aza indiği gösterilmiştir. Testler sırasında, normalde açık elektrostatik mikrokapakları, yüksek dielektrik sabiti ve iletkenliği nedeniyle, deiyonize su ile çalıştırmak mümkün olmamıştır. Hava ile yapılan akış testlerinde, 10 kPa giriş basıncı altında, 85 V tahrik voltajı uygulanarak % 17 sızdırma gözlenmiştir. Diğer yandan, bu sızdırma miktarının tahrik voltajı ayarlanarak  $10^{-3} \text{ V}^{-1}$  hassasiyetle kontrol edilebileceği gösterilmiştir.

Normalde açık mikrokapakta gözlenen problemlerin çözümü için, normalde kapalı elektrostatik mikrokapak tasarımı önerilmiştir. Tasarım, çalışma sıvısını elektrik alandan yalıtması nedeniyle, mikrokapagın herhangi bir sıvı ile çalışmasını mümkün kılmaktadır. Ayrıca, özgün ve yeniden ayarlanabilir yatak tasarımı düşük sızdırma oranlarını mümkün kılmaktadır. Hava ve deiyonize su ile akış olmayan ortamda yapılan pull-in testlerinde, çalışma sıvısından bağımsız olarak, 46-66 V arasında pull-in voltajı gözlenmiştir. Bunun yanısıra, deiyonize su ile yapılan akış testlerinde, 20 kPa giriş basıncına kadar sızdırma kaydedilmemiştir.

Bu mikrokapakların çalışma ve sızdırma özellikleri göz önünde bulundurularak bir çoklu ilaç etkisi araştırma sistemi önerilmiştir. Sistem, farklı ilaçlardan oluşan ve içinde hücre hapsedilmiş olan mikro-damlacıklar oluşturmak için normalde kapalı mikrokapakları kullanmaktadır. Sistemin prototipleri üretilmiş ve 3 µm çaplı polystyrene mikro-tanecikler kullanılarak test edilmiştir. Testler, 135 pl hacimli damlacıklar içinde tek bir tanecik hapsedilmenin mümkün olduğunu göstermiştir. Prototipler canlı maya hücreleriyle de test edilmiştir. Önerilen sistem kullanılarak mikro damlacıklar içinde maya hücresinin hapsedilmesi de sağlanmıştır.

Çoklu ilaç etkisi araştırma sisteminin bir uzantısı olarak, mikrokapak kontrollü damlacık ölçüm tekniği önerilmiştir. Teknik normalde açık mikrokapakları, damlacık tabanlı bir sistemde taşıyıcı sıvının hızını kontrol etmek için kullanmaktadır. İlk testler % 6 hassaslıkta pl hacimli damlacıkların oluşturulabileceğini göstermiştir. Testler sırasında tekniğin voltaj duyarlılığı 0.4 pl/V olarak ölçülmüştür.

**Anahtar Kelimeler:** Mikrokapak, Elektrostatik tahrik, Mikro elektromekanik Sistemler (MEMS), Parylene-C, Çip-üstü-laboratuvar, Damlacık tabanlı mikro akış

*To my wife*  
*and*  
*In memory of my dearest mother*



## ACKNOWLEDGEMENTS

I would like to thank to my supervisor Prof. Dr. M. A. Sahir Arıkan for his guidance, support, and comments throughout the study. I am grateful to my co-supervisor Assoc. Prof. Dr. Haluk Klah for his invaluable guidance not only for the success of this study but also for a broad vision in my academic life. I had definitely learned much from him.

My sincere gratitude is for METU-MEMS staff for their support during fabrication. I specially thank to Orhan Akar for his endless effort and support in fabrication. I would also thank to members of BioMEMS and PowerMEMS research groups for sharing their valuable working hours with me. My sincere thanks are for my friends and former BioMEMS group members Grkan Yılmaz and Ekrem Bayraktar for the valuable discussions on design and their mentoring in fabrication. I would also like to thank Aziz Koyuncuođlu for his help in fabrication during early stages of this study. I also thank to Hatice Ceylan Koydemir for proof reading of the final copy of this thesis.

I am also grateful to Prof. Dr. Levent Kandiller for his never ending support during this study. This study may not come to an end without his efforts to provide the best circumstances. I also thank to Prof. Dr. Nevzat Onur for his patience especially in the late periods of the study.

I would also thank to my mother in law, Rahime Aslan at least for her great meals. I would also like to thank my great family for their support, even if they are not with me. I am grateful to my parents Raziye Yıldıırım and Mustafa Yıldıırım for their endless patience, love, and support throughout my life. They even supported me at the expense of their health, which I can never recover.

Finally, I would like to thank to my dear wife Miray Hanım Yıldırım for her invaluable patience and endless love, which made everything possible.

This study is supported by the Scientific and Technological Research Council of Turkey (TÜBİTAK) with scholarship. A part of this study is supported by the Scientific and Technological Research Council of Turkey (TÜBİTAK) with the grant number 111E110.

## TABLE OF CONTENTS

ABSTRACT .....	iv
ÖZ .....	vi
ACKNOWLEDGEMENTS .....	ix
TABLE OF CONTENTS .....	xi
LIST OF TABLES .....	xiv
LIST OF FIGURES .....	xv
CHAPTERS	
1. INTRODUCTION .....	1
1.1 Review of Microvalves .....	4
1.1.1 Electromagnetic Microvalves.....	6
1.1.2 Piezoelectric Microvalves .....	7
1.1.3 Electrothermal Microvalves .....	7
1.1.4 Pneumatic Microvalves.....	8
1.1.5 Electrostatic Microvalves.....	9
1.2 Objective of the Thesis .....	11
1.3 Organization of the Thesis .....	13
2. A NORMALLY OPEN ELECTROSTATIC MICROVALVE.....	15

2.1	Operation Principle of the Microvalve .....	15
2.2	Analysis of the Microvalve .....	18
2.3	Fabrication of the Microvalves.....	35
2.3.1	Fabrication Process Flow .....	35
2.4	Characterization of the Microvalves.....	41
2.5	Conclusion.....	49
3.	A NORMALLY CLOSED ELECTROSTATIC MICROVALVE.....	50
3.1	Operating Principle of the Microvalve .....	50
3.2	Design of the Microvalve.....	52
3.3	Fabrication of the Microvalves.....	66
3.3.1	Fabrication Process Flow .....	67
3.4	Characterization of the Microvalves.....	71
3.5	Conclusion.....	78
4.	POTENTIAL APPLICATIONS OF THE MICROVALVES IN LAB-ON-A-CHIP .....	81
4.1	Droplet Based Microfluidics and LOC applications .....	82
4.2	Electrostatic Microvalve Controlled Multi-Drug Effect Analysis System ..	85
4.3	Electrostatic Microvalve Controlled Droplet Metering System.....	92
4.4	Conclusion.....	98
5.	CONCLUDING REMARKS AND FUTURE WORK .....	99
	REFERENCES .....	105

## APPENDICES

A. MASK LAYOUTS.....	120
B. FABRICATION PROCESS RECIPES .....	127
CURRICULUM VITAE .....	138

## LIST OF TABLES

### TABLES

Table 1.1: Summary of operation principles and properties of earlier microvalves. .12	
Table 2.1: Parameters involved in the analysis of normally open electrostatic microvalve. ....20	
Table 2.2: Pull-in test results compared with the theory.....42	
Table 3.1: Dimension variations of designed normally closed microvalves.....66	
Table 3.2: Pull-in and pull-out voltages measured for different diaphragms.....74	
Table 5.1: Main properties of the microvalves proposed in the thesis. ....100	

## LIST OF FIGURES

### FIGURES

Figure 1.1: A typical lab-on-a-chip configuration. There are sub-blocks connected through a network of in-plane microchannels. ....	2
Figure 1.2: Flow directions in in-plane and out-of-plane microvalves. ....	5
Figure 1.3: A typical out-of-plane electromagnetic microvalve. ....	6
Figure 1.4: A typical out-of-plane piezoelectric microvalve. ....	7
Figure 1.5: A typical out-of-plane thermopneumatic microvalve. ....	8
Figure 1.6: A typical out-of-plane pneumatic microvalve. ....	9
Figure 1.7: A typical out-of-plane electrostatic microvalve. ....	10
Figure 2.1: Structure and open/closed states of the normally open electrostatic microvalve. ....	16
Figure 2.2: Parallel plates electrostatic actuator. ....	18
Figure 2.3: Geometrical parameters involved in the analysis and the capacitive structure of normally open electrostatic microvalve. ....	20
Figure 2.4: Solid model of the microvalve showing the boundary conditions. ....	23
Figure 2.5: Diaphragm deflection and velocity field solved at 0 V actuation potential. Diaphragm radius and inlet pressure are 250 $\mu\text{m}$ and 2 kPa respectively. ....	24
Figure 2.6: Diaphragm deflection and velocity field solved at pull-in. Diaphragm radius and inlet pressure are 250 $\mu\text{m}$ and 2 kPa respectively. ....	25
Figure 2.7: Flow chart illustrating the solution procedure. ....	26

Figure 2.8: Total CPU time and convergence of the flow rate ( $V_a = 0$ V, $p_{in} = 2$ kPa) versus the number of elements. ....	26
Figure 2.9: Normalized flow rate versus the actuation potential for (a) air and (b) oil at different inlet pressures. Back pressure is assumed to be zero.....	28
Figure 2.10: Pull-in voltage versus the inlet pressure for air and oil as the working fluids. Dotted lines indicate the linearity between pull-in voltage and inlet pressure. ....	29
Figure 2.11: Flow rate versus the inlet pressure for different actuation potentials. Back pressure is assumed to be zero. Working fluid is air. ....	29
Figure 2.12: Pull-in voltage versus dielectric constant for different inlet pressures. Back pressure is assumed to be zero.....	30
Figure 2.13: EDL formation in the microvalve and corresponding voltage change across the channel. ....	31
Figure 2.14: Equivalent circuit model of the microvalve with EDL. $C_p$ is the capacitance of the parylene diaphragm, $C_{EDL}$ is the capacitance of the electric double layer, $R_f$ is the electrical resistance of the liquid, $C_f$ is the capacitance of the bulk liquid. ....	32
Figure 2.15: Stress distribution on 250 $\mu$ m radius microvalve actuated by 200 V potential.....	34
Figure 2.16: Design dimensions of the normally open electrostatic microvalve. ....	34
Figure 2.17: Layout of the microvalve characterization prototype. ....	36
Figure 2.18: Illustration of the fabrication processes. Top view and the cross-section of a single prototype are shown.....	37
Figure 2.19: Chemical structure of common types of parylene [101]. ....	37



Figure 2.20: Parylene swelling problem. Micrographs show two cases: (a) insufficiently baked photoresist (b) properly baked photoresist. ....	39
Figure 2.21: 3D map of the normally open electrostatic microvalve obtained using Veeco Wyko NT1000 optical profiler. ....	39
Figure 2.22: Process wafer before parylene RIE step. Close-up view of a single prototype and micrograph of the microvalve are shown.....	41
Figure 2.23: Illustration of pull-in test setup.....	42
Figure 2.24: Prototype with microfluidic port mounted. ....	43
Figure 2.25: Pull-in voltage versus the inlet pressure for 250 $\mu\text{m}$ radius microvalves. Working fluid is air. Dash line denotes the curve fitted to data. ....	44
Figure 2.26: (a) Schematic drawing of the flow test setup. (b) Implemented flow test setup. ....	45
Figure 2.27: Illustration of the flow rate measurement method. Data are plotted for inlet pressure and actuation potential of 6 kPa and 0 V respectively. ....	46
Figure 2.28: Flow rate at different inlet pressures in open ( $V_a = 0\text{ V}$ ) and closed ( $V_a = 85\text{ V}$ ) states of the microvalve.....	47
Figure 2.29: Flow rate at different actuation potentials at 8 kPa inlet pressure for 250 $\mu\text{m}$ radius microvalve. ....	47
Figure 2.30: (a) Snapshots of the microvalve taken at different actuation potentials and corresponding 3D maps. (b) Width of the leakage path versus the actuation potential. ....	48
Figure 3.1: Structure and open/closed states of the normally closed electrostatic microvalve. ....	51
Figure 3.2: Illustration of the actuation potential. ....	52

Figure 3.3: Parameters affecting the operation of the normally closed microvalve. ...	53
Figure 3.4: Equivalent diaphragm approach. Fluidic pressure and the electrostatic load on the original diaphragm are shown at the top and at the bottom of the original diaphragm respectively. ....	54
Figure 3.5: Projected area underneath the semi-circular wall in open and closed states.....	56
Figure 3.6: Approximation of the fluidic pressure on the diaphragm. ....	57
Figure 3.7: Deflection profile of the diaphragm caused by the fluidic pressure. ....	58
Figure 3.8: Boundary definitions in finite element analysis of normally closed microvalve diaphragm.....	59
Figure 3.9: Diaphragm deflection in (a) closed and (b) open states of the microvalve. Diaphragm radius, semi-circular wall radius, and inlet pressure are 300 $\mu\text{m}$ , 240 $\mu\text{m}$ , and 10 kPa respectively. Height of the actuation chamber is 5 $\mu\text{m}$ .....	60
Figure 3.10: Projected deflection in closed and open states of the microvalve. Diaphragm radius, semi-circular wall radius, and inlet pressure are 300 $\mu\text{m}$ , 240 $\mu\text{m}$ , and 10 kPa respectively. Height of the actuation chamber is 5 $\mu\text{m}$ .....	61
Figure 3.11: Leakage ratio computed using (a) approximate deflection model and (b) finite element analysis.....	62
Figure 3.12: Contour plot of AOF for different inlet pressure levels. ....	64
Figure 3.13: Contour plot of AOF for different relative weights of objectives. ....	64
Figure 3.14: Top view of the microvalves with spiral and full top electrodes.....	65
Figure 3.15: Design dimensions of the normally closed electrostatic microvalve. ....	65
Figure 3.16: Layout of the microvalve characterization prototype. ....	67

Figure 3.17: Fabrication flow of the normally closed microvalves. ....	68
Figure 3.18: SEM image of the actuation chamber showing tapered side wall. ....	69
Figure 3.19: Surface profile of the actuation chamber and filling photoresist layer measured used Veeco Dektak 8 profiler. ....	70
Figure 3.20: Process wafer before parylene RIE step. Close-up view of a single prototype and micrograph of the microvalve are shown. ....	71
Figure 3.21: Snapshots of the microvalve at different actuation potentials. Dashed circle denotes the touch area after pull-in. Diaphragm radius and semi-circular wall radius are 410 $\mu\text{m}$ and 350 $\mu\text{m}$ respectively. ....	72
Figure 3.22: Change in the touch area versus the actuation potential for the microvalve with 410 $\mu\text{m}$ radius diaphragm. Horizontal dashed line denotes the radius of the semi-circular wall. ....	73
Figure 3.23: Illustration of the test setup used for leakage characterization of normally closed microvalves. ....	75
Figure 3.24: Prototype with the port mounted at the inlet, ready for leakage tests. ...	75
Figure 3.25: Leakage ratio measured at different inlet pressure levels for 20 kPa capacity microvalves. ....	76
Figure 3.26: Revised setup used for investigation of dynamic response of the microvalve. ....	77
Figure 3.27: Response of the microvalve to actuation potential. Inlet pressure is 2 kPa, open flow rate is 100 nl/min. ....	78
Figure 3.28: Leakage rate measured for different semi-circular wall radii. Diaphragm radius is 300 $\mu\text{m}$ . ....	79
Figure 4.1: T, Y, and cross junction configurations to generate droplets. ....	83

Figure 4.2: Effect of $Ca$ and flow speed on droplet formation. $w_f$ denotes water fraction (ratio of flow speed of water to total flow speed) [109]. .....	83
Figure 4.3: Screening of protein crystallization [110]. Varying flow rate of NaCl changes the concentration inside the droplet.....	84
Figure 4.4: Drug effect screening system proposed by Gong et al. [5]. .....	84
Figure 4.5: Microwell plate approach. ....	86
Figure 4.6: Illustration of the drug effect analysis system.....	88
Figure 4.7: Fabricated prototype of the drug effect analysis system. ....	88
Figure 4.8: Setup used for testing of drug effect analysis device. ....	89
Figure 4.9: (a) Open and closed states of the microvalves. Figures are colorized for clarity. (b) Droplets in serpentine channel and microbead entrapped in a droplet. ...	90
Figure 4.10: Monodisperse droplets in the microchannel and single micro-bead entrapped in the droplet.....	90
Figure 4.11: Yeast cell entrapped in the droplet and close up view of the cells. ....	91
Figure 4.12: Modification proposed for the Y-junction.....	92
Figure 4.13: Proposed droplet metering system using normally open electrostatic microvalve. ....	93
Figure 4.14: Fabricated droplet metering system prototype. ....	94
Figure 4.14: Illustration of the test setup for droplet metering system. ....	94
Figure 4.16: Top views of the microvalve and generated plugs at different actuation potentials. ....	95

Figure 4.17: Droplet volume versus the actuation potential. ....96

Figure 4.18: Droplet formation simulated using T, Y, and cross junctions. ....97

# CHAPTER 1

## INTRODUCTION

Micro Electromechanical Systems (MEMS) is an attractive field of study especially for the last decades. Over decades, MEMS technology led a way to miniaturization of existing systems or devices. One distinct application is the miniaturization of the systems used in life sciences. The concept is first introduced by Manz et al. [1] in 1990. According to Manz, chemical or biological analyses carried out in a laboratory can be integrated on miniature systems, termed as Miniaturized Total Analysis Systems ( $\mu$ TAS). The term lab-on-a-chip (LOC) is sometimes used replacing  $\mu$ TAS. Although  $\mu$ TAS or LOC concept was firstly discussed in 1990, there were earlier attempts to carry out chip-level biological or chemical analyses. For instance, Shoji et al. [2] had presented an on-chip blood gas analyzer in 1988. However, it was only after 1990 when studies on  $\mu$ TAS had a tremendous jump. Today, various systems have been developed to carry out enzyme/cell assays [3-12], genomic and proteomic analyses [13-21] on chip level.

Such systems commonly rely on flow of chemical reagents or body fluids in micro-scaled channels (generally rectangular channels in the order of 10s of microns in height and width) on a chip. In a complete LOC, common unit operations including reagent transport, mixing, metering, separation, amplification, and detection [22] should be carried out in a network of microchannels on a single chip. Figure 1.1 shows a typical LOC configuration, depicting the unit operations. On the other hand, most of the applications presented so far are limited to design and development of only separation [23-26], amplification [16, 21, 27], or detection [28, 29] techniques. The integration of these unit operations can be possible by on-chip valves and pumps, which enable control on the flow of the reagents. In 2000, Unger et al. [30]

proposed a pneumatically operated platform for large scale microfluidic integration. After then, various integrated LOCs emerged.

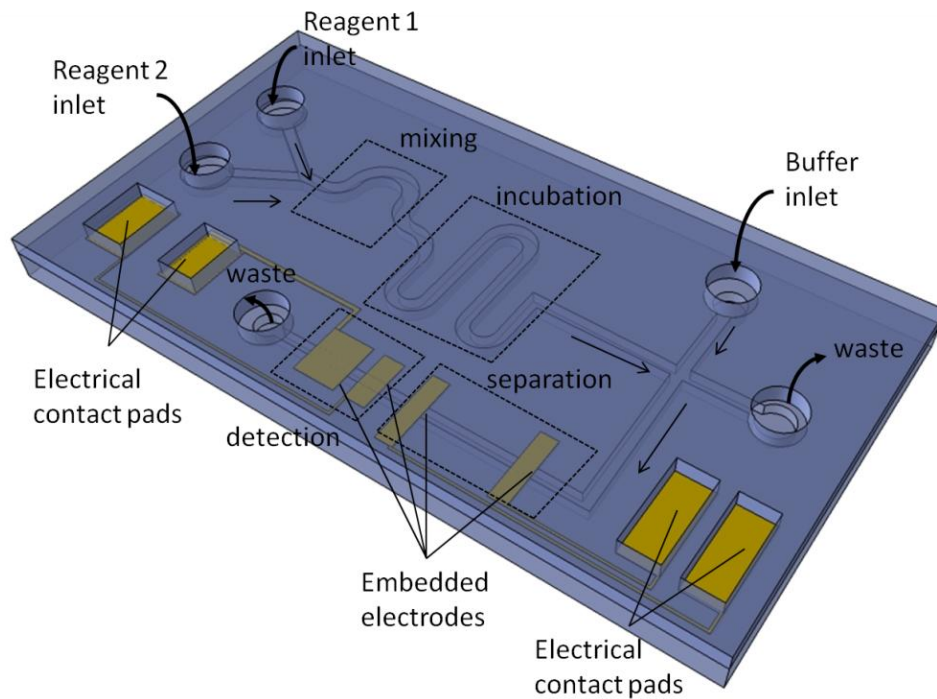


**Figure 1.1: A typical lab-on-a-chip configuration. There are sub-blocks connected through a network of in-plane microchannels.**

Although there are other integration technologies such as electrowetting on dielectric (EWOD) [31, 32] that do not require a valve; or centrifugal microfluidic platforms that use passive valves [33-35], most of the LOCs demand for active microvalves for integration. The challenge here is in the design of simple yet effective microvalves. Today, many integrated LOC systems or platforms make use of pneumatically operated microvalves [36-39]. Although these microvalves are reliable in terms of performance, they require external high-pressure sources, solenoid control valves, and off-chip pneumatic connections.

In addition to the operating principles, flow direction is another limitation of design of microvalves. Revisiting Figure 1 reveals that microchannel network on a typical LOC lays on the same plane. Therefore, a microvalve to serve in LOCs should be co-planar with the microchannels for ease of integration. Moreover, the microvalve should provide low or zero leakage at its closed state in order to control the flow of the reagents. There are many microvalves, which provide very low or zero leakage. However, most of these are complicated out-of-plane designs [40-43]. Providing low leakage is therefore another challenge in the design of in-plane microvalve.

Another consideration in the microvalve design is the structural material. A microvalve to serve in LOC applications should be made of biocompatible materials. Additionally, this material should be transparent to facilitate detection, if optical means are used. Today, many of the LOC devices are fabricated using a biocompatible elastomer; polydimethylsiloxane (PDMS). Due to its high elasticity and suitability for rapid prototyping, PDMS is an attractive material in microfluidic biochemical applications. Although fabrication of PDMS based microfluidic devices is rapid [44], traditional PDMS microchannel fabrication is not fully compatible with micromachining techniques. Excluding its photo-definable versions [45, 46], PDMS cannot be patterned using standard micromachining techniques. This compatibility problem limits the design. Moreover, its relatively poor swelling properties in organic solvents and relatively high vapor permeability limit the applications. To figure out the permeability problem, it is proposed to coat PDMS with a thin layer of another polymer, which is poly-paraxylylene (parylene) [47, 48]. Parylene is a biocompatible, transparent, and inert polymer [49] with comparably low vapor permeability [47]. This makes parylene an interesting material for life sciences. Additionally, parylene can be coated conformably with vapor deposition process, which is compatible with surface micromachining techniques. This property improves the flexibility in microvalve design.

Regarding aforementioned considerations, existing microvalves in the literature are explained in the following section.



## 1.1 Review of Microvalves

Microvalves are microfluidic components used for regulating the flow by fully or partly allowing or preventing the flow along microchannels. Depending on the application, microvalves can be either active or passive. Active microvalves require an external source for powering, while the passive microvalves do not require powering. In an active microvalve, the external source can be an electrical power supply or a vacuum pump. Commonly these sources are used to deflect a membrane or a flap against a seat to actuate the microvalve. There are various actuation schemes to deflect the moving element of the microvalve such as electromagnetic [50-52], piezoelectric [43, 53, 54], electrothermal [40, 55-59], electrostatic [41, 60-64], and pneumatic [37, 65-68]. Such microvalves can be classified as mechanical active microvalves [69]. On the other hand, there are active microvalves, which do not involve any moving element. These microvalves can be operated by modifying the rheological properties of the working fluid [70] or by electrochemical means [71] again using external power sources. These microvalves can be classified as non-mechanical active microvalves [69].

The passive microvalves can also be classified as mechanical or non-mechanical [69]. Similar to mechanical active microvalves, mechanical passive microvalves involve deflecting membranes or flaps and a valve seat. However, different from the mechanical active microvalves; the deflection is caused by the fluidic motion itself in mechanical passive microvalves. Hence, such microvalves are generally used as check valves [72-75], which allow flow in one direction, while preventing it in opposite direction. On the other hand, there are non-mechanical passive microvalves. In such microvalves, capillary forces can be used to regulate the motion of the fluid [76, 77]. There are also siphon valves [33], diffuser-nozzle type valves [78, 79], and Tesla type valves [80] used as check valves, which can also be classified as non-mechanical passive microvalves.

Active microvalves are the most vital ones for the integration as they enable on-demand operation of the units (separation, amplification, detection etc.) in LOCs. Among the active microvalves, non-mechanical ones depend heavily on the chemical

or rheological properties of the working fluid. Therefore, non-mechanical microvalves are more suitable for specific applications rather than integrated LOC platforms.

Apart from the actuation scheme, mechanical microvalves can also be classified regarding the flow direction. In a mechanical microvalve, if the deflecting membrane (or flap) is parallel to the flow direction, then the microvalve is in-plane. Otherwise, the microvalve is out-of-plane. Normally, out-of-plane microvalves involve an orifice, which is perpendicular to the flow. Figure 1.2 illustrates operation of representative in-plane and out-of-plane microvalves. As mentioned before, a microvalve designed for LOC applications should be in-plane for integration purposes.

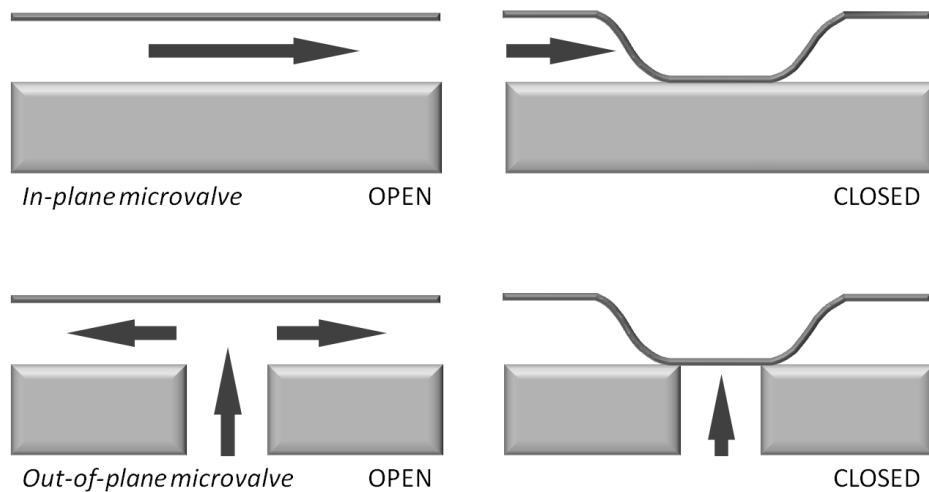


**Figure 1.2: Flow directions in in-plane and out-of-plane microvalves.**

Consequently, it can be stated that in-plane mechanical active microvalves will be at the focus of this study. In this section, mechanical active microvalves reported so far are reviewed based on the actuation schemes. The designs are discussed from feasibility point of view on LOC applications.

### 1.1.1 Electromagnetic Microvalves

Electromagnetic microvalves make use of electromagnetic forces acting on the deflecting element. In order to generate the forces, commonly a permanent magnet and a coil pair is used (Figure 1.3). When electrical current passes along the coil, electromagnetic field generates a force to pull the permanent magnet. Generally, it is possible to create sufficiently high forces and deflections by electromagnetic actuation. However, power consumption is relatively high [81].

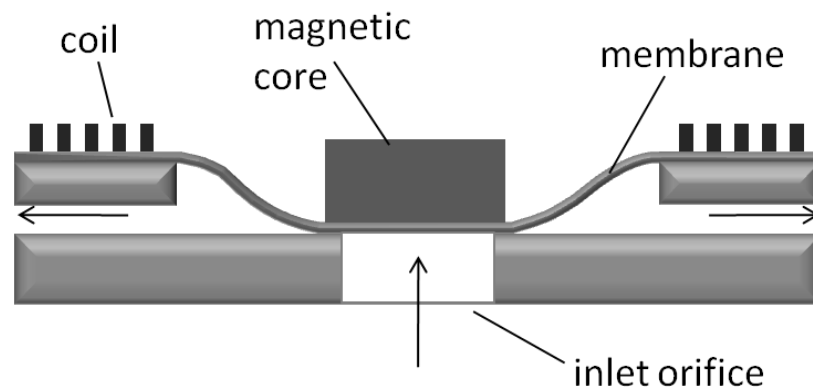


**Figure 1.3: A typical out-of-plane electromagnetic microvalve.**

An example of electromagnetically actuated microvalve was reported by Bintoro et al. [50]. In this design, there is a permanent magnet located on a tethered cover and an orifice underneath. Around the orifice, a magnetic coil is wound. As electrical current passes along the coil, an electromagnetic field is generated. Magnetic forces pull the tethered cover on the orifice closing the microvalve. Here, amplification of the magnetic field by using both coil and the permanent magnet allows relatively high deflection of the tethered cover. It is reported that the leakage under 30  $\mu\text{l}/\text{min}$  flow is between 0.16-0.8  $\mu\text{l}/\text{min}$  with an actuation power of 1.17 W. Although it is possible to obtain leakage ratio as low as 0.5 % with this design, its out-of-plane structure makes it impractical for LOC applications.

### 1.1.2 Piezoelectric Microvalves

Diaphragm or the flap of a mechanical microvalve can also be deflected by using piezoelectricity. Application of electric potential on a piezoelectric material causes stresses on it. If a piezoelectric material is placed on the diaphragm or flap of the microvalve, it can be possible to deflect it by applying voltage (Figure 1.4). In general, power consumption of piezoelectric actuation is lower than that of electromagnetic actuation [81]. In addition, it can be possible to obtain high deflections.

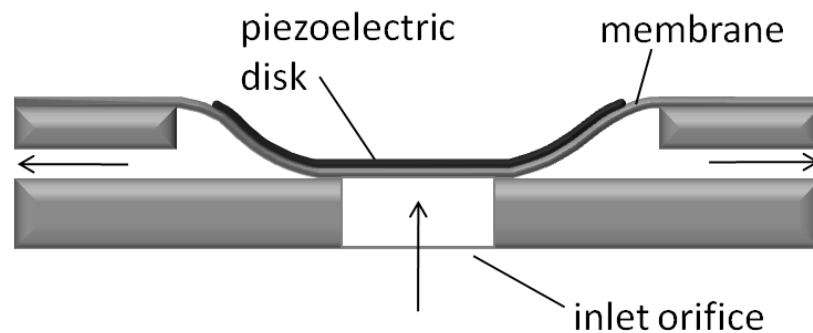


**Figure 1.4: A typical out-of-plane piezoelectric microvalve.**

Doll et al. presented a piezoelectrically actuated microvalve [53]. In this design, a pressed lead zirconate titanate (PZT) disk is placed on top of a silicon membrane. When potential is applied on PZT disk, it deflects the membrane to seat on a circular orifice. However, this is also an out-of-plane microvalve, which makes it impractical for LOC applications.

### 1.1.3 Electrothermal Microvalves

Electrothermal actuation makes use of heat generation through passing electrical current along resistive heaters. This heat can be used to expand air in a chamber closed by diaphragm. The expansion would cause deflection of the diaphragm (Figure 1.5). This scheme is specifically called thermopneumatic actuation and can

be used for operating microvalves [40, 82, 83]. Another electrothermal actuation scheme is based on phase change of materials, which exploit large volumetric expansion during melting. Such materials are sealed by an elastic membrane and heated through resistive elements. Rapid melting of the material causes deflection of the membrane. The membrane deflection can be used to operate microvalves. Common material in such microvalves is paraffin, which shows 10-30 % volume expansion through melting [84]. There are microvalves reported, which utilizes this principle [56, 84].

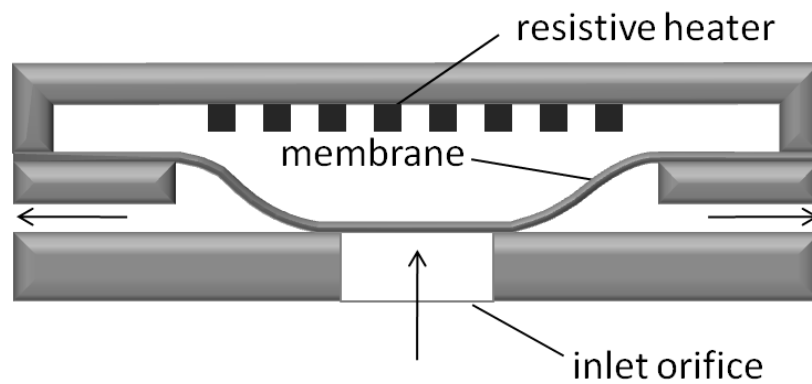


**Figure 1.5: A typical out-of-plane thermopneumatic microvalve.**

It is possible to operate electrothermal microvalves with powers as low as few tens of mWs [56]. However, the response time of these microvalves is generally long (up to tens of seconds) [56].

#### ***1.1.4 Pneumatic Microvalves***

Another method to operate mechanical microvalves is pneumatic actuation. Pneumatic actuation requires external compressed air or vacuum source to deflect the movable member of the microvalve (Figure 1.6). Pneumatic microvalves are preferred so far in LOC applications due to their robustness, compatibility with especially PDMS fabrication methods, and low leakage properties.

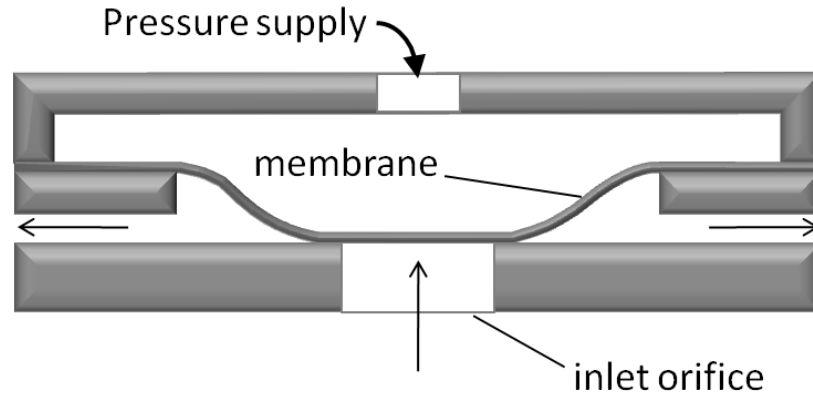


**Figure 1.6: A typical out-of-plane pneumatic microvalve.**

The first pneumatic microvalve for LOC applications was proposed by Unger et al. [30]. In this design, two microchannels (one of which is the active channel, the other is the manifold channel) are located on top of each other. As compressed air is supplied through the manifold channel, the membrane between overlapping channels deflect, squeezing the active channel. A similar design was proposed by Go and Shoji [68]. Here a dome shape membrane is utilized between overlapping channels to improve leakage properties. Grover et al. also proposed a pneumatic microvalve [37] for LOC applications. Different from the previous designs, the structure proposed by Grover et al. requires vacuum to actuate the normally closed valve. A similar structure was also used by Hosokawa and Maeda as a three way microvalve [66].

Although pneumatic microvalves seem to be a powerful tool for integration of PDMS based LOCs today, requirement of external pressure sources and control equipment, and extra off-chip connections for manifold channels limit the applications.

### ***1.1.5 Electrostatic Microvalves***

In electrostatic microvalves, the diaphragm or the flap is deflected via electrostatic forces. The forces are created by applying voltage across the deflecting member and

a counter electrode. Electrical charge on opposing electrodes results in attraction force bending the membrane or the flap onto the counter electrode (Figure 1.7).

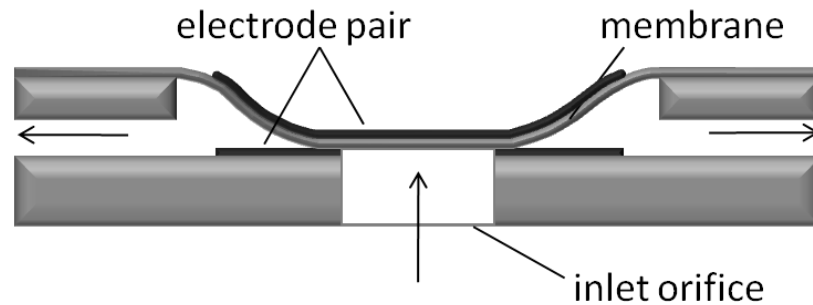


**Figure 1.7: A typical out-of-plane electrostatic microvalve.**

Probably the most important advantage of electrostatic actuation is the ease of implementation. The method requires only two opposing electrodes, which can be easily created by well-known surface micromachining techniques. However, the forces and the amount of deflection are relatively low compared to other actuation methods. Hence, the method is generally used in out-of-plane microvalves where opposing fluidic force can be reduced significantly by decreasing the radius of the orifice. A simple out-of-plane microvalve design was proposed by Dubois et al. [85]. Here, a tethered membrane is electrostatically pulled on to an inlet orifice. In the design, the length of the tethers is kept long to minimize the elastic restoring force. Additionally, the gap between the orifice and the membrane is kept low to maximize the electrostatic forces.

In the design proposed by van de Wijngaart et al., fluidic pressure is suppressed to dominate the effect of the electrostatic force [61]. As a result, an improved deflection could be obtained. Sometimes electrostatic actuation is coupled with other schemes, such as electromagnetic or electrothermal, in order to increase the actuation force [86, 87].

Another problem with electrostatic actuation is related with implementation of the method in liquid media. This problem is especially important in LOC, where the working fluids are generally body liquids (such as blood or plasma) or chemical reagents. In this case, electrostatic actuation may lead to electrolysis of the working fluid, screening of the actuation electrodes by formation of electric double layer [88], or degradation of the biological material in the stream. Application of high frequency ac potential is proposed as a solution for this problem [88]. Chang and Maharbiz previously designed an in-plane electrostatically actuated microvalve for LOC applications [64]. However, the leakage was reported as a problem [64].

Considering the properties and actuation principles, a wide range of microvalves are reported up to now. Actuation principles, operation modes, and flow properties of some of these microvalves are tabulated in Table 1.1. Examining Table 1.1 reveals that especially electromagnetic actuation requires high actuation powers. In thermopneumatic microvalves, actuation power is reduced compared to electromagnetic actuation. However, power requirement is still in the order of  $10^2$  mWs. For the pneumatic microvalves, considering the need for external pumping units, actuation power is also high. As a result, electrostatic actuation is considered to be the proper actuation method for the microvalves. However, there are still challenges to cope with in electrostatic actuation, as mentioned above.

## **1.2 Objective of the Thesis**

The aim of the thesis study is to design, implement, and characterize MEMS based simply actuated, low leakage, and in-plane microvalves considering the needs of LOC applications. Comparing different actuation schemes, electrostatic actuation is decided to be used as it eliminates the need for off-chip pneumatic connections for operation, facilitates integration of LOCs with on-chip electronics, and decreases the power consumption. For the designed microvalves, parylene is selected as the structural material, considering the facts mentioned before. On the other hand, this decision introduces some major challenges such as the problems with electrostatic actuation in liquid media and providing low leakage at intended pressure levels with an in-plane structure.



**Table 1.1: Summary of operation principles and properties of earlier microvalves.**

Reference	Actuation principle	Valve orientation	Mode	On/off supply	Working fluid	Flow properties
Bintoro et al. [50]	EM	out-of-plane	NO	0.38 A, 1.17 W	Water	0.16-0.8 $\mu\text{l}/\text{min}$ leakage over 30 $\mu\text{l}/\text{min}$
Rich et al. [40]	TP	out-of-plane	NO	350 mW at 1000 torr	Air	$10^{-3}$ sccm leakage over 400 sccm
Carlen et al. [84]	TP	in-plane	NO	50-150 mW	Air	500 $\mu\text{sccm}$
Unger et al. [30]	P	in-plane	NO	40 kPa	Water	-
Grover et al. [37]	P	in-plane	NC	45 kPa to close / -20 kPa to open	Water	-
Dubois et al. [85]	ES	out-of-plane	NO	30 V	Nitrogen	1/1600 leakage ratio
van de Wijngaart et al. [61]	ES	out-of-plane	NO	24 V at 100 kPa	Air	-
Chang and Maharbiz [64]	ES	in-plane	NO	15-20 V at 5 MHz	Water	-

EM: electromagnetic  
 TP: thermopneumatic  
 P: pneumatic  
 ES: electrostatic

NO: normally open  
 NC: normally closed

Based on the above discussions, the objectives of the study can be listed as:

1. Designing a MEMS based in-plane microvalve with low leakage under low pressure range ( $10^1 - 10^2$  kPa), which is the level in many LOC applications [89],
2. Manufacturing the microvalve using micromachining techniques,
3. Testing the operation of the valve, including voltage and flow characterization,
4. Implementing the valve on an LOC application for proof-of-concept.

In order to achieve these objectives, analysis, design, fabrication, and testing of a simple normally open microvalve are carried out. For the testing of the microvalves, a setup is designed and devised. These steps are crucial to gain experience on design and analysis tools, microfabrication methods, and testing. Based on this experience, a new microvalve concept is proposed and geometrical optimization of the new microvalve is done. This microvalve essentially solves the problems faced in the first design and satisfies the requirements stated above. Following this step, prototypes of the microvalve are fabricated and tested. During these steps, conceptual design of an LOC application utilizing the microvalves is proposed. After characterization of microvalves, initial design of proposed system is done. Fabricated proof-of-concept prototypes are tested to show the applicability of the microvalves in LOCs.

### **1.3 Organization of the Thesis**

In this chapter, brief information on LOC applications is given and microvalves in these applications are introduced. Additionally, a review of microvalves is presented with a focus on actuation schemes. Considering the ease of integration, electrostatic actuation is selected as the proper way to operate the microvalves in this thesis. In addition to different actuation methods, common materials used in LOC fabrication are discussed. Among these materials, parylene is selected as the suitable material considering mainly its fabrication compatibility. Also, the specifications of the microvalve to serve in LOC applications are set in this chapter.

The organization of the rest of this thesis is based on the methodology explained in the previous section. Chapter 2 covers analysis, fabrication, and characterization of a normally open microvalve, whose conceptual design was previously made in METU-MEMS Research and Application Center BioMEMS research group. Detailed analysis of the microvalve is explained in this chapter. Also, fabrication details and challenges are presented. Characterization results of the microvalve are given in Chapter 2. This chapter is concluded by a discussion on advantages and deficiencies of the microvalve.

Chapter 3 presents a novel normally closed microvalve design. Here, the operational principles and geometrical optimization of the design are presented. Fabrication of this microvalve is also explained in this chapter. A detailed characterization of this microvalve is carried out and the results are presented in this chapter. The chapter also includes a discussion on this design.

Chapter 4 discusses possible applications using the microvalves presented in chapters 2 and 3. Based on the discussions, a drug effect analysis system is designed and presented in chapter 4. Proof-of-concept testing of the system is given in this chapter to show the feasibility of the microvalves in LOC applications.

The last chapter finalizes the thesis with concluding remarks and recommendations on future studies.

## CHAPTER 2

### A NORMALLY OPEN ELECTROSTATIC MICROVALVE

In the previous chapter, the main focus was on the actuation principles and flow direction of the microvalve. Apart from these considerations, an active microvalve can be classified according to its normal state. An active microvalve can be normally open, and get closed when actuated, or can be normally closed and open when actuated. This chapter presents the analysis, fabrication, and characterization of an electrostatically actuated in-plane microvalve, which is monolithically fabricated on parylene microchannel.

The conceptual design of the normally open electrostatic microvalve was previously done in BioMEMS research group. In this thesis study, through analysis, fabrication, and characterization of the microvalve is done.

#### 2.1 Operation Principle of the Microvalve

Figure 2.1 shows the structure and open/closed states of the microvalve. The microvalve is formed by widening a rectangular microchannel, to form a circular diaphragm at the valve section. There are two actuating electrodes, one of which is located at the top of the diaphragm, and the other is located at the bottom. When electric potential is applied across these electrodes, electrostatic forces are generated on the diaphragm, pulling it down on the bottom. As the actuation potential exceeds a certain level (pull-in voltage) the diaphragm collapses on the bottom. Once the diaphragm collapses on the bottom of the channel, it obstructs the fluid flow. However, due to rigid side walls, the diaphragm does not collapse as a whole on the bottom. This results in a leakage path at the periphery. As the actuation potential is increased beyond pull-in, this leakage path narrows, decreasing the leakage flow.

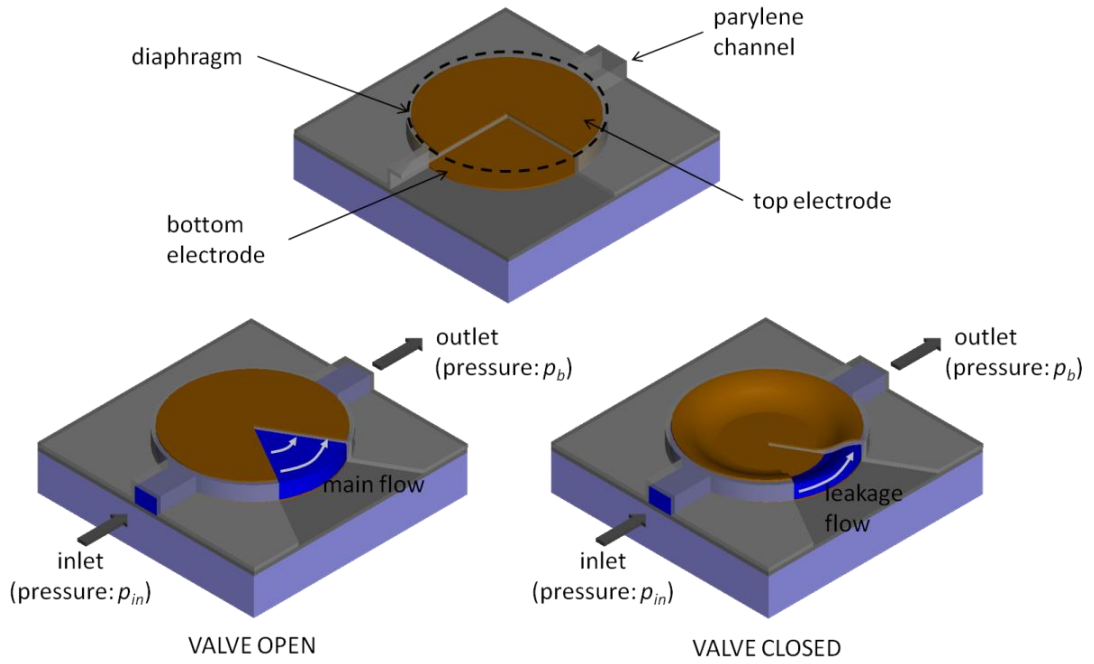


**Figure 2.1: Structure and open/closed states of the normally open electrostatic microvalve.**

Potential required to collapse the diaphragm is defined by the well-known phenomenon; pull-in. Pull-in is the sudden collapse of a compliant or spring-suspended electrode onto the fixed counter electrode under electrostatic loading. The phenomenon is often explained by parallel plate electrostatic actuation model (Figure 2.2). According to this model, static equilibrium of the suspended electrode requires

$$kx - F_e = 0 \quad (2.1)$$

where  $F_e$  is the electrostatic force on the suspended electrode and  $k$  is the stiffness of the spring. Here,  $F_e$  can be found as:

$$F_e = \frac{\varepsilon AV^2}{2(g_0 - x)^2} \quad (2.2)$$

where  $\varepsilon$  is the electric permittivity of the medium,  $A$  is the overlapping electrode area,  $V$  is the electric potential, and  $g_0$  is the initial gap between the electrodes.

Condition given in (2.1) is stable provided that the variation of the net force with respect to an increase in the displacement is negative (2.2).

$$\frac{\partial}{\partial x} \left( kx - \frac{\varepsilon AV^2}{2(g_0 - x)^2} \right) < 0 \quad (2.3)$$

The pull-in occurs at the boundary of this condition, where

$$\frac{\varepsilon AV^2}{g^3} - k = 0 \quad (2.4)$$

where  $g$  is the instantaneous gap between the electrodes ( $g_0 - x$ ). Electric potential satisfying (2.3) is defined as the pull-in voltage:

$$V_{pi} = \sqrt{\frac{kg^3}{\varepsilon A}} \quad (2.5)$$

At this unstable equilibrium point, (2.1) should also be satisfied. Using (2.1),  $g$  at pull-in can be found as:

$$g_{pi} = \frac{2}{3} g_0 \quad (2.6)$$

Therefore, pull-in voltage can be rewritten as:

$$V_{pi} = \sqrt{\frac{8kg_0^3}{27\varepsilon A}} \quad (2.7)$$

This analysis can be modified to find the voltage to pull down the diaphragm shown in Figure 2.1. The details of the analysis are presented in the following section.

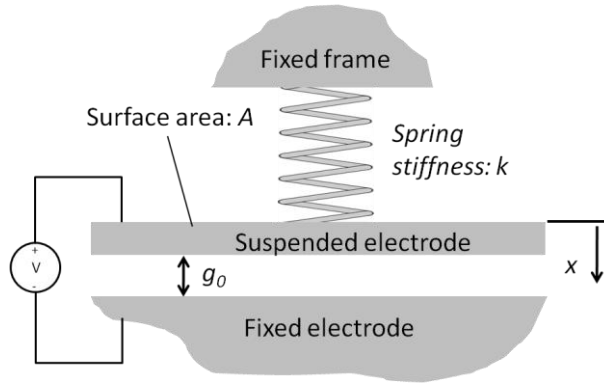


**Figure 2.2: Parallel plates electrostatic actuator.**

## 2.2 Analysis of the Microvalve

In the analysis of the microvalve, mainly the leakage ratio is considered to assess the performance. The leakage ratio of the microvalve is defined as:

$$L(V_a) = \frac{Q(V_a)}{Q(0)} \quad (2.8)$$

The parameters affecting the leakage ratio are the mechanical properties of the valve material, electrical properties of the working fluid and the valve material, physical properties of the working fluid, and the valve geometry. Among these, the valve geometry and the mechanical properties of the valve material control the stiffness of the diaphragm. This affects the pull-in voltage in turn, as described by equation (2.6). According to equation (2.6), reducing the stiffness decreases the pull-in voltage. However, if the stiffness is reduced too much, then the diaphragm becomes excessively susceptible to fluidic pressure, which means that electrostatic forces may not be enough to close the microvalve. Electrical properties of the valve material, namely parylene, and the working fluid affect the electrostatic forces, as implied by equation (2.6) again. As shown by the capacitive structure of the microvalve (Figure 2.2), the media between the actuating electrodes is composed of a thin layer of parylene and the working fluid. Therefore, permittivity of both layers affects the electrostatic forces on the diaphragm. Besides, in case the working fluid is an

electrolytic solution, there would be a charge flow across the electrodes, which alters the capacitive structure shown in Figure 2.2.

The last parameter set, which is the physical properties of the working fluid, affects directly the flow rate. Descriptions of these parameters are listed in Table 2.1. Additionally, geometrical parameters are shown in Figure 2.3.

As described in the previous section, the leakage ratio is described by the deflection profile of the diaphragm. Therefore, the forces on the diaphragm should be defined to explain the leakage behavior of the microvalve.

There are two external forces acting on the diaphragm; electrostatic force and the fluidic pressure. The electrostatic force is defined as a distributed load on the diaphragm. Based on the capacitive model shown in Figure 2.3, this load can be found as [90]:

$$q_e = -\frac{\varepsilon_0 \varepsilon_f V_a^2}{2 \left( (h - \omega) + \frac{\varepsilon_f t_p}{\varepsilon_p} \right)^2} \quad (2.9)$$

where  $\varepsilon_0$  is the permittivity of vacuum,  $\varepsilon_f$  is the dielectric constant of the working fluid,  $\varepsilon_p$  is the dielectric constant of parylene,  $t_p$  is the thickness of the parylene diaphragm,  $h$  is the channel height,  $\omega$  is the amount of deflection, and  $V_a$  is the actuation potential. Equation (2.9) is valid before pull-in. After pull-in, a portion of the diaphragm touches the bottom, changing the capacitive structure at touch area. In this case, the media between the electrodes would be composed of only parylene. Therefore,  $q_e$  should be revised as:

$$q_e = \begin{cases} -\frac{\varepsilon_0 \varepsilon_f V_a^2}{2 \left( (h - \omega) + \frac{\varepsilon_f t_p}{\varepsilon_p} \right)^2} & \omega \in [0, h) \\ -\frac{\varepsilon_0 \varepsilon_p V_a^2}{2 t_p^2} & \omega = h \end{cases} \quad (2.10)$$



**Table 2.1: Parameters involved in the analysis of normally open electrostatic microvalve.**

Geometrical parameters		Mechanical properties of the structural materials		Electrical properties of the structural material		Electrical and physical properties of the working fluid	
$R$	Radius of the valve	$E_p$	Elastic modulus of parylene (3.2 GPa)	$\epsilon_p$	Dielectric constant of parylene (3.15)	$\epsilon_f$	Dielectric constant of the working fluid (1 for air, 3 for oil, 80 for DI water)
$t_p$	Thickness of the parylene diaphragm	$\nu_p$	Poisson's ratio of parylene (0.33)			$\sigma_f$	Conductivity of the working fluid (0 for air and oil, 0.5 $\mu\text{S}/\text{cm}$ for DI water)
$t_e$	Thickness of the top electrode	$E_{Au}$	Elastic modulus of gold (77.2 GPa)			$\rho_f$	Density of the working fluid (1.225 $\text{kg}/\text{m}^3$ for air, 920 $\text{kg}/\text{m}^3$ for oil, 1000 $\text{kg}/\text{m}^3$ for DI water)
$h$	Channel height	$\nu_{Au}$	Poisson's ratio of gold (0.42)			$\eta_f$	Dynamic viscosity of the fluid (0.35 Pa.s for oil, 0.001 Pa.s for DI water)
$H$	Channel width						

Permittivity of vacuum  $\epsilon_0$  is  $8.854 \times 10^{-12}$  F/m.

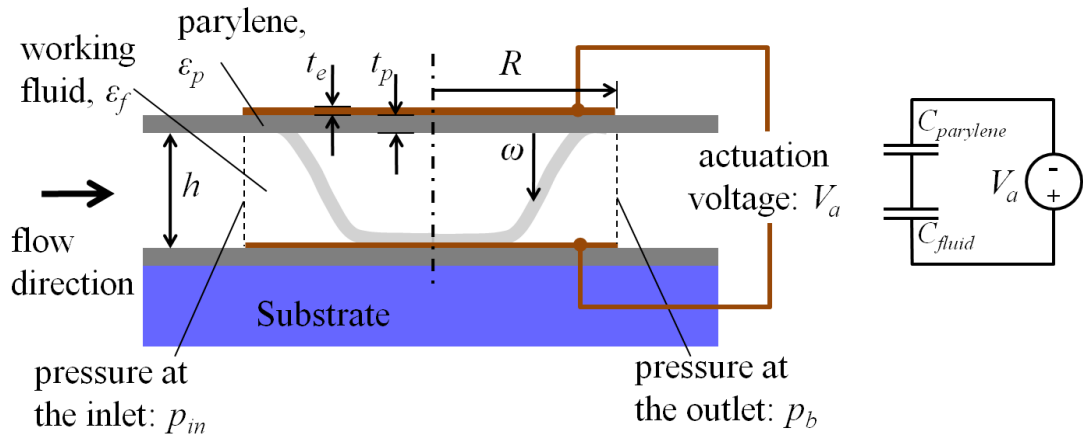


**Figure 2.3: Geometrical parameters involved in the analysis and the capacitive structure of normally open electrostatic microvalve.**

The fluidic pressure on the microvalve is described by the inlet pressure and the back pressure. Given these boundary conditions, fluidic pressure distribution on the diaphragm can be found by solving the Navier-Stokes equation:

$$\rho_f \frac{\partial \mathbf{u}}{\partial t} - \nabla \cdot \left[ -p_f \mathbf{I} + \nu_f \left( \nabla \mathbf{u} + (\nabla \mathbf{u})^T \right) \right] + \rho_f \mathbf{u} \cdot \nabla \mathbf{u} = 0 \quad (2.11)$$

where  $\mathbf{u}$  is the velocity field,  $\rho_f$  is the density of the working fluid,  $\nu_f$  is the viscosity of the working fluid, and  $p_f$  is the fluidic pressure. However, after pull-in, fluidic pressure would be simply zero on the touch area. Therefore, an additional constraint should be defined stating that the fluidic pressure is zero at the touch area:

$$p_f = \begin{cases} p_f & \omega \in [0, h) \\ 0 & \omega = h \end{cases} \quad (2.12)$$

Consequently, static equilibrium condition of the diaphragm can be stated as:

$$p_f + q_e - K\omega = 0 \quad (2.13)$$

where  $K\omega$  is the elastic restoring force described by the mechanical properties of diaphragm material and geometry. Equations (2.10) and (2.12) can be solved to obtain the flow rate across the microvalve, which is the surface integral of the velocity field over the inlet or the outlet of the valve.

Here, it is important to note that both electrostatic pressure and fluidic pressure are dependent on the amount of deflection. This means that external forces are not uniform (because of the fluidic pressure variation across the valve) and affect each other (prescribed by the deflection). Under these circumstances, it can be concluded that analytical solution of the problem may not be feasible. Therefore, finite element method is considered as the solution tool.

The problem involves two physical domains; mechanical domain prescribed by equation (2.12) and fluidic domain prescribed by equation (2.11). There are many commercial finite element analysis programs to deal with such multi-physics problems [91-93]. Among these, COMSOL Multiphysics is selected, since it enables

the user to define custom equations, which is especially useful in definition of aforementioned constraints and equations. Moreover, the software allows interfacing with other engineering design and analysis programs; MATLAB and SOLIDWORKS, which may improve the design capability. Another advantage in selection of COMSOL Multiphysics is that the software is widely used in MEMS and microfluidics community yielding a great deal of knowhow.

For the solution of such multiphysics problems, generally there are two approaches; solving the equations describing the physical domains simultaneously (direct coupling) or sequentially (sequential coupling). In the analysis of this problem, sequential coupling is preferred mainly to decrease the computational time.

In order to solve the problem, solid model of the microvalve is created considering the symmetry constraints. Figure 2.4 shows the solid model with boundary definitions. After creating the model and defining the boundary conditions, the model is meshed using default tetrahedral elements with quadratic shape function. Using the meshed model, equation (2.10) is solved for the pressure distribution and the velocity field, as the first step in solution. Using the pressure distribution and knowing the actuation potential, equation (2.12) is solved for the deflection profile of the diaphragm. As the next step, equation (2.10) is solved once more with this updated geometry. This iterative procedure is carried out until a prescribed error margin in flow rate is achieved. Flow rate is computed by integrating the velocity field over cross section area of the microchannel at the inlet or outlet. Consequently, flow rate versus the actuation potential can be obtained. Figure 2.5 shows the diaphragm deflection and corresponding streamlines obtained at 0 V actuation potential.

However, a stable solution cannot be obtained at pull-in voltage. In order to find a stable solution, an additional constraint is defined stating that center point deflection is equal to the channel height at pull-in (2.14) [94]. Iterative solution procedure is carried out with this constraint to obtain solution beyond pull-in (Figure 2.6).

$$\omega(0,0) = h \quad (2.14)$$

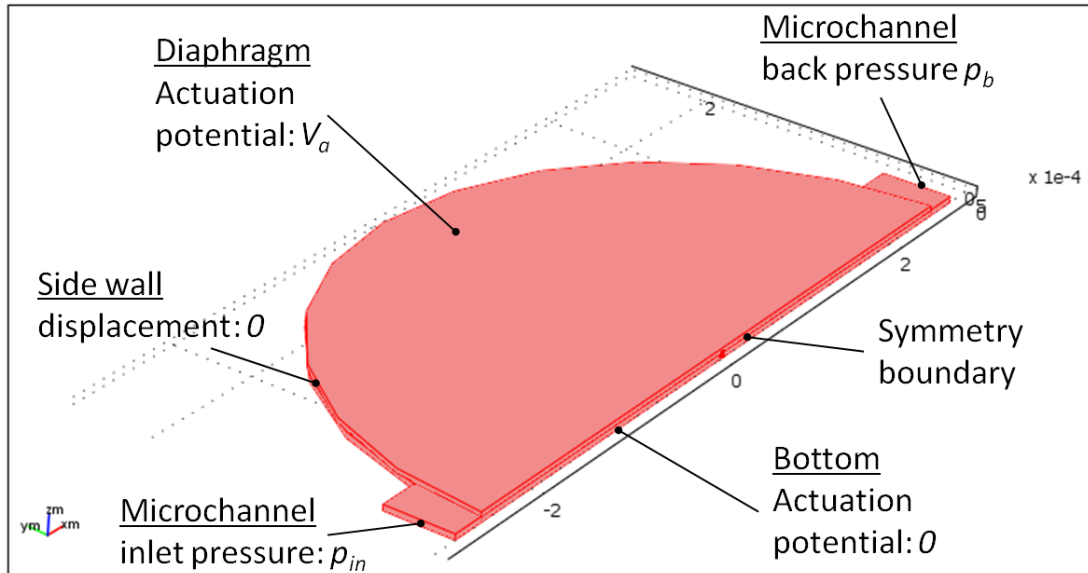


**Figure 2.4: Solid model of the microvalve showing the boundary conditions.**

Solution procedure explained above is illustrated by a flow chart in Figure 2.7. To verify the solutions obtained using this procedure, a convergence analysis is done. For this purpose, flow rate at specific inlet pressure and actuation potential is solved repeatedly by refining the mesh. Resulting flow rate and total CPU time are recorded. Figure 2.8 shows that the flow rate converges as the mesh is refined, which indicates the correctness of the solution. However, increase in CPU time is significantly larger compared to the convergence rate. Considering this trade-off, a relatively coarse mesh is used in the analysis.

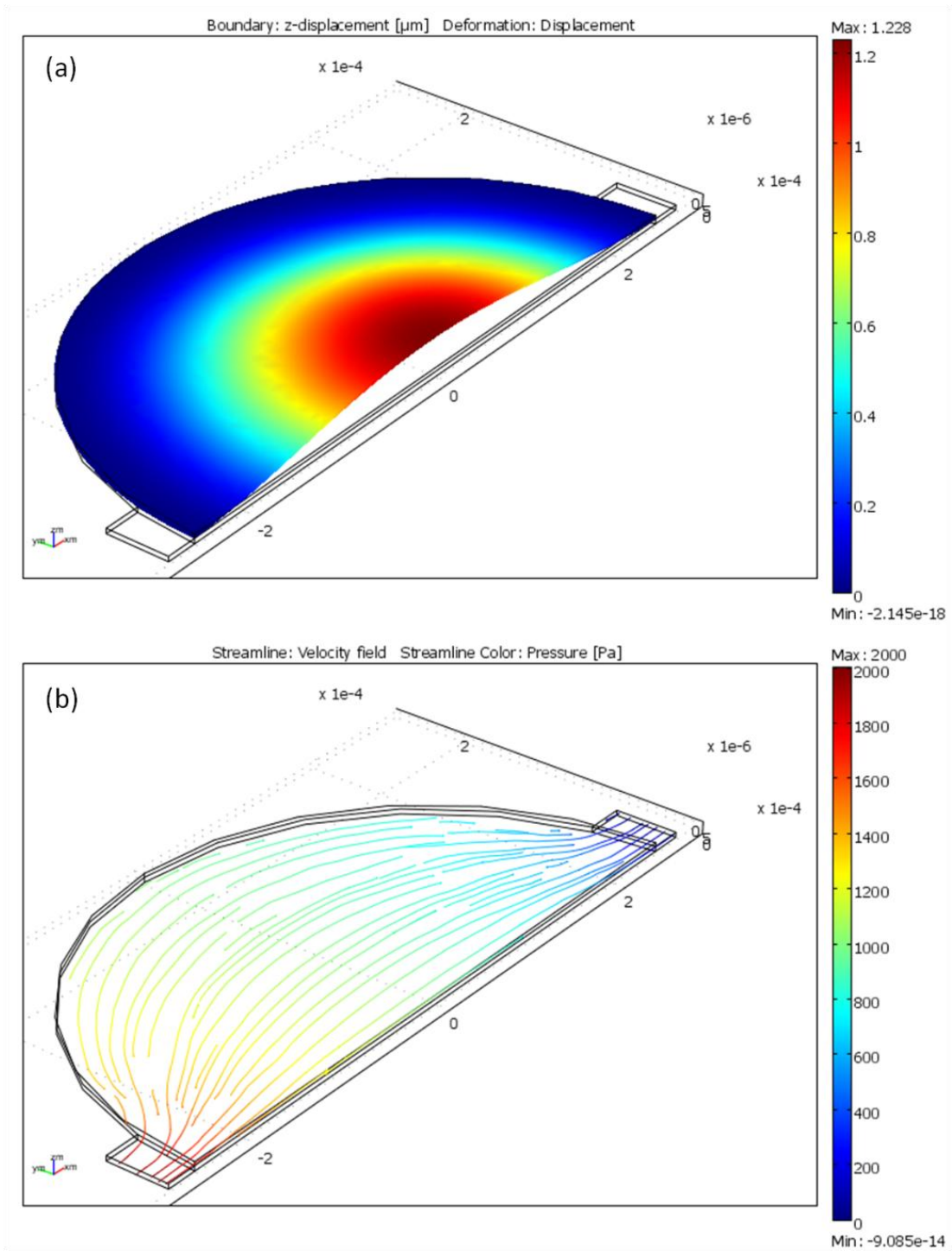


**Figure 2.5: Diaphragm deflection and velocity field solved at 0 V actuation potential. Diaphragm radius and inlet pressure are 250  $\mu\text{m}$  and 2 kPa respectively.**

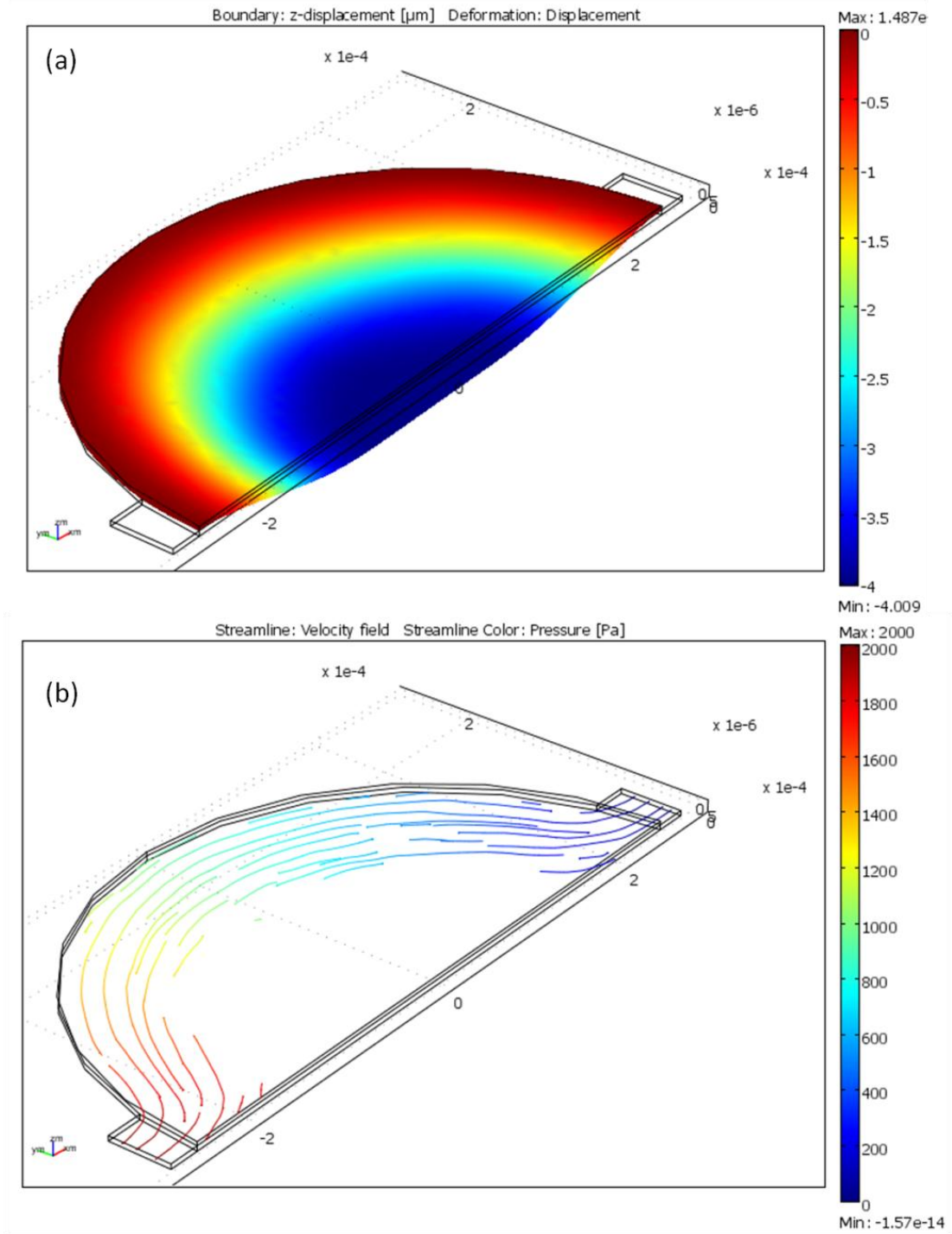


**Figure 2.6: Diaphragm deflection and velocity field solved at pull-in. Diaphragm radius and inlet pressure are  $250 \mu\text{m}$  and 2 kPa respectively.**

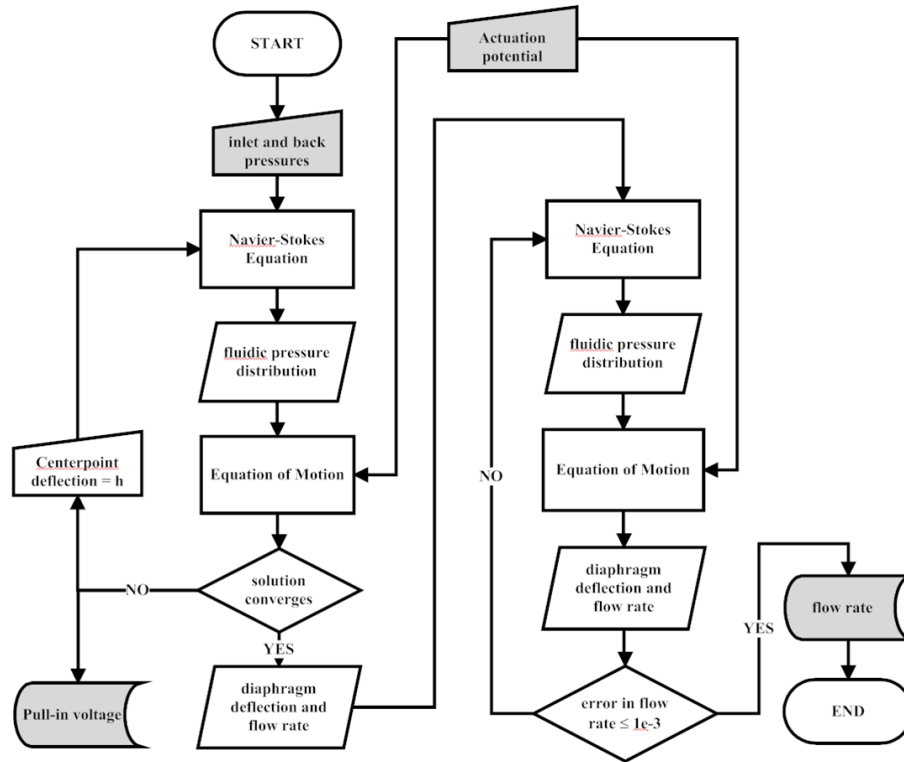


Figure 2.7: Flow chart illustrating the solution procedure.

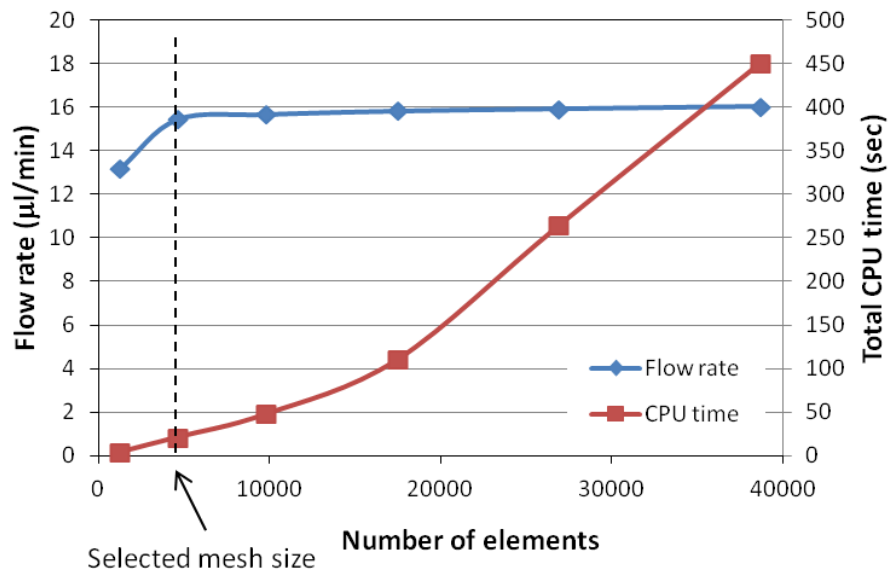


Figure 2.8: Total CPU time and convergence of the flow rate ( $V_a = 0$  V,  $p_{in} = 2$  kPa) versus the number of elements.

In order to examine the path dependence of the microvalve, solution procedure explained above is run for increasing and decreasing actuation potentials. At each potential level, solution found is defined as the initial condition for the next level. The results show that there is hysteresis in operation. As the actuation potential is increased, the flow rate decreases abruptly at pull-in potential, as prescribed by the analysis explained above. On the other hand, after pull-in electrostatic force becomes significantly larger, as implied by equation (2.9). As a result, pull-out of the diaphragm occurs at a potential level lower than the pull-in voltage [95]. Figure 2.9 shows the change in normalized flow rate with the actuation potential and the hysteresis effect in operation for air and oil as the working fluids at different inlet pressures. The hysteresis curve shows that as the pull-in voltage becomes larger, pull-out occurs at significantly lower potentials, which is also in accordance with the theory explained in [96].

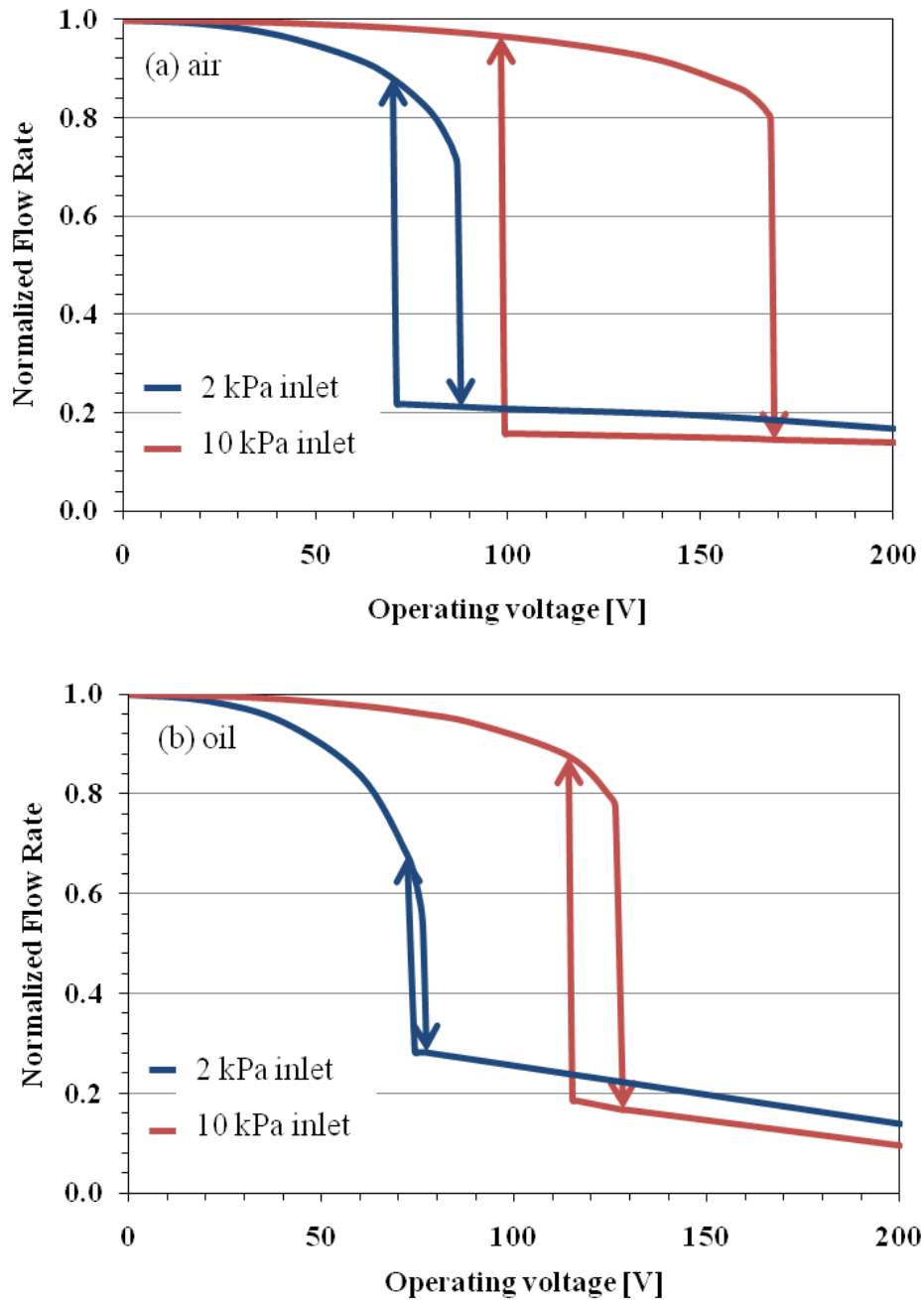
Figure 2.9 reveals that pull-in voltage increases with the inlet pressure, since larger electrostatic forces are required to close the microvalve. Pull-in voltage is computed for different inlet pressure levels for air and oil as working fluids (Figure 2.10). It is seen that the relation between the pull-in voltage and the inlet pressure is almost linear in low pressure range.

Figure 2.10 implies that as the inlet pressure increases it becomes impossible to close the microvalve at certain actuation potentials. Figure 2.11 shows the flow rate versus the inlet pressure for different actuation potentials. Dash lines denote bursting of the microvalve, where the electrostatic forces become insufficient to keep the microvalve closed.

Revisiting Figure 2.9 reveals that electrical properties of the working fluid affect the pull-in voltage. To investigate the relation between the pull-in voltage and the electrical properties of the working fluid, pull-in voltage is computed for different dielectric constants (Figure 2.12). The results show that pull-in becomes minimum for certain working fluids (fluids with dielectric constant between 3-5). After this minimum, pull-in voltage constantly increases. The results also show that it may be practically impossible to close the microvalves in case of working fluids with



relatively high dielectric constants (e.g. deionized water with dielectric constant of 80).



**Figure 2.9: Normalized flow rate versus the actuation potential for (a) air and (b) oil at different inlet pressures. Back pressure is assumed to be zero.**

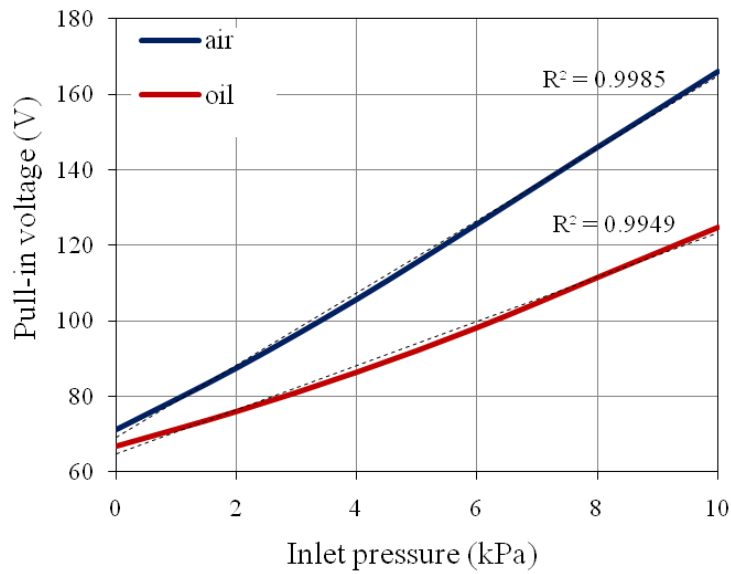


**Figure 2.10: Pull-in voltage versus the inlet pressure for air and oil as the working fluids. Dotted lines indicate the linearity between pull-in voltage and inlet pressure.**

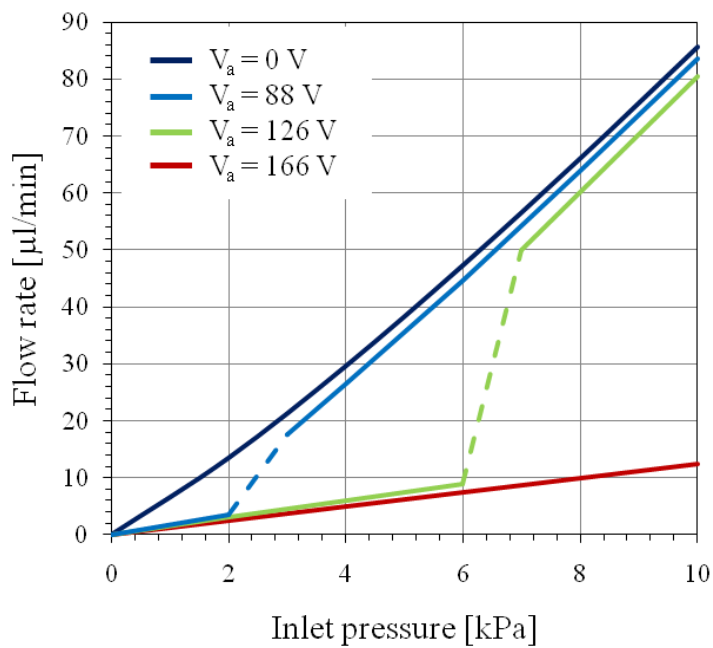


**Figure 2.11: Flow rate versus the inlet pressure for different actuation potentials. Back pressure is assumed to be zero. Working fluid is air.**

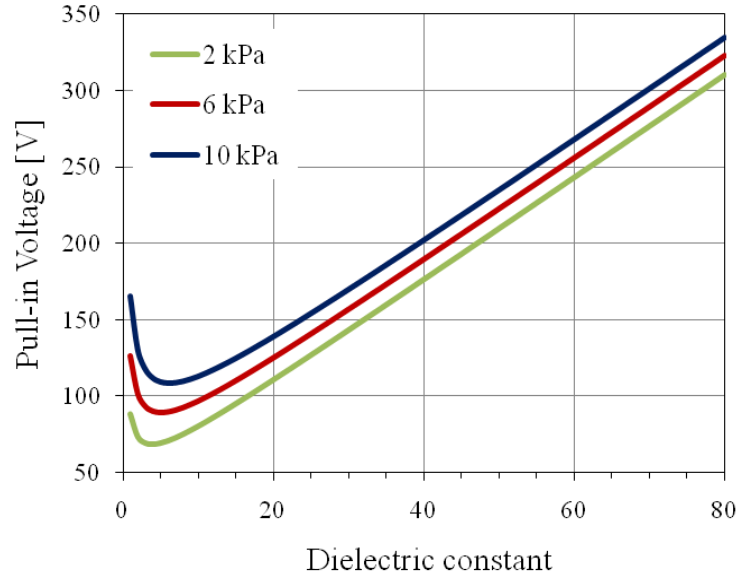


**Figure 2.12: Pull-in voltage versus dielectric constant for different inlet pressures. Back pressure is assumed to be zero.**

On the other hand, dielectric constant is not the only parameter that affects the pull-in of the diaphragm. The conductivity of the working fluid also affects the pull-in behavior. In case of ionic solutions, ions tend to accumulate at the solid-liquid interface forming an electric double layer (EDL). Figure 2.13 shows EDL formation in the microvalve. This EDL introduces a significantly large capacitance defined by  $C_{EDL} = \varepsilon A / \lambda_d$ , where  $C_{EDL}$  is the capacitance of the EDL,  $\varepsilon$  is the permittivity of the electrolytic solution,  $A$  is the electrode area, and  $\lambda_d$  is the Debye length [97]. Depending on the electrolyte concentration, Debye length can be in the order of few nanometers. Because of this capacitive effect of the EDL, the actuation potential diminishes steeply across the Debye length, screening the operation of the electrostatic actuator [88]. Figure 2.13 also shows the voltage change across the electrodes.

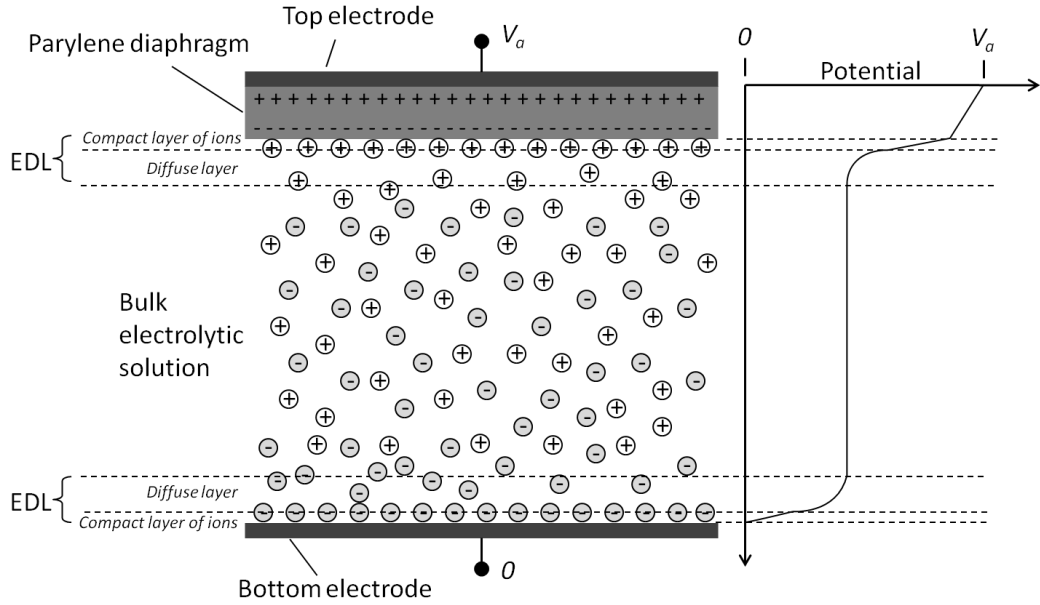


**Figure 2.13: EDL formation in the microvalve and corresponding voltage change across the channel.**

For the microvalve to operate in an electrolytic solution, the polarity of the actuation potential should be altered at a certain frequency [88]. This critical frequency should be such that the polarity is changed before the ions accumulate at solid-liquid interface. To determine this critical frequency, the capacitive structure of the microvalve should be revised as shown in Figure 2.14. The critical frequency can be simply defined in terms of the time constant of the equivalent circuit model shown in the figure, which is the time required to charge the EDL [88] (2.15).

$$f_c = \frac{1}{2\tau} \quad (2.15)$$

In (2.15)  $\tau$  is the time constant of the equivalent circuit shown in Figure 2.14. For this circuit,  $\tau$  can be found as [88]:

$$\tau = \frac{\epsilon_f \epsilon_0 h}{\sigma_f t_p} \quad (2.16)$$

Therefore, critical frequency can be defined as:

$$f_c = \frac{\sigma_f t_p}{2\epsilon_f \epsilon_0 h} \quad (2.17)$$

As a result, it can be stated that in case of an electrolytic solution, pull-in voltage computed by the aforementioned analysis should be applied at a critical frequency prescribed by equation (2.17) in order to close the microvalve.

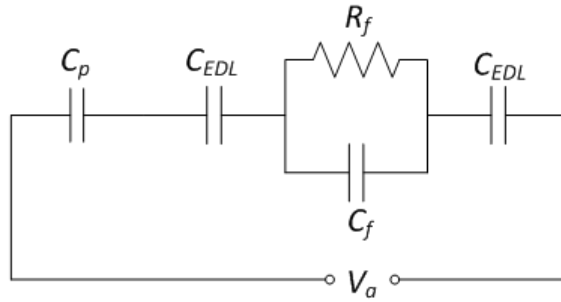


**Figure 2.14: Equivalent circuit model of the microvalve with EDL.  $C_p$  is the capacitance of the parylene diaphragm,  $C_{EDL}$  is the capacitance of the electric double layer,  $R_f$  is the electrical resistance of the liquid,  $C_f$  is the capacitance of the bulk liquid.**

Dimensions of the microvalve are determined based on the analysis results and the fabrication concerns. To determine the valve radius, forces on the diaphragm are considered. Equation (2.6) shows that, as the valve radius is increased, pull-in voltage decreases. However, if the valve radius is increased excessively, the diaphragm becomes more susceptible to the fluidic pressure. Hence, it may be impossible to pull-in the diaphragm by applying moderate potentials. In addition, increasing the valve radius too much may create stiction problems during fabrication [98]. To cover a wide range, microvalve radii are selected as 150  $\mu\text{m}$ , 250  $\mu\text{m}$ , 350  $\mu\text{m}$ , and 450  $\mu\text{m}$ . Another dimension to be determined is the diaphragm thickness. Equation (2.9) implies that, decreasing the diaphragm thickness increases the electrostatic force. Existing technology allows parylene coating of as low as 0.5  $\mu\text{m}$ .

However, based on the fabrication experience, it is determined that minimum of 3  $\mu\text{m}$  parylene layer can be successfully processed (Details of the process are explained in the following section). The last design parameter is the microchannel height. Equation (2.9) also implies that, electrostatic force on the diaphragm is increased as the channel height is decreased. Existing fabrication capabilities allow reproducible fabrication of 4  $\mu\text{m}$  channels.

Design dimensions stated above are determined assuming that the diaphragm remains elastic during operation. However, this assumption should be verified before fabricating the prototypes. In order to prove the elasticity of the diaphragm, stresses are computed. Examining the operation of the microvalve, it can be stated that the stress on the diaphragm increases with the actuation potential. Therefore, stresses on the diaphragm are computed at 200 V actuation potential, which is relatively high compared to applied potential levels. Under this operating condition, maximum equivalent von Mises stress on the diaphragm is found to be 44 MPa. This stress is lower than the yield strength of parylene reported by the vendor, which is 55 MPa [99]. This confirms the elasticity of parylene during operation. This maximum stress is also compared with the yield point of gold. According to Weihs et al. [100] this stress is below the yield stress of gold. This result ensures the elastic behavior of the membrane under quasi-static loading conditions. Figure 2.15 shows the stress distribution on 250  $\mu\text{m}$  radius diaphragm actuated by 200 V potential.

Figure 2.16 shows the design dimensions. The prototypes with these design dimensions are fabricated for characterization. Details of the fabrication methods are explained in the next section.

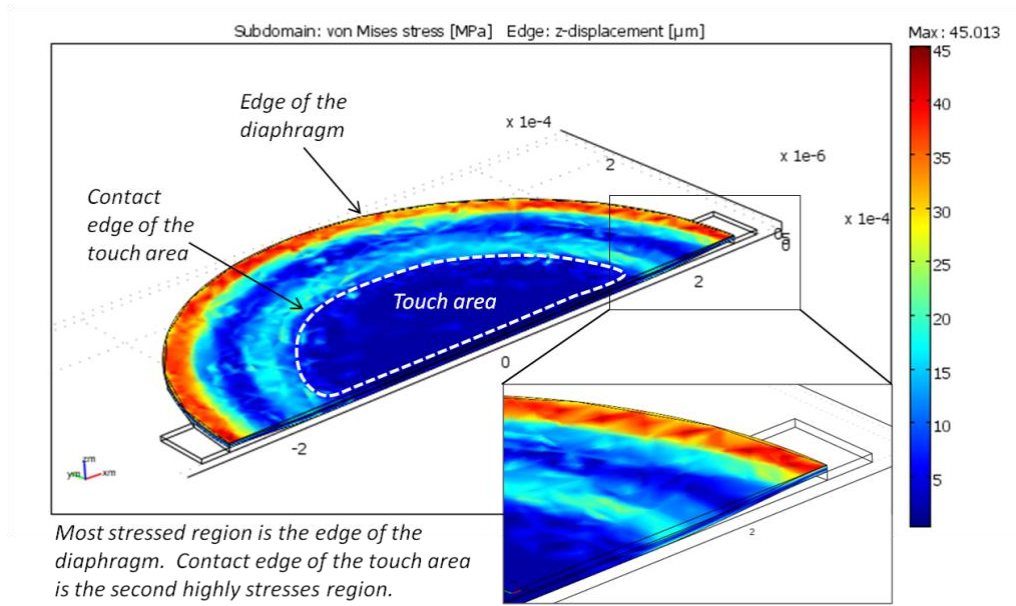


**Figure 2.15: Stress distribution on 250  $\mu\text{m}$  radius microvalve actuated by 200 V potential.**

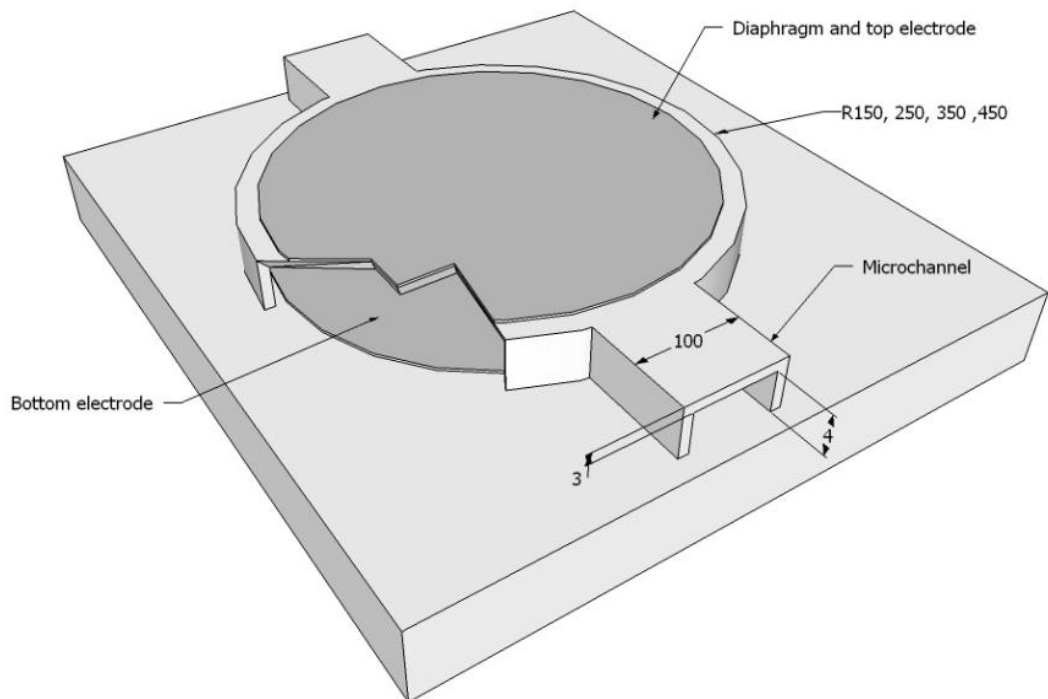


**Figure 2.16: Design dimensions of the normally open electrostatic microvalve.**

## 2.3 Fabrication of the Microvalves

To fabricate the prototypes, surface micromachining techniques are used. Surface micromachining is essentially based on successively forming and patterning of layers on a substrate. During fabrication, standard 4" diameter glass wafers are used as substrates.

Micromachining techniques allow fabrication of multiple prototypes on the same wafer, by following the same fabrication sequence. Therefore, microvalves with dimensional variations are fabricated on the same wafer. Layout drawings of these microvalves are created and compiled using Tanner<sup>®</sup> L-Edit<sup>®</sup> software. These layout drawings, which define the layers, are used to manufacture glass masks for patterning these layers during fabrication.

Figure 2.17 illustrates the layout of the testing prototype of 250  $\mu\text{m}$  valve radius. Each color on the layout drawing represents a different layer. On the layout, bottom and top electrodes of the microvalve are connected to contact pads through wire lines for external electrical connections. Additionally, inlet and outlet of the microvalves are connected to inlet and outlet reservoirs, where external fluidic connections are made, via microchannels. The reservoirs are designed to facilitate external fluidic connections. The rings at the periphery of the reservoirs act as a rib for mounting external fluidic ports. The configuration shown in Figure 2.17 is also used for 350  $\mu\text{m}$  and 450  $\mu\text{m}$  radius microvalves.

The prototypes mentioned above and their dimensional variations are laid out on a 4" diameter wafer. Schematic drawing of the whole wafer is given in Figure A. 1 in APPENDIX A. There are total of 45 devices on the layout. Multiples of each device is located on the same wafer in order to produce a batch of test devices on a single wafer. The devices are separated by vertical and horizontal lines. These lines facilitate dicing of the wafer into individual devices at the end of the fabrication.

### 2.3.1 Fabrication Process Flow

Fabrication of the microvalves is a 4-mask process. The patterns and definition of these masks are presented in Table A.1 in APPENDIX A. During fabrication, 4"



diameter glass wafers are used as substrates. Before the fabrication, the glass wafers should be treated with piranha solution (1:1  $\text{H}_2\text{SO}_4:\text{H}_2\text{O}_2$  mixture) and buffered HF solution (BHF) respectively. Piranha solution is used to remove organic residues on the wafer, while BHF roughens the wafer surface. This facilitates the adhesion of the following parylene layer on the wafer. Process flow after preparation of the wafers is illustrated in Figure 2.18.

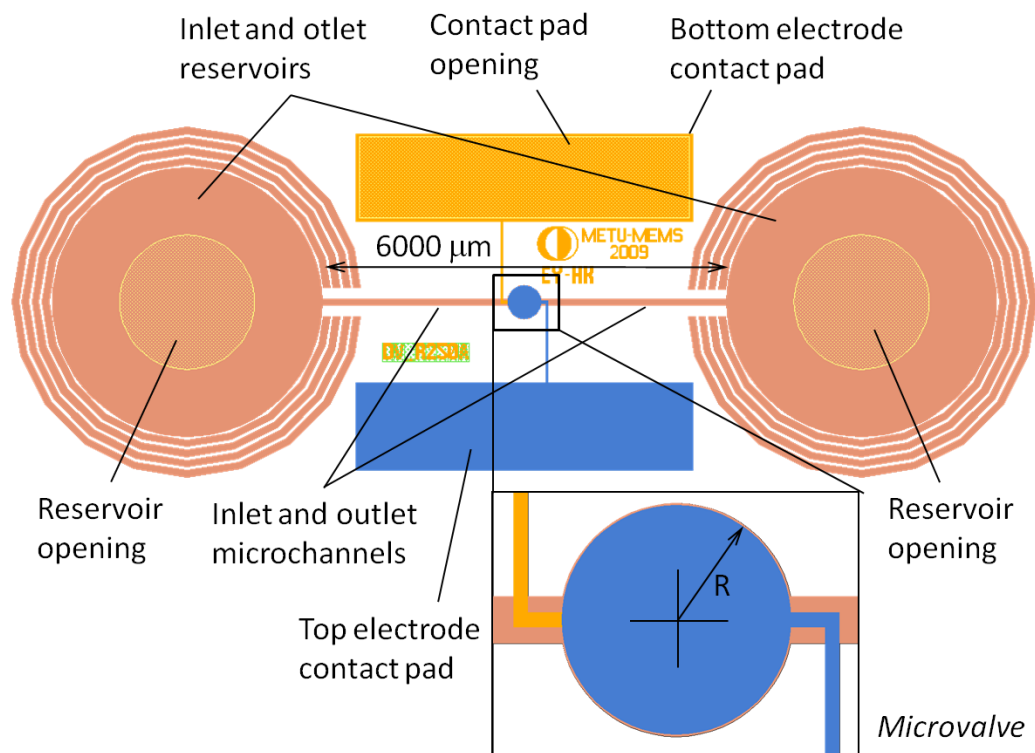


**Figure 2.17: Layout of the microvalve characterization prototype.**

As the first step in fabrication, the wafer is coated with 3 μm thick parylene layer. Parylene is the name of a group of polymers, with the basis poly-para-xylylene. As stated before, because of its transparent and biocompatible nature, parylene is a preferable material in life sciences. In addition, due to its elastic behavior (elastic modulus of parylene is 3.2 GPa), it is also preferred in fabrication of compliant structures. There are three common commercially available types of parylene;

parlyene-N, which is the basic type, parlyene-C, and parlyene-D (Figure 2.19). Among these, parlyene-C is the most preferable one, since it has the lowest permeability to moisture and corrosive gases and the lowest refractive index [101].

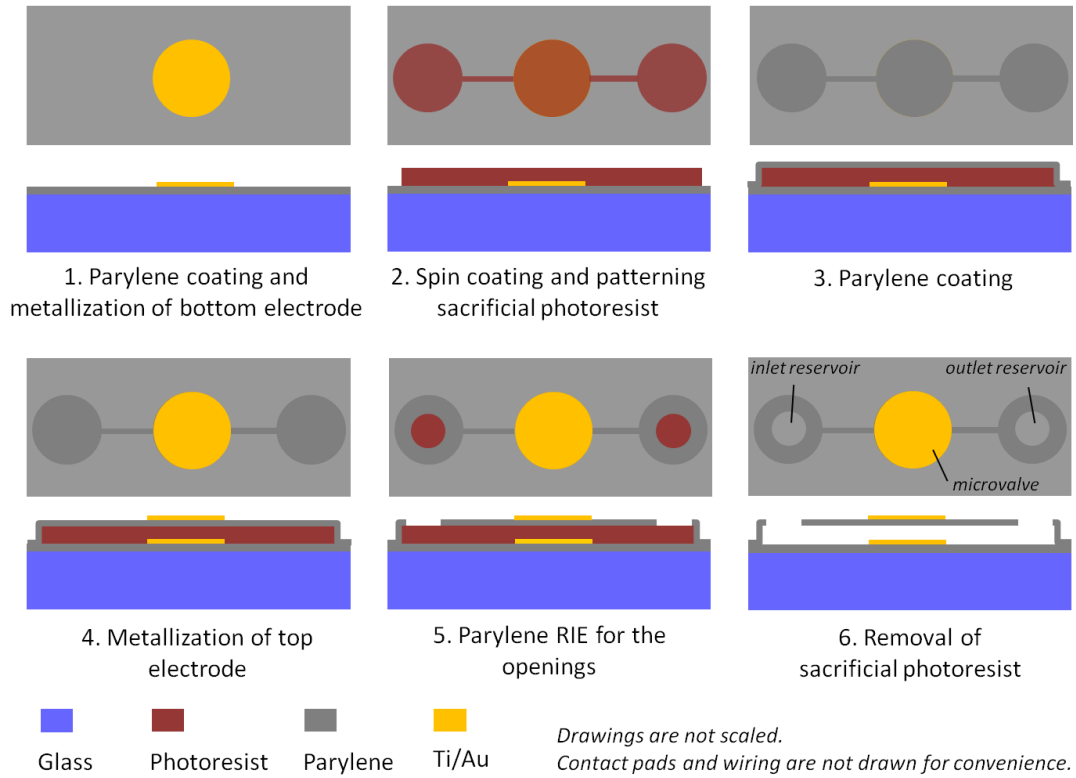


**Figure 2.18: Illustration of the fabrication processes. Top view and the cross-section of a single prototype are shown.**

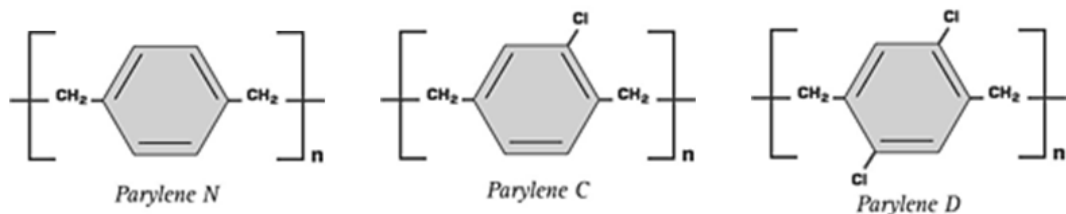


**Figure 2.19: Chemical structure of common types of parylene [101].**

Coating of parylene is basically a chemical vapor deposition (CVD) process. Regarding to the calibration of the parylene coating equipment, 2 gr of parylene-C in the form of dimer is used for 1  $\mu\text{m}$  of coating. Therefore, for 3  $\mu\text{m}$  thick coating, 6 gr of dimer is loaded into coating equipment. During the process, this dimer is evaporated at 175°C. Evaporated dimer is broken into monomers at 690°C. The monomer vapor polymerizes conformably on the wafer at room temperature. Since coating occurs at room temperature, parylene layer on the wafer is free of thermal stresses.

Next step in fabrication is the metallization of the bottom electrode. In this step, 150 nm thick Ti/Au bimetallic layer is sputtered on the wafer. After sputtering, Ti/Au layer is covered by a thin photoresist layer by spinning. This photoresist layer is exposed using the bottom electrode mask (Figure A.2) and developed, leaving a photoresist layer at bottom electrode and contact pad sites. This photoresist layer is then used as an etch mask to pattern underlying Ti/Au layer. Chemical etching is used to pattern Ti/Au layer. Afterwards, photoresist mask is stripped off the surface.

The third step is the formation of the microchannels, reservoirs, and valve chambers. This fabrication step is based on the technique introduced by Man et al. [101]. In this step, the wafer is coated with 4  $\mu\text{m}$  thick photoresist layer by spinning. The thickness of this layer defines the channel height. This photoresist layer is exposed using the channel mask (Figure A.3) and developed. Remaining photoresist pattern on the wafer includes the reservoirs, microchannels, and the valve chambers. After patterning, the photoresist layer is coated with 3  $\mu\text{m}$  thick parylene. However, before parylene coating, underlying photoresist layer should be kept in vacuum and hard baked in furnace for extended periods. This step is vital in fabrication of the microvalves. If this step is omitted, or not properly done, solvents in the photoresist evaporate during fabrication. This causes swelling of the covering parylene layer in the following top electrode metallization step. Figure 2.20 compares two cases with properly baked photoresist and insufficiently baked photoresist. Details of the baking procedure are given in process recipes in APPENDIX A. To assure that the dimensions of fabricated microchannels match with the design dimensions, surface

profile data of the microvalves are gathered using optical profiler. Since measurement relies on interferometry principles, this measurement should be carried out after coating transparent parylene layer with bimetallic Ti/Au layer. Figure 2.21 shows 3D map of the microvalve, which proves the agreement of the actual dimensions with design dimensions.

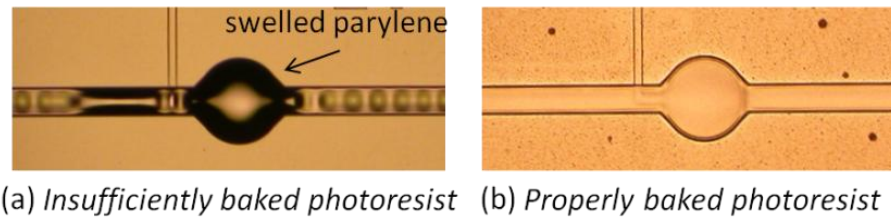


**Figure 2.20: Parylene swelling problem. Micrographs show two cases: (a) insufficiently baked photoresist (b) properly baked photoresist.**

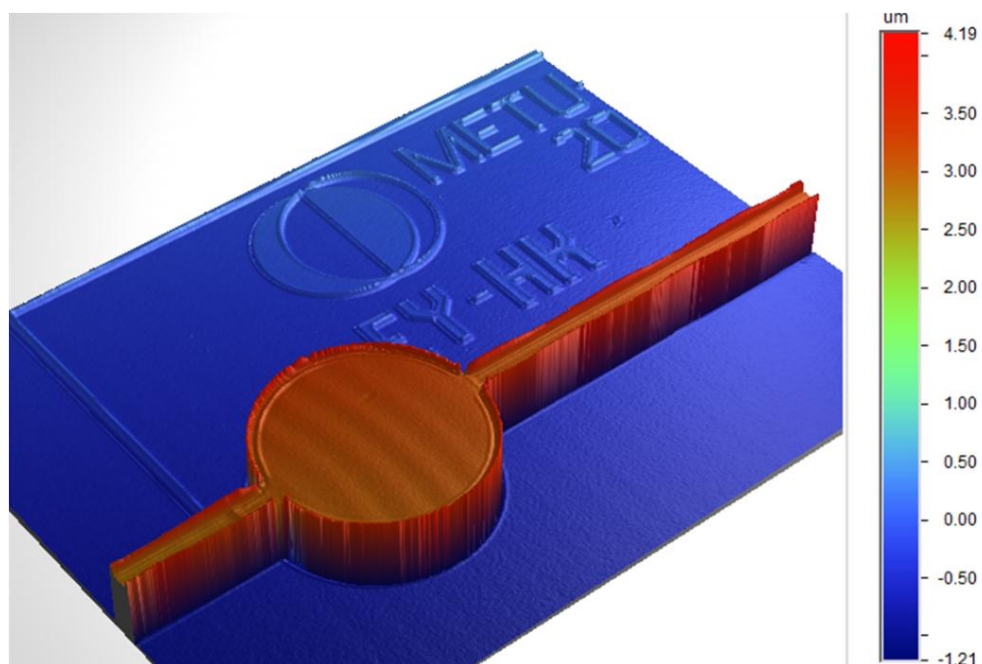


**Figure 2.21: 3D map of the normally open electrostatic microvalve obtained using Veeco Wyko NT1000 optical profiler.**

In the next step, wafer is coated with 150 nm thick Ti/Au bimetallic layer. After sputtering this bimetallic layer, the wafer is spin coated with a relatively thick photoresist layer, which conforms the surface topology. This photoresist layer is exposed using the top electrode mask (Figure A.4) and developed respectively. Afterwards, underlying Ti/Au layer is chemically etched using the photoresist as the masking layer. Then, the photoresist layer is stripped off, remaining top electrode and the contact pads open.

Next step in fabrication is to create the reservoir and contact pad openings. For this purpose, the wafer is coated with a thick (9  $\mu\text{m}$ ) photoresist layer by spinning. Then, this layer is exposed using the dark field opening mask (Figure A.5) and developed. Using this thick photoresist, underlying parylene layer is etched with reactive ion etching (RIE) process.

At the final step, the wafer is diced along the dicing streets (Figure 2.22) to obtain individual devices. These devices are then immersed in still acetone to remove photoresist at the top and inside the channels. Photoresist removal process is a concentration dependent diffusion process [102] and it takes approximately 2 days to remove the sacrificial photoresist inside the channels. At the end of this period, acetone inside the channels is removed by immersing the prototypes in isopropyl alcohol and methanol respectively. Methanol inside the channels is removed by evaporation on 70°C hotplate. Rapid evaporation of methanol prevents stiction of parylene channels.

Figure 2.22 shows the process wafer before parylene RIE step. Micrograph of the fabricated microvalve after photoresist removal is also shown in Figure 2.22.

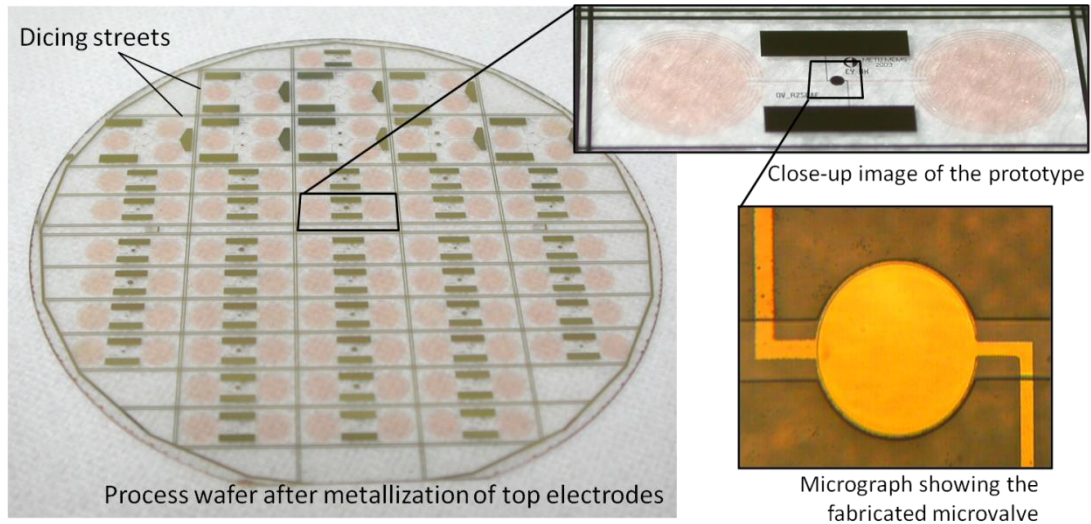


**Figure 2.22: Process wafer before parylene RIE step. Close-up view of a single prototype and micrograph of the microvalve are shown.**

#### 2.4 Characterization of the Microvalves

Fabricated prototypes are tested to determine pull-in voltage and leakage behavior. Pull-in tests are carried out under no flow condition with air, deionized (DI) water, and oil as the working fluid. For the tests with DI water and oil, at first microchannels are filled with the working fluid by capillary action. After then, actuation potential is gradually increased up to pull-in. Figure 2.23 illustrates the pull-in test setup. During the tests, slightly lower pull-in voltages are observed in case of oil, compared to air, which is predicted by the theory (Table 2.2). Moreover, the results obtained for oil are the minimum possible pull-in voltages for the microvalves with given dimensions. Because according to analysis results (Figure 2.12), pull-in voltage becomes minimum for fluids with dielectric constant around 3, which is the dielectric constant of oil. For the DI water, it could not be possible to pull-in the diaphragm by applying ac potential up to 100 V. This result is also predicted by the theory. According to Figure 2.12 and (2.16), approximately 300 V potential should be applied by switching its polarity at 0.7 MHz (600 Vpp square wave at 0.7 MHz) which is practically impossible.

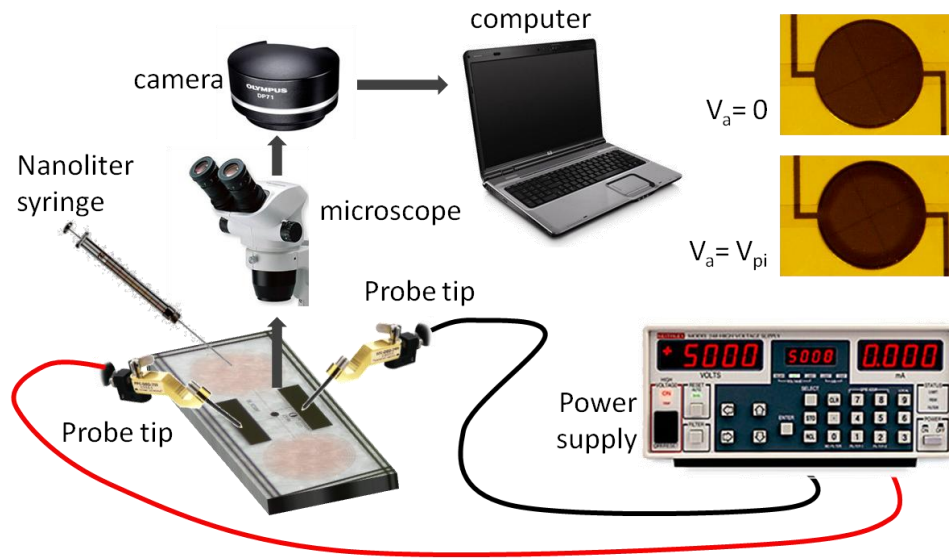


**Figure 2.23: Illustration of pull-in test setup.**

**Table 2.2: Pull-in test results compared with the theory.**

Diaphragm radius [ $\mu\text{m}$ ]	Pull-in voltage [V]			
	experimental		theoretical	
	(air)	(oil)	(air)	(oil)
450	19	14	22	21
350	33	26	36	34
250	65	47	71	67

To determine the effect of pressure on the pull-in voltage, tests are repeated under pressurized air flow. For this purpose, commercially available microfluidic ports are mounted on the inlet reservoir of the microvalves. Manufacturer of the microfluidic ports (LabSmith<sup>®</sup>) recommends 3M<sup>®</sup> DP-420 epoxy adhesive for mounting the ports on the reservoir. However, trials reveal that due to its low viscosity, recommended adhesive leaks into the microchannels by capillary forces and clogs the channels. It is found that, Loctite<sup>®</sup> 1C Hysol<sup>®</sup> epoxy adhesive has much higher viscosity and does not leak into the channels. Hence, Loctite<sup>®</sup> 1C Hysol<sup>®</sup> epoxy is used to mount the ports on the reservoirs. However, this epoxy cannot provide a good sealing. It is

observed that pressurized fluid leaks out at the port site in case Loctite® 1C Hysol® epoxy is used. Therefore, as the best practice, ports are mounted on the reservoirs using Loctite® 1C Hysol® epoxy, and then sealing is provided by applying 3M® DP-420 epoxy at the periphery of the port after mounting. Curing of these epoxy adhesives can be accelerated at elevated temperatures. However, adhesives are cured at room temperature to prevent thermal stresses. Figure 2.24 shows the prototype with microfluidic port mounted, and ready for pressurized testing.

Pressurized pull-in tests are carried out with air as the working fluid. For the tests, an air pump is used to provide pressurized air. Pressurized air is directed to the microfluidic port through 3 mm inner diameter tubing. A pressure regulator and a pressure gage are located just before the port to control the inlet pressure. The results show that pull-in voltage increases with increasing inlet pressure, which is in accordance with the theory. The results also show that this change is almost linear in low pressure range. Figure 2.25 shows the change in pull-in voltage with the inlet pressure for 250  $\mu\text{m}$  radius microvalves.

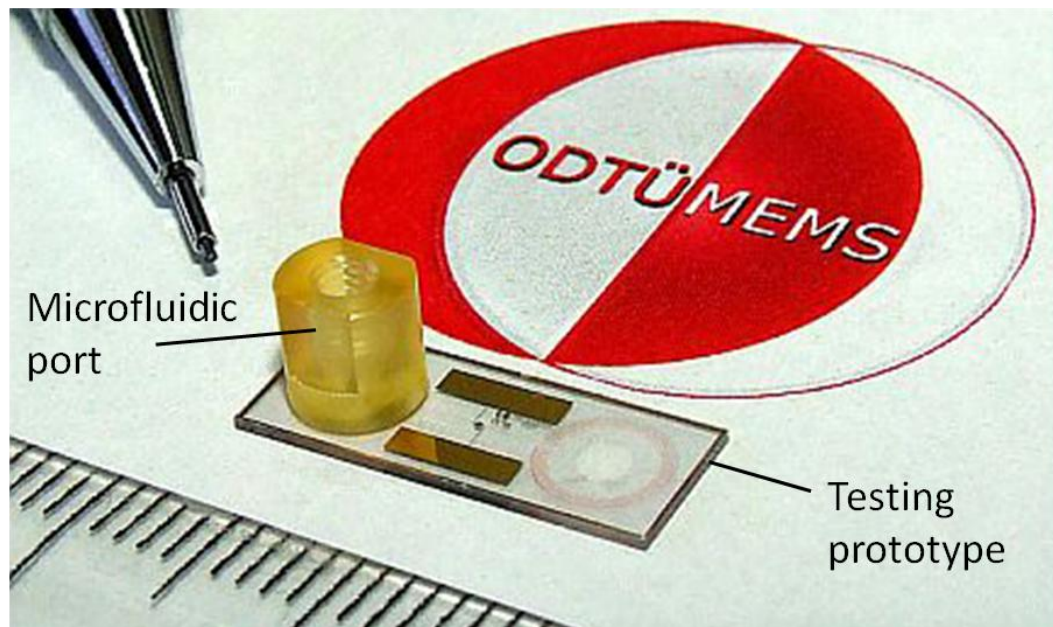


**Figure 2.24: Prototype with microfluidic port mounted.**



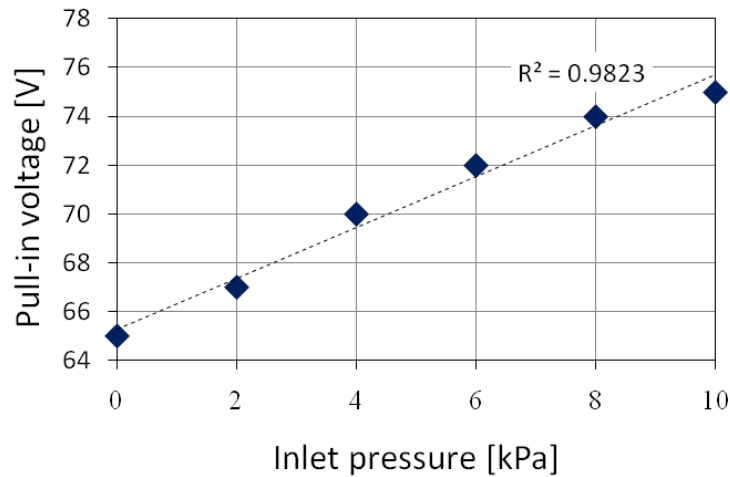


**Figure 2.25: Pull-in voltage versus the inlet pressure for 250  $\mu\text{m}$  radius microvalves.**

**Working fluid is air. Dash line denotes the curve fitted to data.**

After pull-in characterization, microvalves are tested for flow characterization. Air is used as the working fluid in flow characterization tests. The setup used for testing is essentially the same with the one used in pressurized pull-in tests. On the other hand, the setup is modified to measure the flow rate. In order to measure the flow rate, a glass capillary with a droplet inside is placed just before the pressure gauge. During the tests, droplet position in the capillary is recorded by a camera. Since the capillary is in-line with the microchannel, the flow rate of the droplet in the capillary gives the flow rate in the microchannel. In order to ensure the droplet is in the field-of-vision of the camera, a syringe pump is located before the capillary. This syringe pump is used to place the droplet under the camera, just before testing. Figure 2.26 shows the schematic drawing of this custom test setup. Implemented setup is also shown in Figure 2.26.

As stated before, in order to measure the flow rate droplet position in a capillary tube is recorded by a camera. Afterwards, recorded video is processed by using a macro written on Java based open source image processing tool; ImageJ. Consequently, relative position of the droplet front in time could be determined. Time derivative of this droplet position is multiplied with the cross-section area of the capillary tube,

which gives the flow rate in time. Mean of the data is defined as the flow rate at specified inlet pressure and actuation potential. Standard deviation is defined as the error in measurement. Figure 2.27 illustrates the flow rate measurement method.

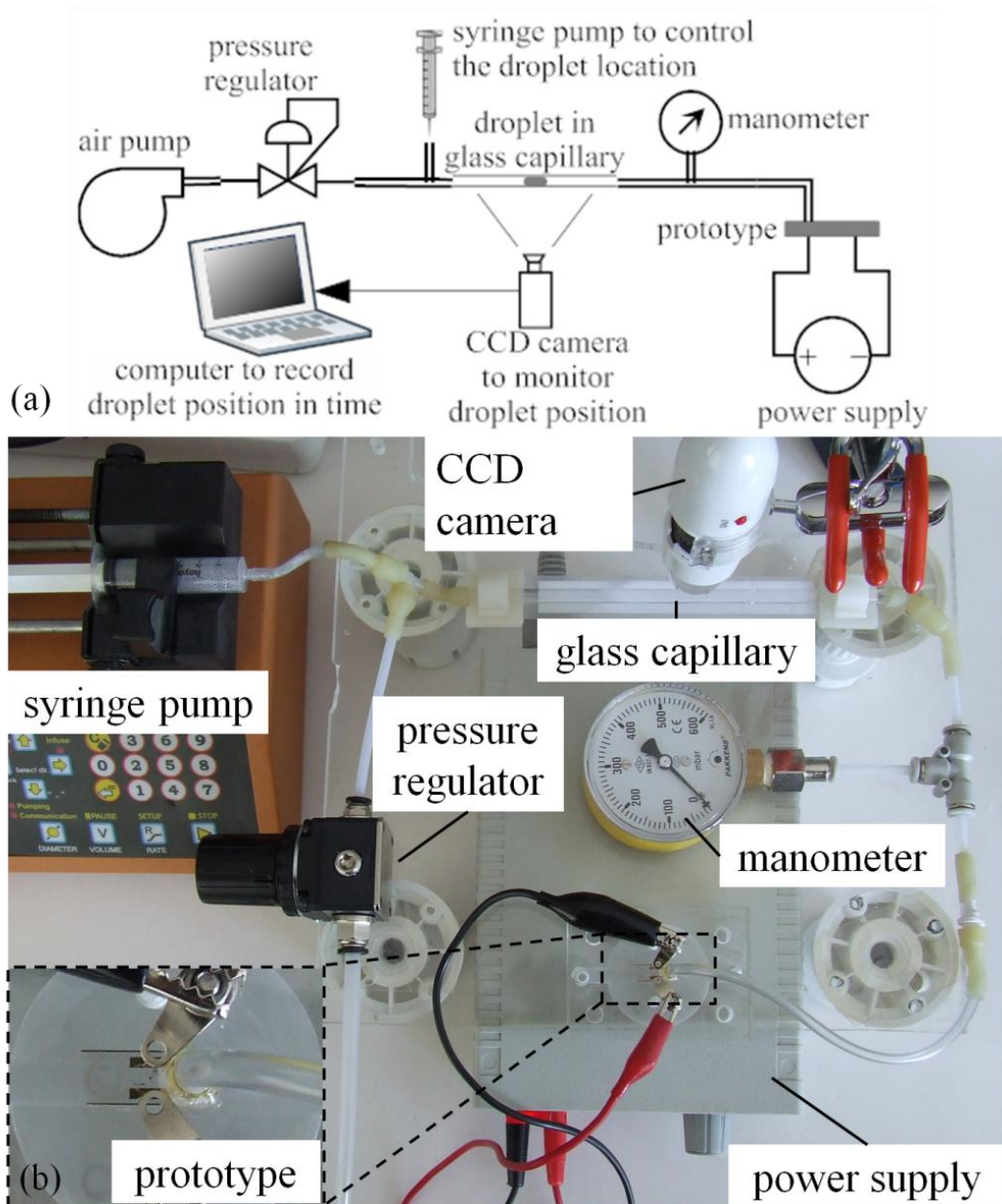


**Figure 2.26: (a) Schematic drawing of the flow test setup. (b) Implemented flow test setup.**

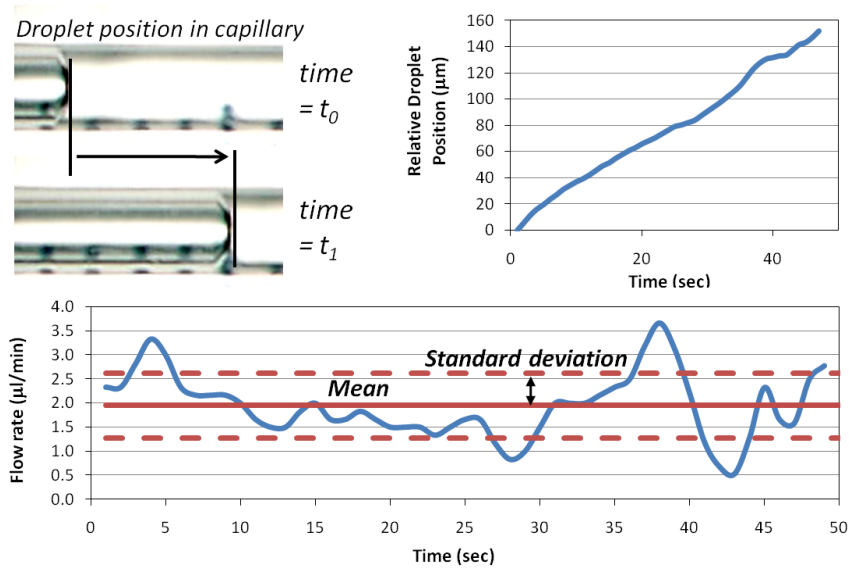


**Figure 2.27: Illustration of the flow rate measurement method. Data are plotted for inlet pressure and actuation potential of 6 kPa and 0 V respectively.**

Flow rate across the microvalve is measured at different inlet pressures and actuation potentials for 250  $\mu\text{m}$  radius microvalve. Figure 2.28 shows the flow rate measured in open ( $V_a = 0\text{ V}$ ) and closed ( $V_a = 85\text{ V}$ ) states of the microvalve, compared with the theoretical results. To compare the test results with the theory, pressure drop along the inlet and outlet channels (Figure 2.17) are considered in the analysis. The solutions presented in section 2.3 are modified accordingly. The results show that there is no considerable leakage up to 4 kPa inlet pressure. On the other hand, leakage ratio prescribed by equation (2.8) increases to 17 % at 10 kPa.

To examine the effect of actuation potential on leakage, flow tests are also carried out at different voltages. Figure 2.29 shows the flow rate measured at different potentials for 250  $\mu\text{m}$  radius microvalve under constant inlet pressure. The results show that the flow rate decreases almost linearly with increasing actuation potential beyond pull-in. The slope of the fitted line is used to estimate the sensitivity of flow rate to actuation potential after pull-in. Normalizing the slope with the open flow rate gives the sensitivity of leakage, which is found as  $10^{-3}\text{ V}^{-1}$ .

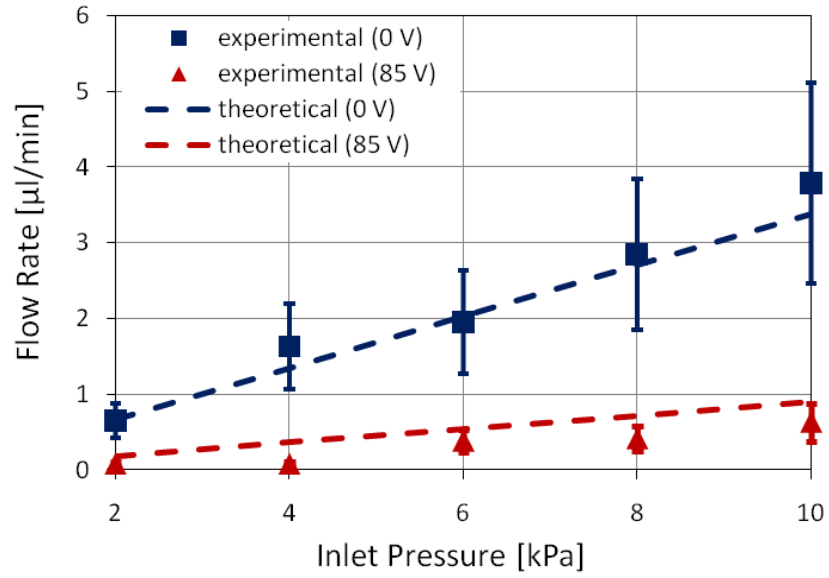


**Figure 2.28: Flow rate at different inlet pressures in open ( $V_a = 0$  V) and closed ( $V_a = 85$  V) states of the microvalve.**

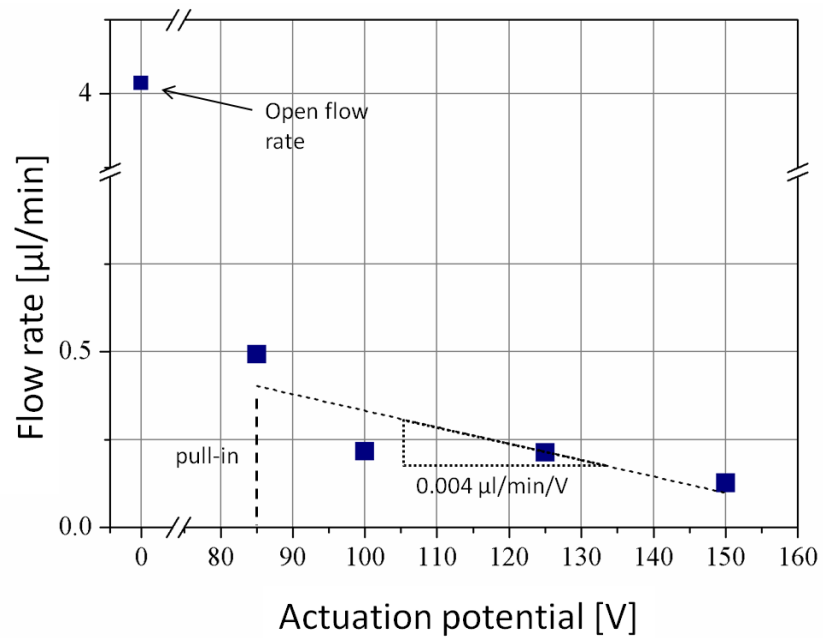


**Figure 2.29: Flow rate at different actuation potentials at 8 kPa inlet pressure for 250  $\mu\text{m}$  radius microvalve.**

Decrease in flow rate is the result of narrowing leakage path with increasing actuation potential. To examine this behavior, width of the leakage path is measured at different voltages. For this purpose, snapshots of the microvalves actuated by applying different potentials are taken and 3D maps are created based on the color intensity using ImageJ. Figure 2.30 illustrates the procedure and shows the change in the leakage path with the actuation potential.

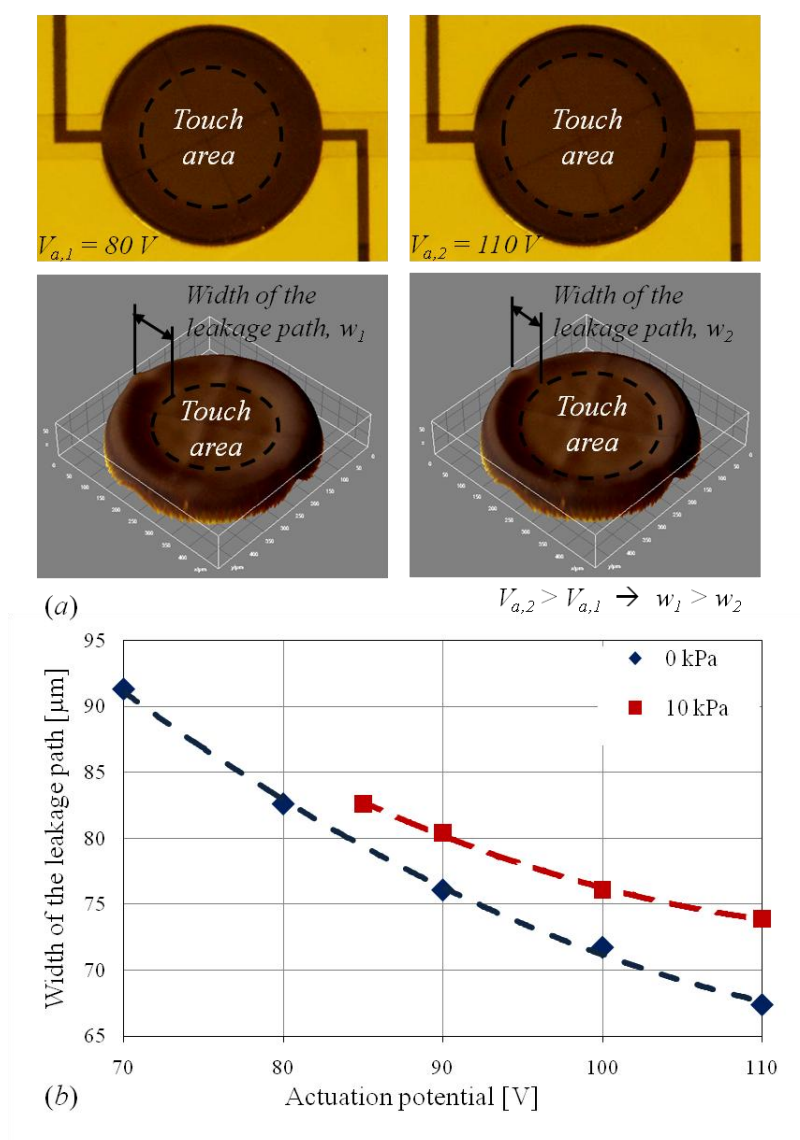


**Figure 2.30: (a) Snapshots of the microvalve taken at different actuation potentials and corresponding 3D maps. (b) Width of the leakage path versus the actuation potential.**

## 2.5 Conclusion

In this chapter, analysis, fabrication, and testing of a simple, in-plane, electrostatically actuated, parylene microvalves are presented in details. Fabricated microvalves are tested to determine pull-in and flow characteristics.

Test results show that the microvalves of radii ranging from 250  $\mu\text{m}$  to 450  $\mu\text{m}$  can be operated by applying voltages between 20-70 V with air and oil as working fluids. During the tests, lower pull-in voltages are observed for oil, compared to air. This result is the consequence of the difference between electrical permittivity of oil ( $\epsilon_{oil} = 3$ ) and air ( $\epsilon_{air} = 1$ ). According to the analysis, pull-in voltage becomes minimum for working fluids of dielectric constant around 3-5. Therefore, pull-in voltage measured for oil is the minimum possible actuation potential for the fabricated microvalves. On the other hand, it could not be possible to operate the microvalves with DI water. This is because of the high dielectric constant of water ( $\epsilon_{water} = 80$ ).

Flow tests of the microvalves are carried out with air as the working fluid. During the tests, no leakage is detected up to 4 kPa inlet pressure, when the valves are actuated applying 85 V potential. The leakage ratio increases to 17 % at 10 kPa inlet pressure under same operating conditions. It is also shown that the leakage decreases with increasing actuation potential. However, sensitivity of the leakage ratio to actuation potential becomes very low ( $10^{-3} \text{ V}^{-1}$ ), meaning that the leakage can be controlled precisely by the microvalve presented here.

Test results show that actuation potential strongly depends on the electrical properties of the working fluid. In addition to this, although the design can be used as a precise throttle valve, it cannot be used as an on/off switch due to its inherent leakage properties. Considering the advantages and the shortcomings of the device, possible applications are discussed and demonstrations are presented in chapter 4.

## CHAPTER 3

### A NORMALLY CLOSED ELECTROSTATIC MICROVALVE

In chapter 3, a simple normally open electrostatic microvalve was explained in detail. However, it was concluded that actuation potential is strongly dependent on the electrical properties of the working fluid. Additionally, leakage properties of the microvalve were not acceptable for on/off switching applications. Therefore, a novel microvalve is proposed to solve aforementioned problems in normally open electrostatic microvalve. Different from the previous design, the microvalve utilizes a normally closed structure.

This chapter presents the principles, analysis and design, fabrication, and characterization of this novel microvalve in details.

#### 3.1 Operating Principle of the Microvalve

Figure 3.1 illustrates this normally closed microvalve and its operation modes. The design involves an in-plane circular diaphragm, similar to the previous design. However, in this case the diaphragm is located at the bottom of the microchannel. An actuation chamber is located underneath this diaphragm. On top of the diaphragm, there exists a semi-circular wall suspending from the top of the microchannel. This wall acts as the wall seat during operation. In closed state, flow is blocked by this semi-circular wall. In open state, the diaphragm underneath is pulled-down, forming a gap between the wall and the diaphragm. Hence, the fluid can pass underneath the semi-circular wall. To pull-down the diaphragm, actuation potential is applied across the top electrode (on top of the diaphragm) and the bottom electrode (at the bottom of the actuation chamber). To allow the air escape during actuation, air vents are located at the top of the actuation chamber.

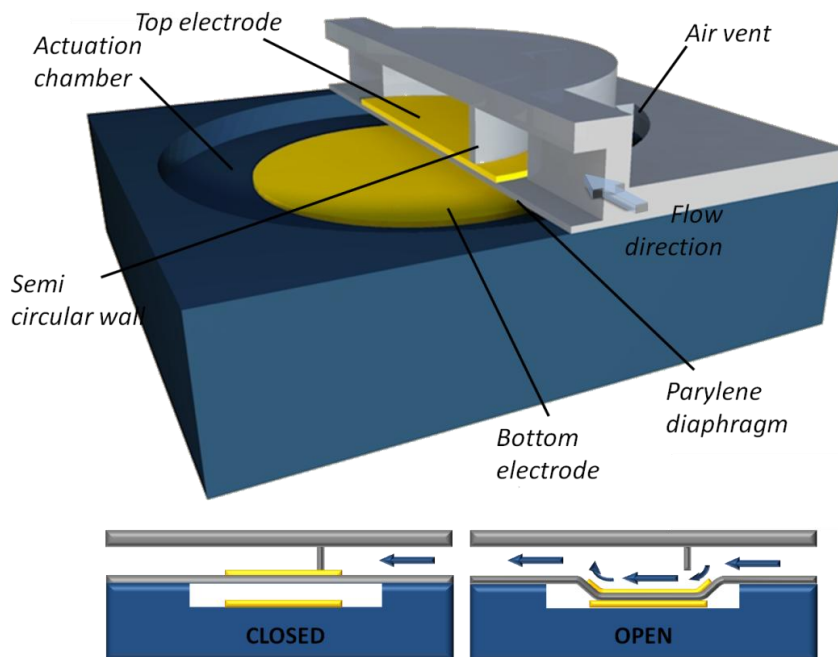


**Figure 3.1: Structure and open/closed states of the normally closed electrostatic microvalve.**

The flow rate across the microvalve is characterized by the amount of gap between the diaphragm and the semi-circular wall. This gap is controlled by the deflection of the diaphragm. There are two forces causing the diaphragm deflect; electrostatic force and the fluidic pressure. As voltage is applied across the electrodes, attractive electrostatic forces are generated pulling the diaphragm down. The diaphragm deflects more as the voltage is increased. At pull-in voltage, the diaphragm suddenly collapses down on the bottom of the actuation chamber (details of pull-in was explained in section 2.2). As the voltage is increased further, radius of the area, where the diaphragm touches the bottom, increases. The voltage, where the radius of this touch area is equal to the radius of the semi-circular wall, is defined as the actuation potential. At this potential, the gap underneath the diaphragm is at its maximum (Figure 3.2).



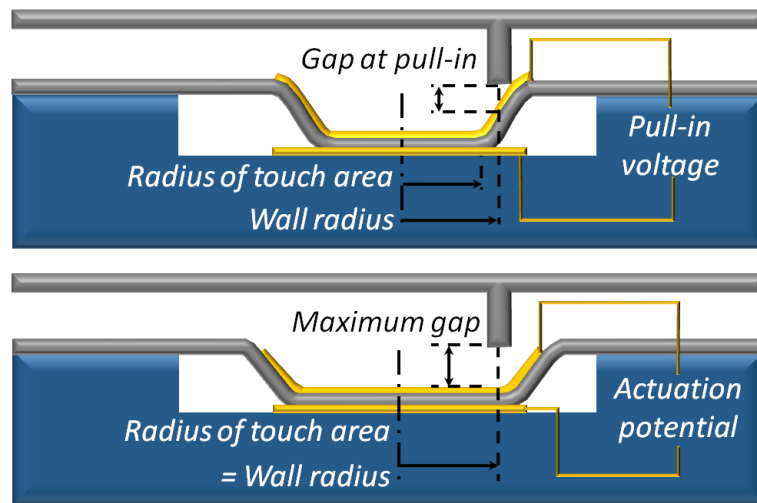


**Figure 3.2: Illustration of the actuation potential.**

As stated above, second force acting on the diaphragm is the fluidic pressure. The fluidic pressure also tends to deflect the diaphragm down when the microvalve is unpowered. This relatively increases the flow rate in closed state. In order to minimize the effects of the fluidic pressure, semi-circular wall is utilized. During operation, semi-circular wall confines the flow at the periphery of the diaphragm. This minimizes the bending moment caused by the fluidic pressure, preventing the deflection of the diaphragm in closed state.

The effect of the electrostatic force and the fluidic pressure are analyzed in the following section. Design dimensions are determined considering these effects.

### **3.2 Design of the Microvalve**

In the design of the microvalve, three major variables are considered: actuation potential, leakage ratio, and the response time. The objective in the design is to minimize all these parameters. Similar to the normally open microvalve, geometry of the microvalve and mechanical properties of the diaphragm material (parlylene-C) affect these parameters. Figure 3.3 shows the parameters affecting the microvalve

operation. Here it is important to note that, different from the normally open microvalve, electrical properties of the working fluid does not affect the actuation potential. This is simply because the dielectric media in the actuation chamber is always air, regardless of the working fluid. This unique property solves an important problem with electrostatic microvalves in LOC applications, where operating voltages strongly depend on working fluid.

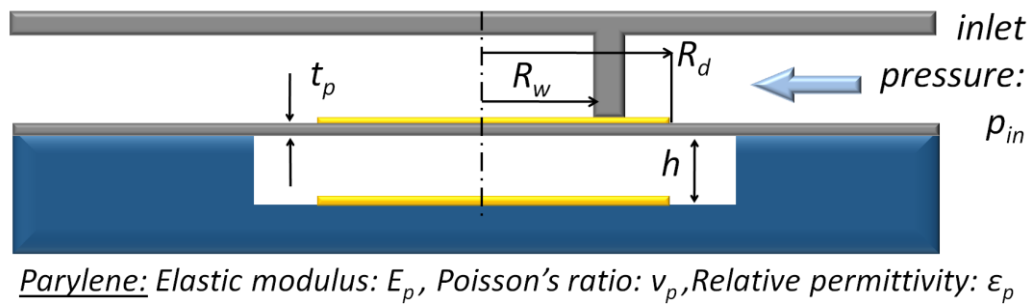


**Figure 3.3: Parameters affecting the operation of the normally closed microvalve.**

Actuation potential is defined above as the voltage, where the gap underneath the semi-circular wall is at its maximum. This voltage can be calculated by using equivalent diaphragm approach. This approach is originally developed for touch mode capacitive pressure sensors [103], where the touch area is related with the ambient pressure. Here, this approach is modified to correlate the touch area with the electrostatic forces on the diaphragm. According to this approach, an equivalent diaphragm with a smaller radius is defined. This equivalent diaphragm, which is barely touching the bottom at the center, is loaded with a central force, which is equal to the resultant of the forces on the original diaphragm. The difference between the radii of the original diaphragm and the equivalent diaphragm gives the radius of the touch area. Figure 3.4 shows the original and equivalent diaphragms with the loads on it.

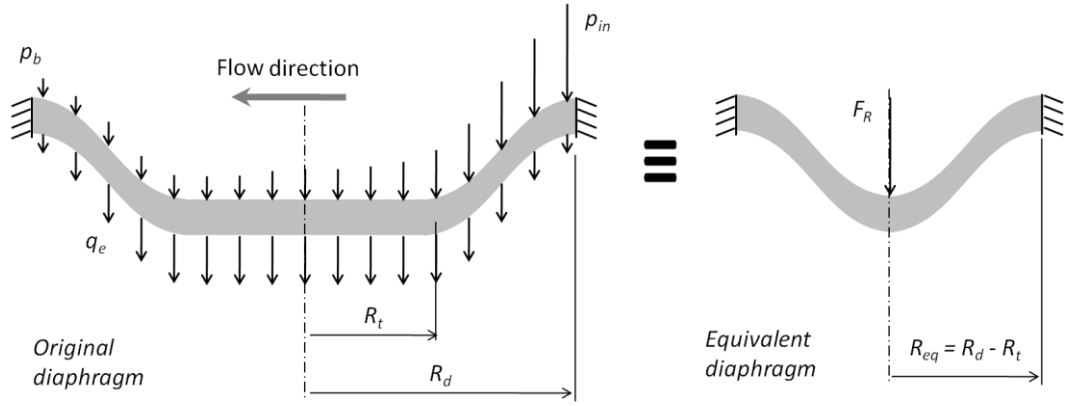


**Figure 3.4: Equivalent diaphragm approach. Fluidic pressure and the electrostatic load on the original diaphragm are shown at the top and at the bottom of the original diaphragm respectively.**

It should be noted that, for the microvalve to be open, touch radius ( $R_t$ ) should be equal to the radius of the semi-circular wall ( $R_w$ ). Therefore, using Timoshenko's formula [104] for large deflection of a clamped circular diaphragm under central load, it can be written that:

$$16Dh + \frac{191}{648} E_p t_p h^3 = \frac{F_R (R_d - R_w)^2}{\pi} \quad (3.1)$$

Here,  $h$  is the actuation chamber height,  $t_p$  is the diaphragm thickness,  $E_p$  is the elastic modulus of parylene, and  $D$  is the flexural rigidity of the diaphragm (3.2).

$$D = \frac{E_p t_p^3}{12(1 - \nu_p^2)} \quad (3.2)$$

where  $E_p$  is the elastic modulus of parylene,  $t_p$  is the diaphragm thickness, and  $\nu_p$  is the Poisson's ratio of parylene. As a result, actuation potential can be found using (3.1), if the resultant force is expressed in terms of the voltage.

On the original diaphragm, electrostatic load ( $q_e$ ) is also non-uniform. As stated in (2.10),  $q_e$  varies depending on the amount of deflection and the media between the electrodes. Therefore,  $q_e$  can be stated as:

$$q_e = \begin{cases} \frac{\varepsilon_0 V_a^2}{2 \left( (h - \omega) + \frac{t_p}{\varepsilon_p} \right)^2} & \omega \in [0, h[ \\ \frac{\varepsilon_0 \varepsilon_p V_a^2}{2 t_p^2} & \omega = h \end{cases} \quad (3.3)$$

where  $\varepsilon_0$  is the permittivity of vacuum,  $V_a$  is the actuation potential,  $h$  is the actuation chamber height,  $t_p$  is the diaphragm thickness,  $\varepsilon_p$  is the permittivity of parylene, and  $\omega$  is the vertical displacement.

Similarly, fluidic pressure is also non-uniformly distributed on the diaphragm. Fluidic pressure varies from inlet pressure ( $p_{in}$ ) to back pressure ( $p_b$ ) across the valve. Therefore, in order to simplify the solution some assumptions are made. The first assumption is related with the fluidic pressure on the diaphragm. It should be noted that the fluidic pressure acts in the same direction with the electrostatic force. Therefore, considering only the actuation potential, the worst case is the no-flow case, where the fluidic pressure is zero. Next assumption is related with the electrostatic force. Examining (3.3) reveals that electrostatic load becomes maximum on touch area. Considering the fact that the electrostatic force is dominated by the load on touch area, and fluidic pressure is zero, resultant force can be stated as:

$$F_R = \frac{\pi \varepsilon_0 \varepsilon_p V_a^2 R_w^2}{2 t_p^2} \quad (3.4)$$

Combining (3.1) and (3.4) gives the actuation potential under no flow condition (3.5).

$$V_a = \sqrt{\frac{2t_p^2}{\varepsilon_0 \varepsilon_p R_w^2 (R_d - R_w)^2} \left[ 16Dh + \frac{161}{648} E_p t_p h^3 \right]} \quad (3.5)$$

Leakage ratio is defined as the ratio of the flow rate in closed state to that in open state in chapter 2. However, it is mentioned above that the flow rate across the microvalve is mainly characterized by the gap between the semi-circular wall and the diaphragm. Therefore, definition of the leakage ratio can be modified as the ratio of the opening area in open state to that in closed state. Considering the direction of the main stream, this area should be normal to the flow in order to describe the leakage correctly. Consequently, the opening area is stated as the area underneath the semi-circular wall projected on the central plane normal to the flow (Figure 3.5). Hence, the leakage ratio is redefined as:

$$L = \frac{A_{off,projected}}{A_{on,projected}} \quad (3.6)$$

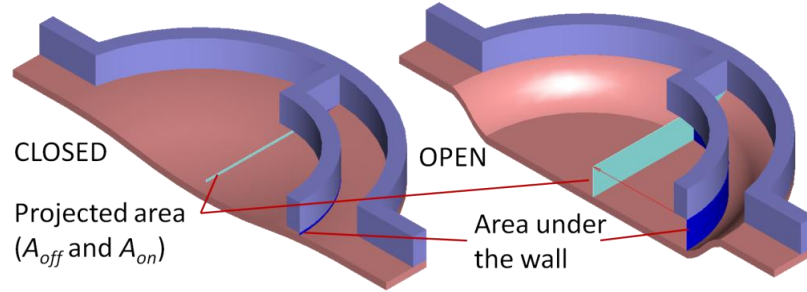


**Figure 3.5: Projected area underneath the semi-circular wall in open and closed states.**

In order to find the projected areas, the distance between the diaphragm and the wall should be found. For this purpose, loading cases are simplified. For the closed state, loading is approximated by uniform fluidic pressure acting on a solid membrane of radius  $R_d$ , between  $R_w$  and  $R_d$  (Figure 3.6). Additionally, back pressure is assumed to be zero. The loading approximation simplifies the solution, while overestimating the

deflection. However, the objective is to compare different cases to find the optimum radii not to find the exact leakage ratio. Therefore, the approximation can safely be used for optimization purposes. Using the Roark's formula [105], the central diaphragm deflection can be found as

$$\begin{aligned} \omega_c &= \frac{p_{in} R_d^4}{2D} (L_{14} - 2L_{11}) \\ L_{11} &= \frac{1}{64} \left\{ 1 + 4 \left( \frac{R_w}{R_d} \right)^2 - 5 \left( \frac{R_w}{R_d} \right)^4 - 4 \left( \frac{R_w}{R_d} \right)^2 \left[ 2 + \left( \frac{R_w}{R_d} \right)^2 \right] \ln \frac{R_w}{R_d} \right\} \\ L_{14} &= \frac{1}{16} \left[ 1 - \left( \frac{R_w}{R_d} \right)^4 - 4 \left( \frac{R_w}{R_d} \right)^2 \ln \frac{R_w}{R_d} \right] \end{aligned} \quad (3.7)$$

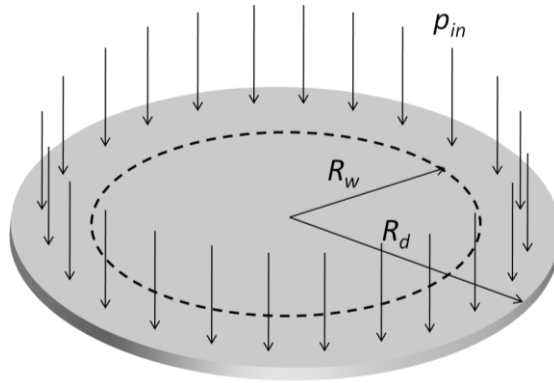


**Figure 3.6: Approximation of the fluidic pressure on the diaphragm.**

Assuming that the deflection profile is linear (Figure 3.7), projected area can be found as

$$A_{off} = R_d \omega_c \left[ 1 - \left( \frac{R_w}{R_d} \right)^2 \right] \quad (3.8)$$

This applies only if the central deflection is smaller than the chamber height  $h$  (Figure 3.7 a). Otherwise, the diaphragm sits on the bottom, defining a touch radius  $R_t$  (Figure 3.7 b). In this case,  $R_t$  can be approximated as

$$R_t = \frac{R_d (\omega_c - h)}{\omega_c} \quad (3.9)$$

Consequently, assuming a linear deflection profile beyond the touch radius, projected area can be found as

$$A_{off} = \begin{cases} \frac{(R_d^2 - R_w^2)h}{(R_d - R_{tp})} & \text{if } R_t < R_w \\ (R_{tp} + R_d)h & \text{if } R_t \geq R_w \end{cases} \quad (3.10)$$

The open state of the valve is defined as the state, where the diaphragm touches the bottom of the actuation chamber over a radius of  $R_w$ . Therefore, projected area in open state can be found as

$$A_{on} = (R_w + R_d)h \quad (3.11)$$

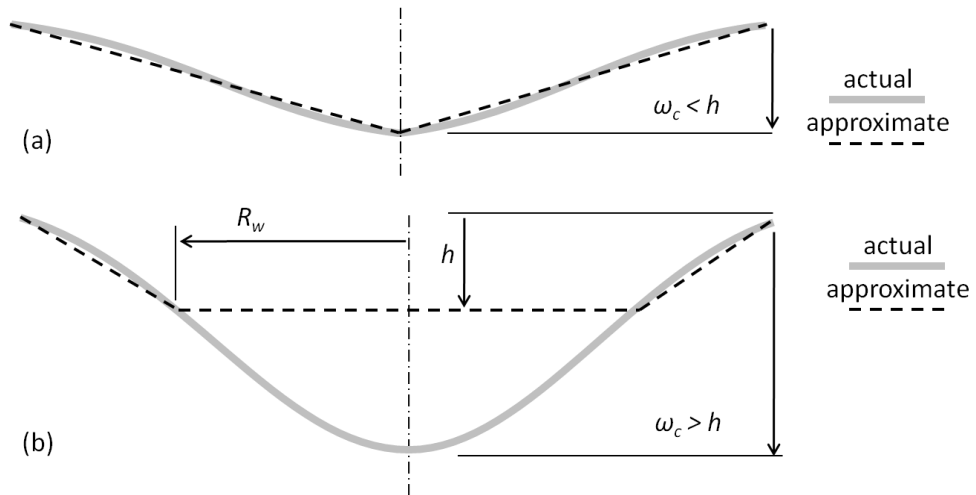
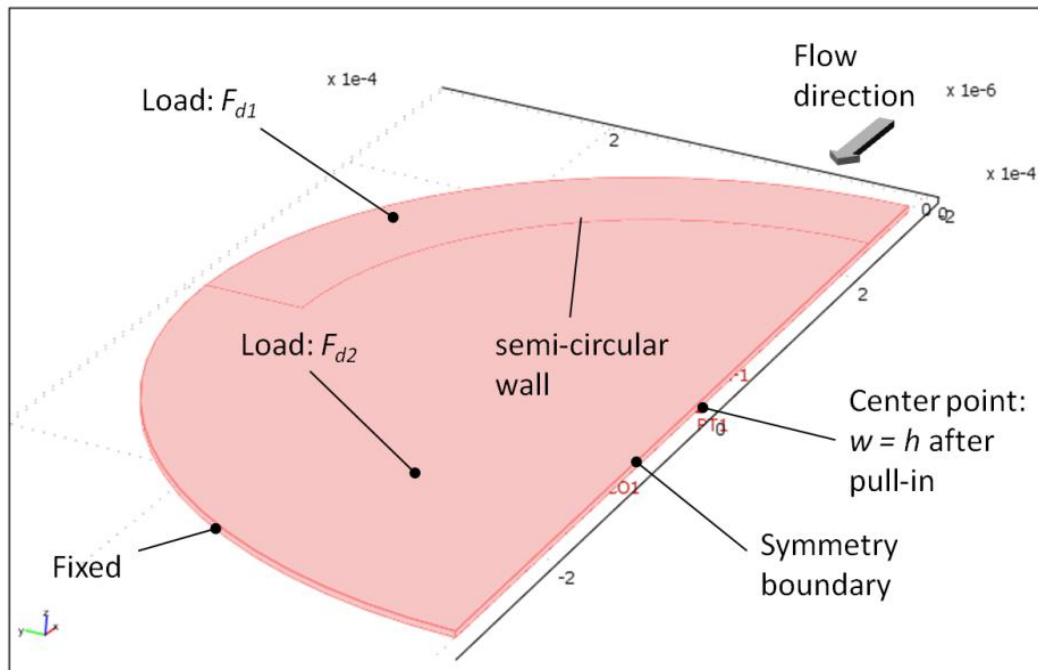


**Figure 3.7: Deflection profile of the diaphragm caused by the fluidic pressure.**

To validate this approximation, the diaphragm is modeled using finite element method. Figure 3.8 shows the boundary conditions on the diaphragm. Here, forces  $F_{d1}$  and  $F_{d2}$  are defined as

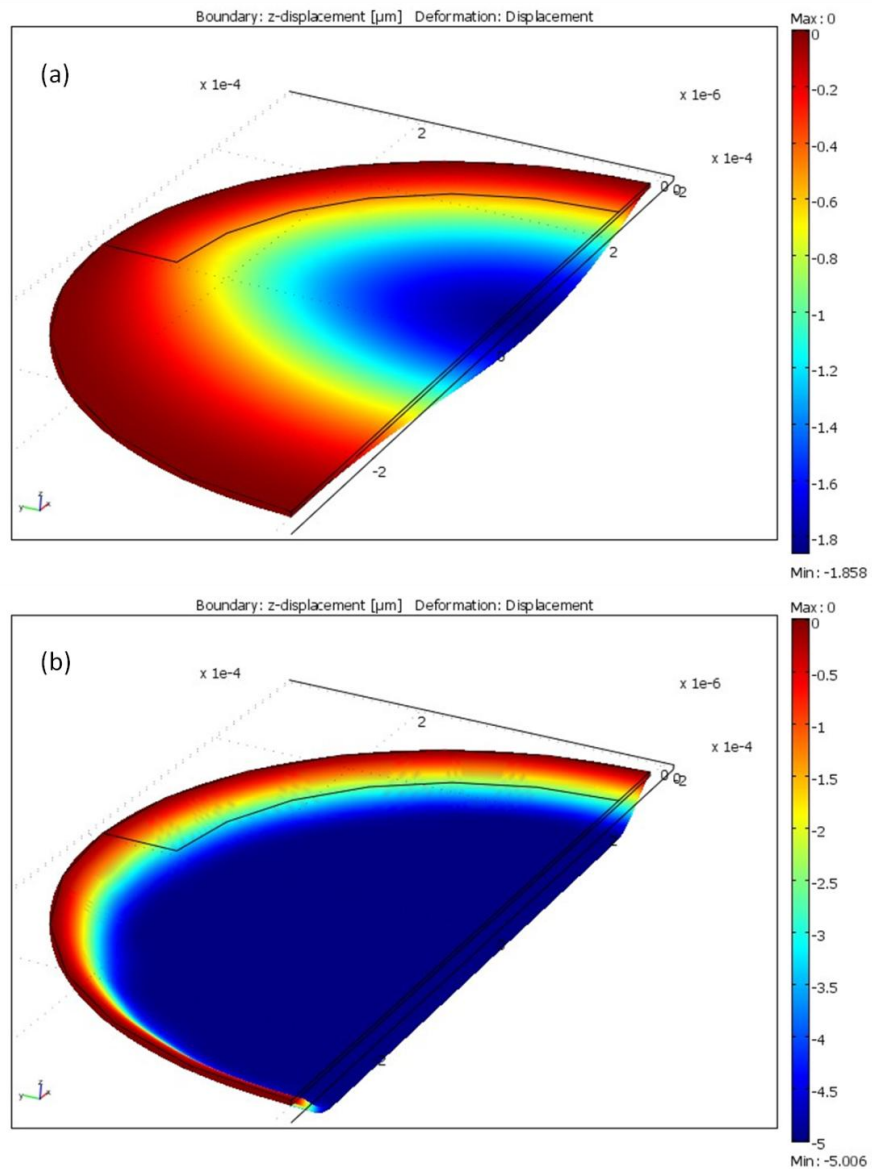
$$\begin{aligned} F_{d1} &= -p_{in} - q_e \\ F_{d2} &= -p_b - q_e \end{aligned} \quad (3.12)$$

where  $p_{in}$  and  $p_b$  are inlet and back pressures respectively, and  $q_e$  is the electrostatic pressure on the diaphragm, which is defined by equation (3.3). Using the finite element model, diaphragm deflection is solved in open (where actuation potential defined in (3.5) is applied) and closed (where zero potential is applied) states of the microvalves. Figure 3.9 shows the deflection of 300  $\mu\text{m}$  radius diaphragm with 240  $\mu\text{m}$  radius semi-circular wall in closed and open states.



**Figure 3.8: Boundary definitions in finite element analysis of normally closed microvalve diaphragm.**

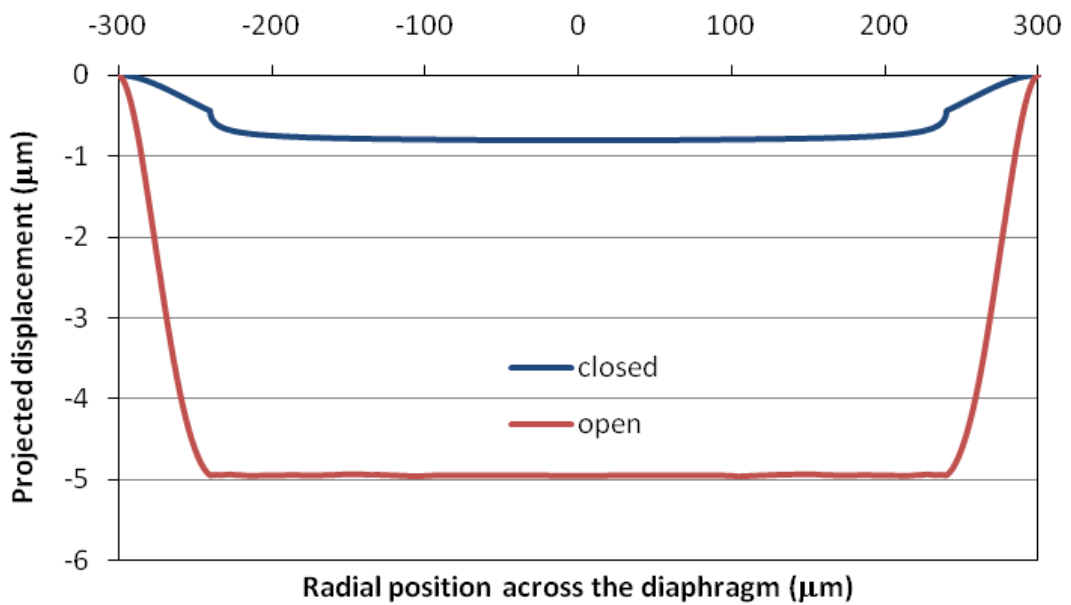




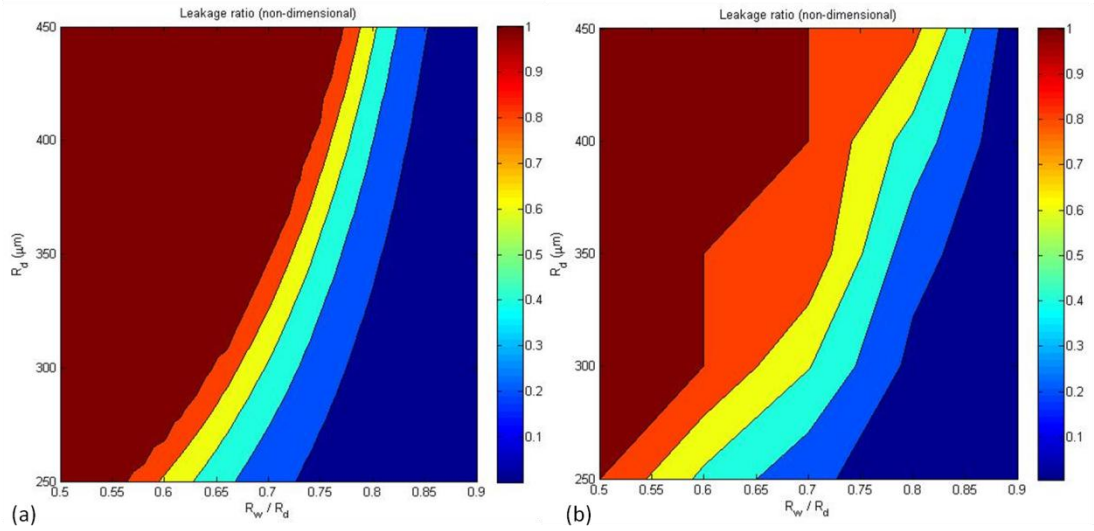
**Figure 3.9: Diaphragm deflection in (a) closed and (b) open states of the microvalve. Diaphragm radius, semi-circular wall radius, and inlet pressure are  $300\ \mu\text{m}$ ,  $240\ \mu\text{m}$ , and  $10\ \text{kPa}$  respectively. Height of the actuation chamber is  $5\ \mu\text{m}$ .**

Figure 3.10 shows the deflection profile projected along the semi-circular wall. Area between the projected deflection curve and the horizontal axis gives the projected area in open and closed states respectively. With this data, leakage ratio is calculated using equation (3.6). Leakage ratio computed using the finite element analysis is

compared with the approximated leakage ratio, which is found by dividing equation (3.10) with equation (3.11). Figure 3.11 plots the leakage ratio computed for a range of microvalves at a specific inlet pressure, using finite element analysis and the approximate solution. Examining the contour plots shows that the approximation overestimates the leakage ratio, as expected. However, in low leakage range (denoted by the dark blue area) the approximation agrees well with the finite element analysis solutions. Therefore, approximate solution can be safely used since low leakage range is the target in this design.



**Figure 3.10: Projected deflection in closed and open states of the microvalve. Diaphragm radius, semi-circular wall radius, and inlet pressure are 300 μm, 240 μm, and 10 kPa respectively. Height of the actuation chamber is 5 μm.**



**Figure 3.11: Leakage ratio computed using (a) approximate deflection model and (b) finite element analysis.**

The last variable, response time, describes how fast the microvalve reacts to electrostatic actuation. This is directly dependent on the compliance of the diaphragm (3.13). In case of a stiff diaphragm, the response time will be low. However, this excessively makes the operating potential high.

$$c = \frac{R_d^4}{D} \quad (3.13)$$

For optimized operation of the valve, equations (3.5), (3.6) and (3.13) should be minimized. To solve this multi-objective problem, an aggregate objective function (*AOF*) which is a linear combination of leakage ratio, actuation potential, and compliance is defined (3.14).

$$AOF = \lambda_1 L + \lambda_2 \tilde{V}_a + \lambda_3 \tilde{c} \quad (3.14)$$

Here  $\tilde{V}_a$  and  $\tilde{c}$  are normalized operating voltage and compliance respectively. Maximum of  $V_a$  and  $c$  in the search range are used as normalization bases respectively. In (3.14),  $\lambda_i$  are relative weights of the individual objectives.

As mentioned before, geometrical parameters affecting the operation of the valve are shown in Figure 3.3. Among these dimensions, actuation chamber height  $h$  and the diaphragm thickness  $t_p$  are restrained by the fabrication capabilities and the application. Therefore, diaphragm radius  $R_d$  and the semi-circular wall radius  $R_w$  are selected as design dimensions. To determine the design dimensions,  $AOF$  is solved at specific inlet pressure levels assuming  $\lambda_i = 1$ . During calculation, actuation chamber height and diaphragm thickness are taken as  $5 \mu\text{m}$  and  $3.5 \mu\text{m}$  respectively, regarding the fabrication limitations explained in the following section. Figure 3.12 shows the contour plots of  $AOF$  obtained for different inlet pressures (back pressure is assumed to be zero). The results show that  $R_w$  should be increased as inlet pressure increases, to minimize  $AOF$ . However, the results also show that optimum solution region (closed dark blue area in Figure 3.12) remains substantially unchanged in a wide range of inlet pressures. Therefore, it can be concluded that the design is relatively insensitive to inlet pressure level. Effect of the relative importance of each objective is also investigated by varying  $\lambda_i$ . Figure 3.13 shows the resulting  $AOF$  for different weight combinations. The results imply that minimum of  $AOF$  does not change significantly. However, dependency of  $AOF$  on relative weights is more important compared to the inlet pressure.

In this study, relative importance of each objective are decided to be equal. On the other hand, for specific applications these relative weights can be altered for design flexibility. For instance, if the microvalves are intended for flow regulation rather than flow switching, relative weight of the leakage ratio can be reduced. On the other hand, considering the power sources, one may keep relative weight of the actuation potential large to further minimize the voltage. Additionally, tuning the weight of the compliance changes the latching properties of the microvalve. If the relative weight of the compliance is kept small, a less stiff diaphragm will be designed. If the diaphragm is designed excessively compliant, pull-in and pull-out times will increase. A longer pull-out time means that the diaphragm would remain closed for a specific period after actuation potential is switched off.

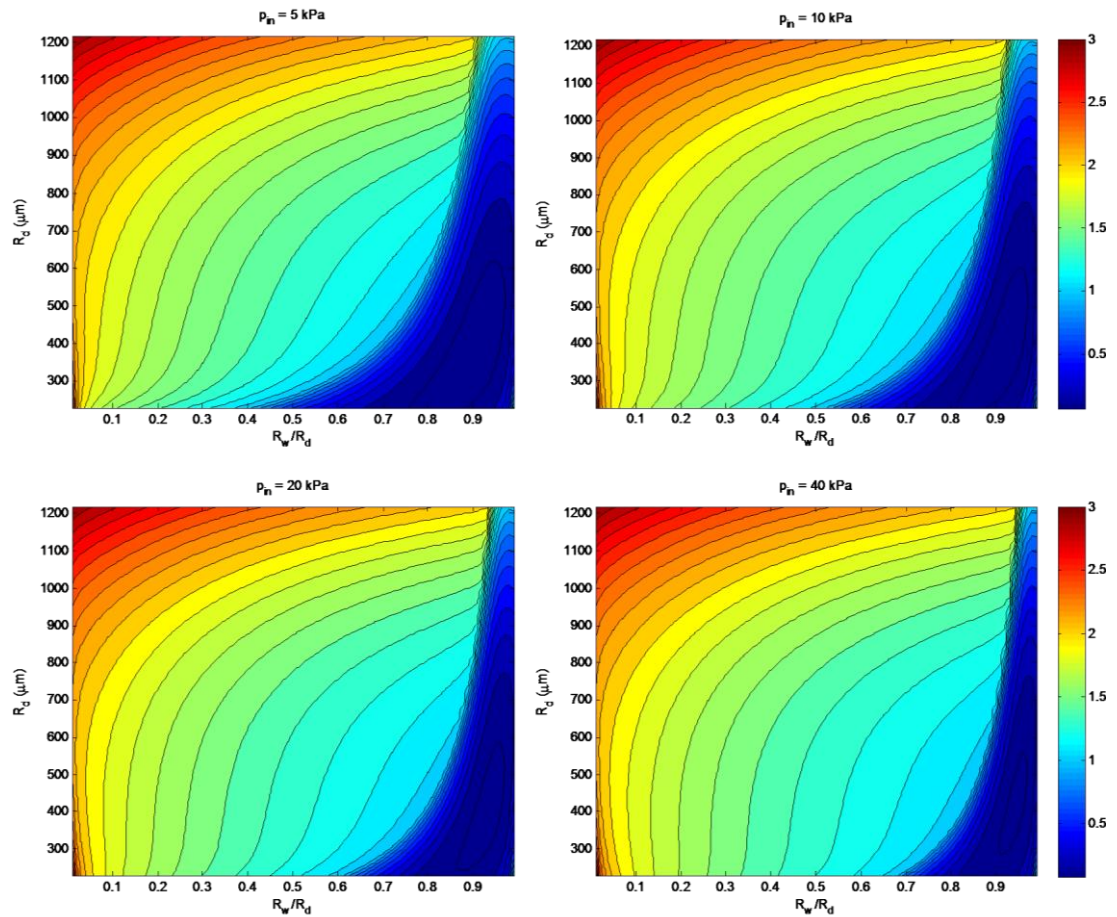


Figure 3.12: Contour plot of AOF for different inlet pressure levels.

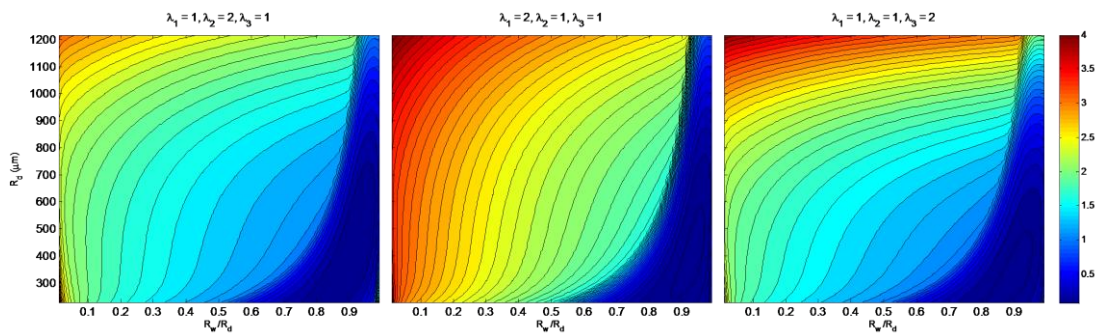
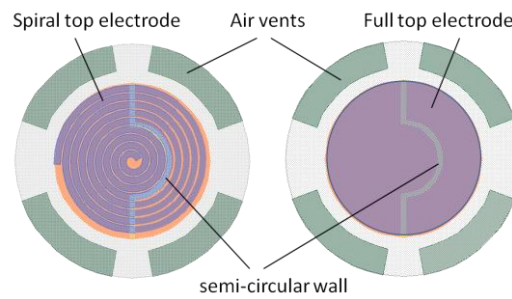
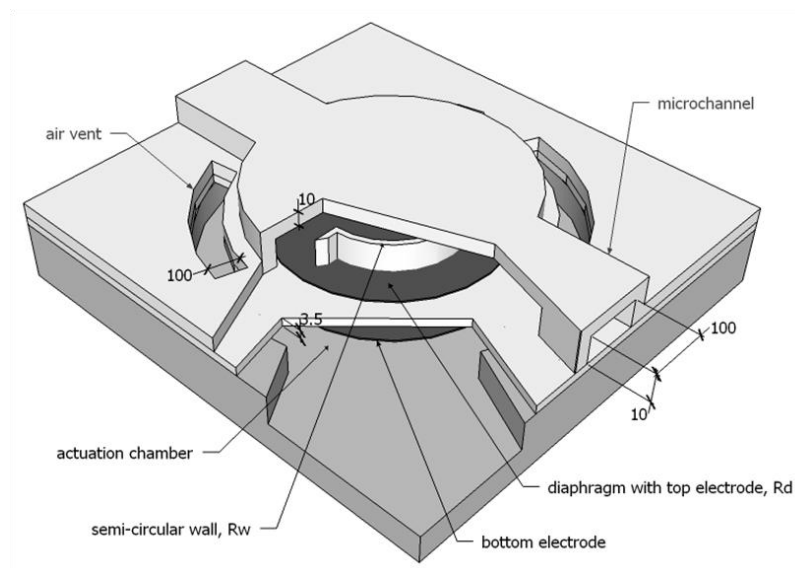


Figure 3.13: Contour plot of AOF for different relative weights of objectives.

For the characterization of the microvalves, prototypes are fabricated with the design dimensions found by minimizing the *AOF* for 20 kPa and 40 kPa inlet pressures. In addition to these, microvalves with varying diaphragm and semi-circular wall radii are fabricated to analyze their effect on the operation. Additionally, a spiral top electrode design is utilized to improve the resilience of the diaphragm. Figure 3.14 sketches the top views of the microvalves with spiral top electrode and full top electrode. Dimensions of the fabricated microvalves are labeled in Figure 3.15. All variations in the design are listed in Table 3.1.



**Figure 3.14: Top view of the microvalves with spiral and full top electrodes.**



**Figure 3.15: Design dimensions of the normally closed electrostatic microvalve.**

**Table 3.1: Dimension variations of designed normally closed microvalves.**

	Diaphragm radius, $R_d$ [ $\mu\text{m}$ ]	Semi-circular wall radius, $R_w$ [ $\mu\text{m}$ ]	Top electrode	Notes
1.	410	380	Full	20 kPa capacity
2.	410	385	Full	40 kPa capacity
3.	410	350	Full	
4.	410	250	Full	
5.	410	150	Full	
6.	410	0	Full	
7.	410	350	Spiral	
8.	410	250	Spiral	
9.	410	150	Spiral	
10.	410	0	Spiral	
11.	300	250	Full	
12.	300	150	Full	
13.	300	0	Full	
14.	300	250	Spiral	
15.	300	150	Spiral	
16.	300	0	Spiral	

### 3.3 Fabrication of the Microvalves

Unlike normally open electrostatic microvalves, combination of bulk micromachining with surface micromachining techniques are used to fabricate the prototypes. As stated before, surface micromachining involves successive deposition and patterning of thin layers on a substrate. Different from surface micromachining, bulk micromachining involves patterning of the substrate material, rather than a deposited layer. Utilizing combination of surface and bulk micromachining techniques, prototypes are fabricated on 4" diameter silicon wafers.

Similar to fabrication of normally open microvalves, multiple prototypes with varying dimensions are fabricated on the same wafer. For this purpose, layout of each variation is created again using Tanner<sup>®</sup> L-Edit<sup>®</sup> software. Figure 3.16 shows a representative layout for one of the prototypes listed in Table 3.1. The same configuration is used for fabrication of all prototypes. To manufacture a batch of prototypes using these masks, multiples of each microvalve are laid out on the same mask set. Layout of the whole wafer on these mask sets is presented in Figure A.6.

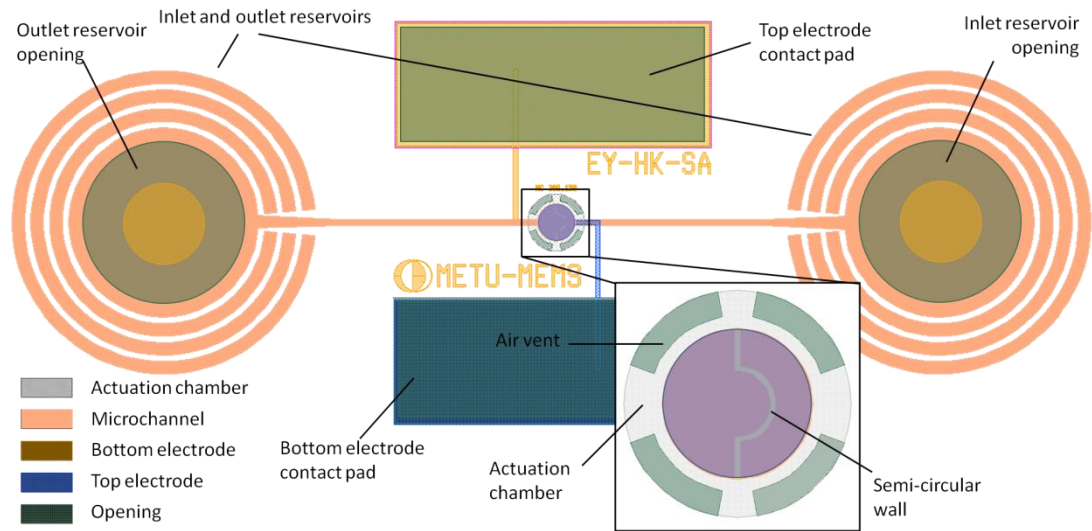


**Figure 3.16: Layout of the microvalve characterization prototype.**

### 3.3.1 Fabrication Process Flow

Total of 5 masks are used in fabrication of normally closed microvalves. Layouts of these masks are presented in APPENDIX A. For the fabrication of normally closed microvalves, 4" diameter silicon wafers are used as substrates. Figure 3.17 illustrates the fabrication process flow.

The first step in fabrication is the formation of the actuation chamber on the substrate. For this purpose, silicon wafer is coated with a thin photoresist layer by spinning. After then, this photoresist layer is exposed using the actuation chamber mask (Figure A.7) and developed successively. In this process, an image reversal photoresist is used to imprint the negative tone of the clear field actuation chamber mask. As a result of this process, photoresist is removed at actuation chamber sites. Afterwards, silicon substrate is etched by deep reactive ion etching (DRIE) by using the photoresist layer as the mask. At the end of DRIE process, recesses at actuation chamber sites are created. After DRIE process, masking photoresist layer and the polymer layer coated during the process are removed under O<sub>2</sub> plasma. One important point in formation of the actuation chamber is the tapered side walls. Tapered side walls facilitate conformity of the electrode layer in the next step.



Without taper angle, it may not be possible to have contact to the bottom electrode embedded in the actuation chamber. Figure 3.15 shows scanning electron microscope (SEM) image of the actuation chamber and the tapered side wall.

After forming of the actuation chamber, a thin silicon oxide layer is deposited on the wafer. This layer provides insulation between the bottom electrode and silicon substrate.

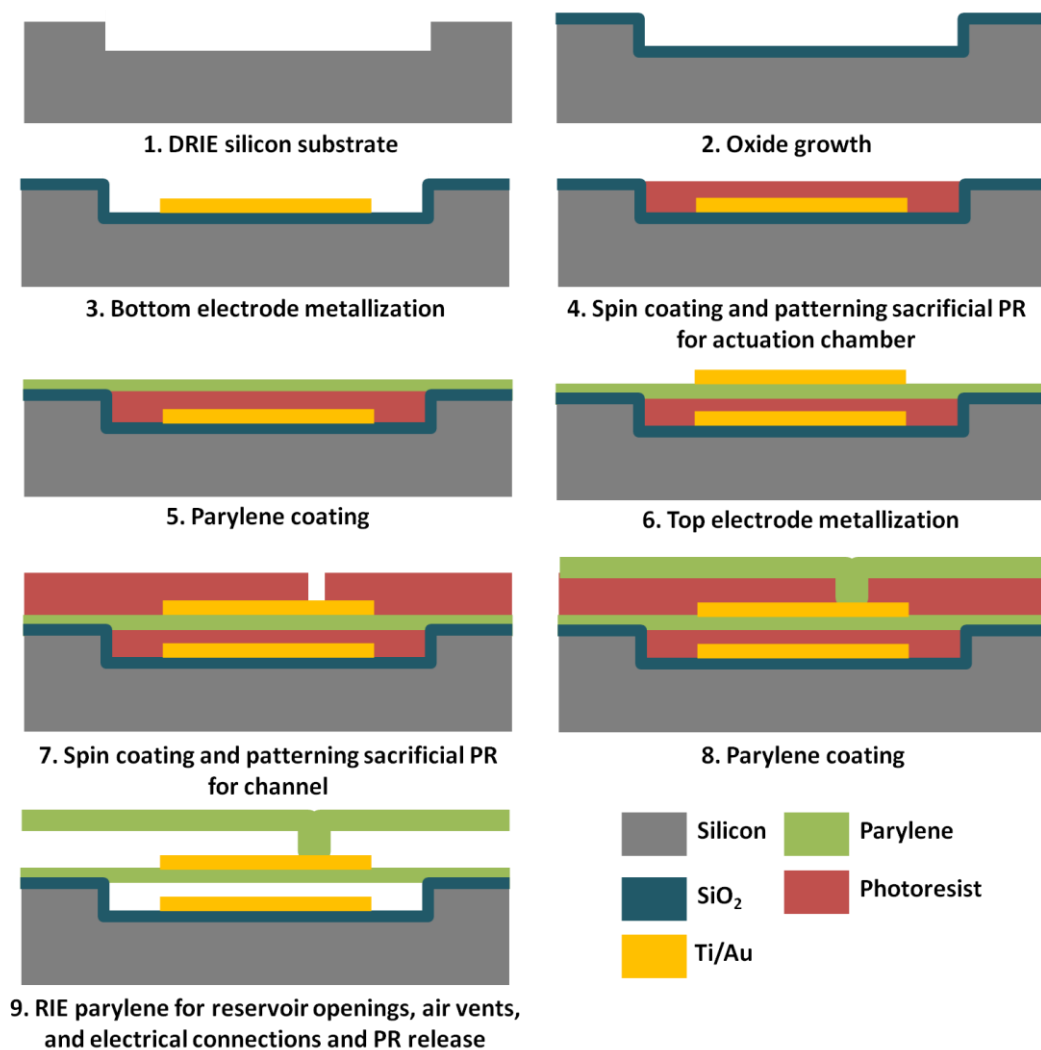


**Figure 3.17: Fabrication flow of the normally closed microvalves.**

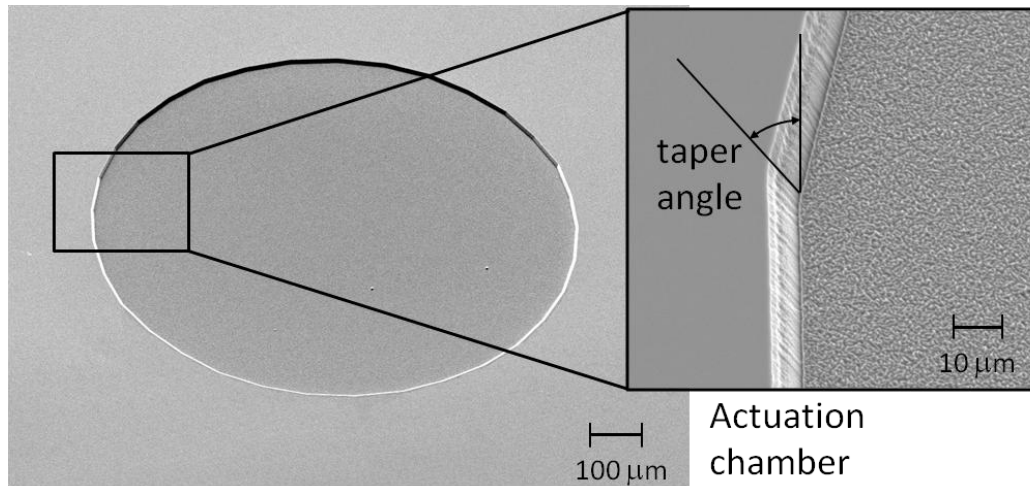


**Figure 3.18: SEM image of the actuation chamber showing tapered side wall.**

As the next step, bimetallic Ti/Au layer is sputtered on the substrate. After sputtering, wafer is spin-coated with a photoresist layer. This layer is then exposed using bottom electrode mask (Figure A.8) and developed successively. Underlying Ti/Au layer is patterned by chemical etching using this photoresist layer as the mask.

In the next step, recesses defining the actuation chamber (Figure 3.18) are filled with a sacrificial photoresist layer. In this step, a thick positive-tone photoresist layer (thickness equal to the depth of the recess) is spun and patterned, using the actuation chamber mask (Figure A.7). As a result of this process, replicas of the actuation chambers are imparted on the substrate. Following this step, wafer is coated with 2.5 μm thick parylene layer, which defines the diaphragm. Before parylene coating, sacrificial photoresist layer should be hard baked properly, due to reasons stated in section 2.3.1. However, hard baking causes the photoresist shrink down forming a rim at the periphery of the actuation chamber. Although the height of the rim is comparable with the height of the actuation chamber, it is less than the height of the microchannel (10 μm). Consequently, effect of the rim on flow rate can be ignored. Figure 3.19 shows the profile of the recess and the sacrificial photoresist.

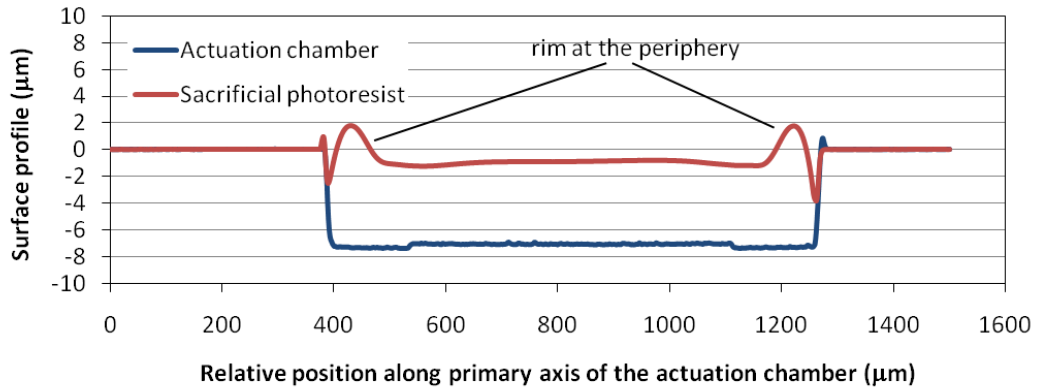


**Figure 3.19: Surface profile of the actuation chamber and filling photoresist layer measured used Veeco Dektak 8 profiler.**

The next step in fabrication is metallization of the top electrodes. For this purpose, wafer is coated with 150 nm thick Ti/Au bimetallic layer by sputtering. Afterwards, the wafer is spin coated with a thin photoresist layer. This layer is exposed using the top electrode mask (Figure A.10) and developed. Using this photoresist layer as the mask, Ti/Au layer is patterned by chemical etching.

After metallization of the top electrodes, a 10 µm thick sacrificial photoresist layer is spun and patterned to define reservoirs, microchannels, and semi-circular walls in the valve chambers. Channel mask (Figure A.9) is used for this purpose. Afterwards, a thick parylene layer (10 µm) is coated on this photoresist layer.

Next step in fabrication is etching the reservoir and contact pad openings, and the air vents. For this purpose, 30 µm thick photoresist layer is spun and patterned successively using the opening mask (Figure A.11). Underlying parylene is etched at opening sites by RIE process using this photoresist layer as the mask.

After parylene etching, processed wafer is diced along the dicing lines (Figure A.6). After dicing, individual dies are immersed in still acetone for 2 days, to remove sacrificial photoresist layer. Afterwards, the dies are treated with IPA and methanol successively to release the prototypes. Figure 3.20 shows the process wafer before

parlylene etching step. Details of the fabrication and recipes used in processes are given in Table B.2.

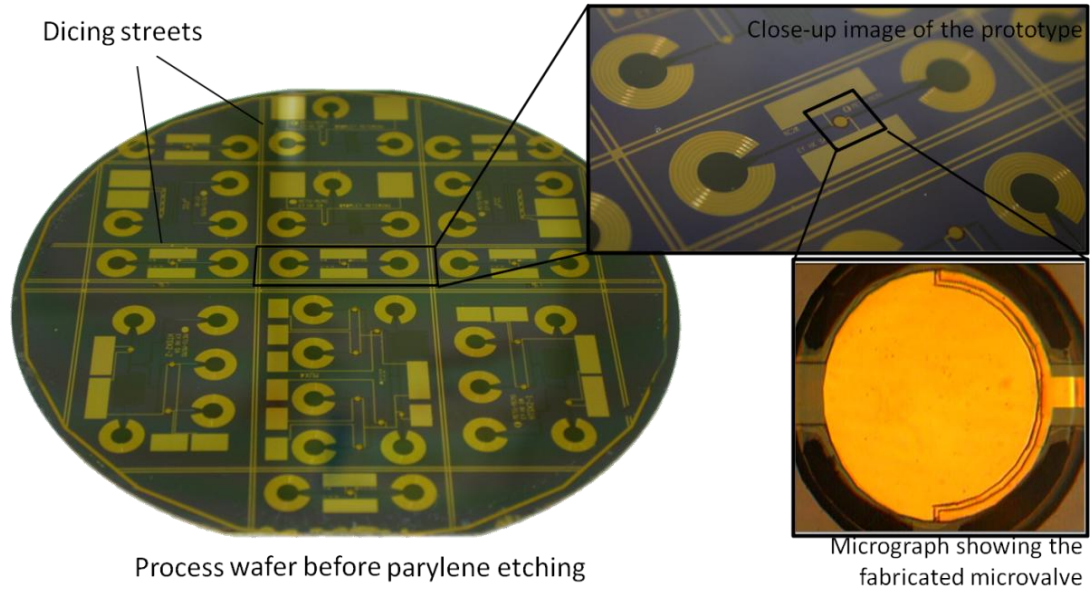


**Figure 3.20: Process wafer before parylene RIE step. Close-up view of a single prototype and micrograph of the microvalve are shown.**

### 3.4 Characterization of the Microvalves

Fabricated prototypes are tested to determine pull-in and leakage behavior with air and water as the working fluids. Pull-in tests are carried out under no-flow condition to investigate the effect of the working fluid. For pull-in tests with DI water, microchannels are filled with the working fluid by capillary action at first (Figure 2.23). During pull-in tests carried out on the prototypes, it is observed that the diaphragm can be pulled down by applying dc potential even when the working fluid is water. However, in case of water, bubbles are generated at the top electrode surface almost immediately after application of the potential. To solve this problem, top electrode is covered by a thin insulating parylene layer. However, this additional layer causes adhesion of the semi-circular wall in the next step. To figure out this

problem each microvalve is treated with 5 % Microsoap solution (Micro-90 concentrated cleaning solution and DI water), which aggravates adhesion of parylene. Afterwards, potential is gradually increased until pull-in is observed. Pull-in voltages are measured around 45 V for microvalves with 410  $\mu\text{m}$  radius diaphragm, while 65 V for 300  $\mu\text{m}$  radius diaphragm, independent of the working fluid. After pull-in, potential is increased further until the radius of the touch area becomes equal to the radius of the semi-circular wall. Figure 3.21 shows the snapshots of a specific microvalve (410  $\mu\text{m}$  diaphragm radius, 350  $\mu\text{m}$  semi-circular wall radius, and spiral top electrode) taken at different actuation potential levels. In color micrographs, due to refractive effect of relatively thick parylene layer over the top electrode, it could not be possible to detect the touch area clearly. However, after enhancing the contrast and converting the micrographs to binary images, touch area becomes distinguishable. Radii of the touch area at different potential levels are measured accordingly. Image processing tool ImageJ is used for processing and analysis of the snapshots.

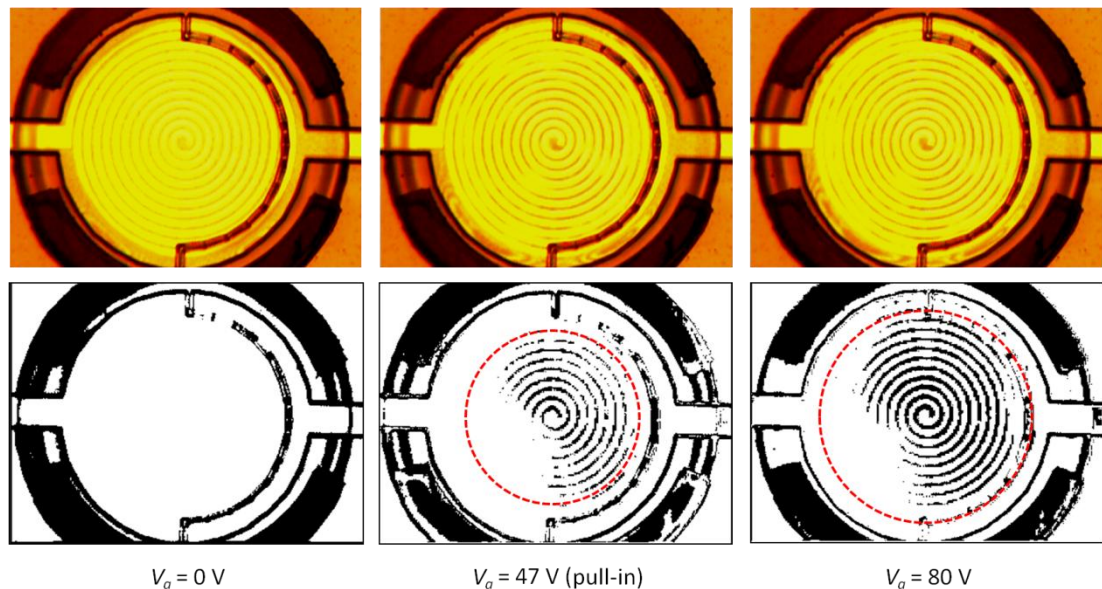


**Figure 3.21: Snapshots of the microvalve at different actuation potentials. Dashed circle denotes the touch area after pull-in. Diaphragm radius and semi-circular wall radius are 410  $\mu\text{m}$  and 350  $\mu\text{m}$  respectively.**

Figure 3.22 plots the radius of the touch area versus potential for a specific microvalve. Examining the figure reveals that the actuation potential required to achieve a touch area is higher compared to the theory. This result is expected to be arising from non-ideal boundary conditions of the diaphragm. During analysis, it was assumed that the diaphragm is clamped at its periphery. However, in reality the diaphragm is suspended underneath the microchannel. Although thickness of the parylene layer forming the channel is higher than the thickness of the diaphragm, it still tends to bend down together with the diaphragm under electrostatic loading. As a result, an additional stiffness term is introduced, which increases the actuation potential in turn.

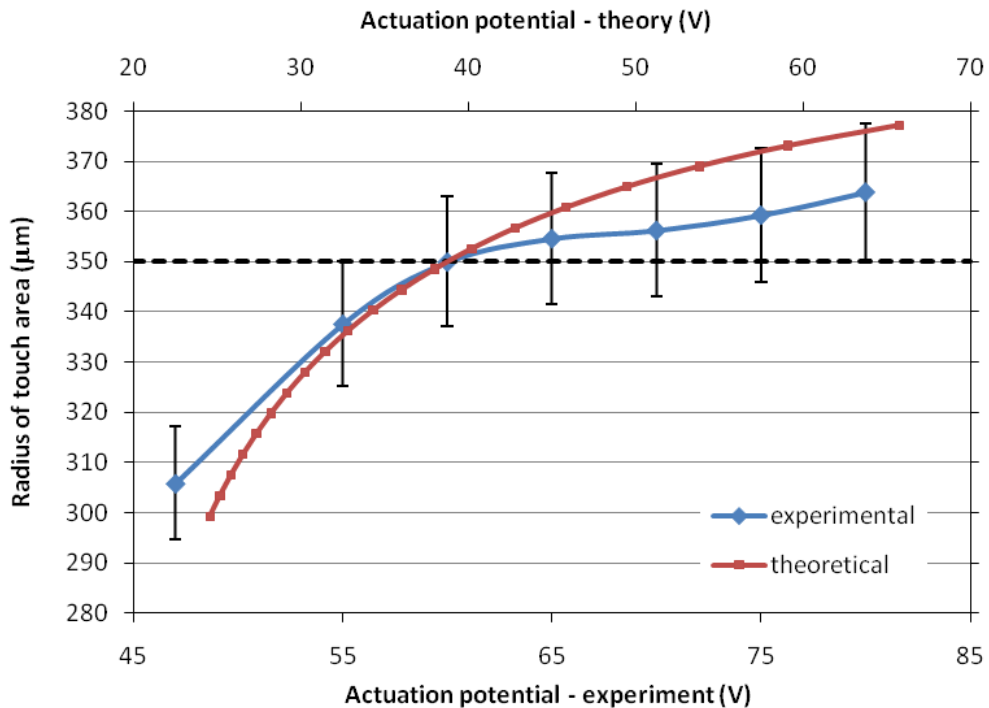


**Figure 3.22: Change in the touch area versus the actuation potential for the microvalve with 410 µm radius diaphragm. Horizontal dashed line denotes the radius of the semi-circular wall.**

After observing the touch area, potential is gradually decreased until the diaphragm bounces back. Potential level at this point is recorded as the pull-out voltage. As expected in electrostatic actuators, hysteresis behavior is observed. Pull-out is observed at potential levels, which are significantly lower than pull-in voltages. Table 3.2 lists the pull-in and pull-out voltages for the microvalves with 410  $\mu\text{m}$  and 300  $\mu\text{m}$  diaphragm radii. Here, it is interesting to note that pull-in voltages are measured to be the same for the microvalves with spiral top electrode and full top electrode. This means that 150 nm thick Ti/Au bimetallic layer does not significantly alter the stiffness of the diaphragm. Moreover, to assure the resilience of the diaphragm over long operation cycles, 410  $\mu\text{m}$  radius microvalves are actuated repeatedly in low frequency. It is observed that pull-in voltage does not change over 100 cycles at 0.25 Hz frequency.

**Table 3.2: Pull-in and pull-out voltages measured for different diaphragms.**

Diaphragm radius ( $\mu\text{m}$ )	Type of the top electrode	Pull-in voltage (V)	Pull-out voltage (V)
410	Spiral	47	29
410	Full	46	31
300	Spiral	65	40
300	Full	66	40

After pull-in characterization of the microvalves, flow tests are carried out to determine the leakage properties. Leakage tests are carried out with DI water. For this purpose, the setup used flow in characterization of normally open microvalves (Figure 2.26) is modified. A fluid reservoir is placed just before the inlet of the prototype to supply pressurized DI water. Figure 3.23 illustrates the modified test setup. To direct the pressurized liquid in the microchannel, fluidic ports are mounted at the inlet of the prototypes (Figure 3.24).

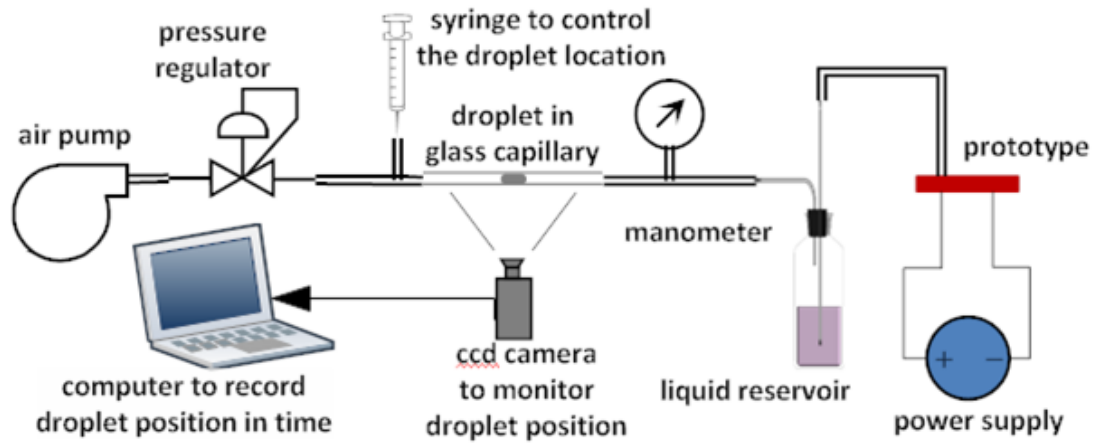


**Figure 3.23: Illustration of the test setup used for leakage characterization of normally closed microvalves.**

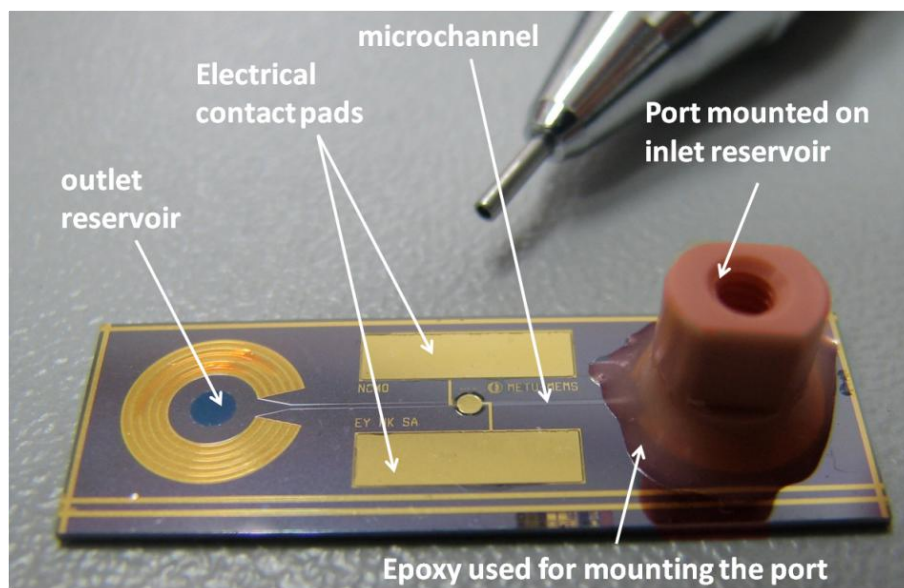


**Figure 3.24: Prototype with the port mounted at the inlet, ready for leakage tests.**

During the leakage tests, 20 kPa capacity microvalves are operated applying 200 V dc under different inlet pressure values. Flow rates are measured both in closed and open states using droplet monitoring system explained in section 2.4. The ratio between the flow rates in open and closed states is recorded as the leakage ratio.



During the tests, no leakage is observed up to 20 kPa inlet pressure. The leakage increases to 9 % at 40 kPa pressure, which is beyond the low pressure range (Figure 3.25). Maximum open flow rate is measured as 9.4  $\mu\text{l}/\text{min}$  during the tests.

The reason for the deviation of the experimental results from theory is relatively low actuation potential. According to the theory, actuation potential that should be applied is 232 V. However, 200 V is applied to actuate the microvalves. This reduces the flow rate in open state, which in turn increases the leakage ratio compared to the theory. Another reason for this error is the approximation made in calculation of the leakage ratio. As stated above, leakage ratio is approximated as the ratio between the projected areas underneath the semi-circular wall in closed state to that in open state. Here, the flow resistance created by the semi-circular wall is ignored. This also introduces an error between the experimental and theoretical results.

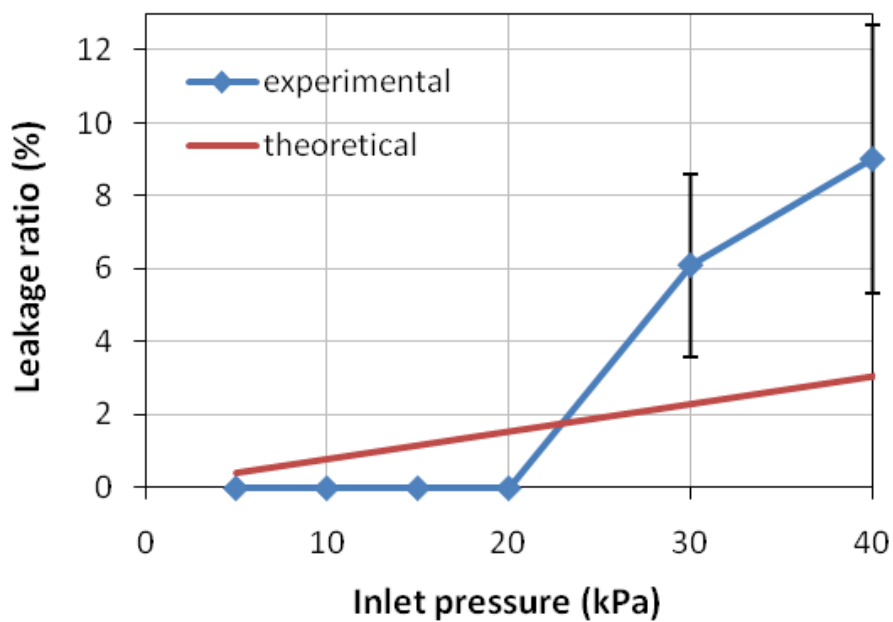


**Figure 3.25: Leakage ratio measured at different inlet pressure levels for 20 kPa capacity microvalves.**

After determining the leakage properties, dynamic response of the microvalves are investigated. For this purpose, test setup is revised to measure instantaneous flow rate. The setup includes a low pressure (max. 345 mbar) regulator with 0.1 % precision, and a flow sensor capable of reading data at 10 Hz and detecting flow rates as low as 2 nl/min. Figure 3.26 shows the revised setup. During the tests, it is observed that the microvalve responds the actuation potential in 0.3 sec. on average. Figure 3.27 shows the change in the flow rate for the microvalve with 410  $\mu\text{m}$  radius diaphragm and a straight wall, under 2 kPa inlet pressure. Marching flow front clearly shows the operation of the microvalve. As stated above in section 3.2, decreasing the effect of the compliance during design stage, response time of the microvalve can be increased to obtain latching microvalves.

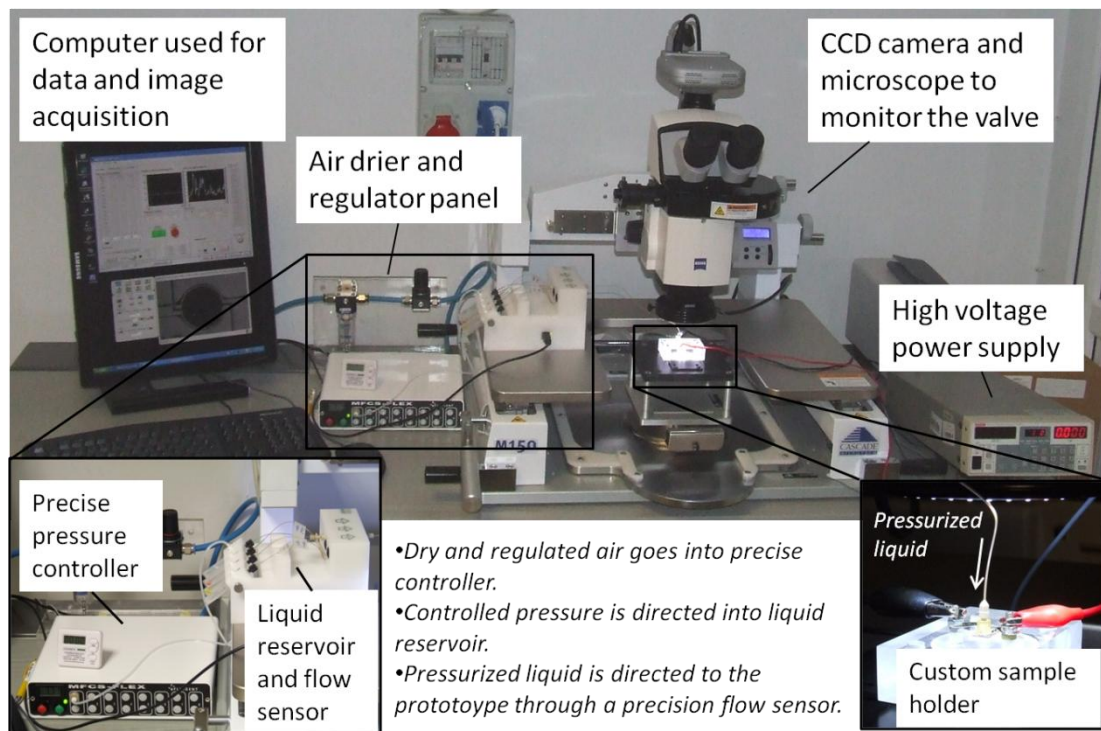


**Figure 3.26: Revised setup used for investigation of dynamic response of the microvalve.**

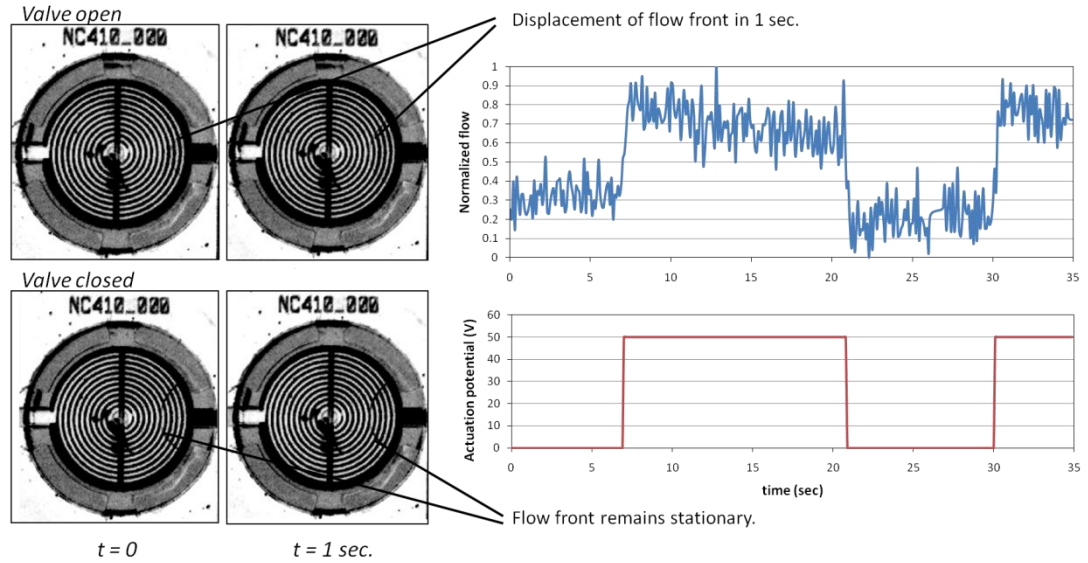


**Figure 3.27: Response of the microvalve to actuation potential. Inlet pressure is 2 kPa, open flow rate is 100 nl/min.**

To investigate the effectiveness of the semi-circular walls in reducing the leakage, microvalves with different radius semi-circular walls are tested in closed state. For these microvalves, leakage rate is recorded while varying the inlet pressure. Figure 3.28 shows the leakage rate measured for different semi-circular wall radii at varying pressure levels. Results prove that increasing the radius of the semi-circular wall reduces the leakage rate.

### 3.5 Conclusion

Design, analysis, fabrication, and characterization of a normally closed electrostatic microvalve are explained in this chapter. The microvalve utilizes a valve seat in the form of a semi-circular wall to figure out the leakage problem in the normally open electrostatic microvalve explained in the previous chapter. Besides, the microvalve isolates the working fluid from the electric field. As a result, actuation potential becomes independent of the working fluid, solving a major problem in electrostatic microvalves for LOC applications.

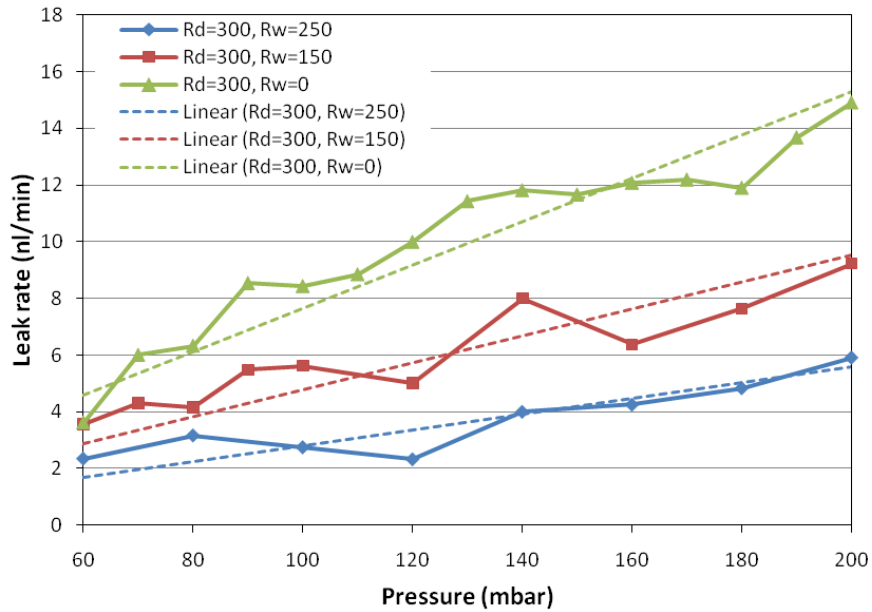


**Figure 3.28: Leakage rate measured for different semi-circular wall radii. Diaphragm radius is 300  $\mu\text{m}$ .**

For the design of the microvalves, actuation potential, leakage ratio, and compliance of the valve diaphragm are considered. All of these parameters are minimized to determine the dimensions of the microvalve. For minimization of the parameters, an aggregate objective function (AOF) is used, which is a linear combination of individual parameters. The AOF introduces flexibility to design by relatively weighting each parameter. Hence, it becomes possible to design microvalves specific for application.

Designed microvalves are then fabricated by combination of bulk and surface micromachining techniques using 5 masks. Fabricated microvalves are tested for pull-in and leakage characterization. Pull-in tests show that the microvalve diaphragms can be pulled-down by applying 46 – 66 V dc potential for any working fluid. However, depending on the radius of the semi-circular wall, actuation potential can increase up to 230 V to maximize the gap underneath the semi-circular wall, hence the open flow rate.

During leakage tests, microvalves optimized for 20 kPa inlet pressure are tested with pressurized DI water. Leakage ratio is measured using droplet monitoring method explained in section 2.4. No detectable leakage is observed using this method up to 20 kPa inlet pressure. Leakage ratio becomes 6 % at 40 kPa, which is higher than the intended pressure level. To detect low leakage rates and to investigate the effectiveness of semi-circular wall design, a precision flow sensor is used. Results obtained for different semi-circular wall radii show that the leakage rate decreases with increasing wall radius. This proves the effectiveness of the valve seat design.

Considering the characteristics of the microvalve, possible applications are discussed in the following chapter.

## **CHAPTER 4**

### **POTENTIAL APPLICATIONS OF THE MICROVALVES IN LAB-ON-A-CHIP**

As stated at the beginning of chapter 1, microvalves are employed in applications ranging from polymerase chain reaction (PCR) to enzyme assays, or protein synthesis in lab-on-a-chip systems. These applications can be carried out using various microfluidic schemes, where flow of a single phase or multiple phases can be driven by capillary action or by applying pressure. An interesting scheme in LOCs is droplet-based microfluidics. Droplet microfluidics is based on formation and manipulation of nanoliter or sub-nanoliter size isolated droplets in a microchannel. These droplets can be used as micro-reactors to carry out specific analyses or assays. Since the size of the droplets is in the same scale with the biological material (protein, cell, etc.), controllability of the analyses or assays can be significantly improved. In addition, high surface to volume ratio of micro-droplets increases the reaction rate [106], which improves the throughput of droplet based systems. Considering these advantages, droplet based microfluidics stand out as a promising scheme for LOC applications.

This chapter gives brief information on droplet based microfluidics. Possible LOC applications using droplet based microfluidics are presented. Use of microvalves in droplet based microfluidic systems is also discussed. As a conclusion, a multi-drug effect analysis device utilizing normally closed microvalves is presented. The system is demonstrated for proof-of-concept. Additionally a microvalve controlled droplet metering technique is proposed as an extension to multi-drug effect analysis system. Initial test results are also presented.

#### 4.1 Droplet Based Microfluidics and LOC Applications

Droplet based systems often involve two immiscible fluids (e.g. air-water, water-oil, etc.). Affected by the inertial, viscous, and interfacial forces, one of these phases often encapsulate the other phase causing droplets in the microchannel. Relative effects of these forces are generally defined in terms of non-dimensional Reynolds ( $Re$ ) and Capillary ( $Ca$ ) numbers [107]. Reynolds number is defined as the ratio of the inertial forces to viscous forces (4.1).

$$Re = \frac{\rho v d}{\eta} \quad (4.1)$$

Here,  $\rho$  is the density,  $v$  is the flow velocity,  $d$  is the characteristic dimension, and  $\eta$  is the dynamic viscosity. For microchannels,  $Re$  is changing between 1 and  $10^{-3}$  [107]. Considering that turbulent transition occurs at  $Re = 10^3$  [108], it can be concluded that the flow in microchannels is always in laminar regime.

Second non-dimensional number affecting the droplet formation is the Capillary number, which is defined as the ratio of the viscous forces to interfacial forces (4.2).

$$Ca = \frac{\eta v}{\sigma} \quad (4.2)$$

where  $\sigma$  is the interfacial tension.

Generally, T, Y, or cross junction configurations are used to generate droplets in microchannels. In these configurations, the carrier fluid shears the other phase, creating disperse droplets of the latter phase (Figure 4.1). Geometry of the droplets generated using T, Y, or cross junctions vary depending on the viscous, inertial, and interfacial forces as stated before. Zheng et al. studied the droplet formation with respect to Capillary number and relative speeds of the phases [109]. Figure 3.2 shows various droplet flow regimes in a cross-junction.

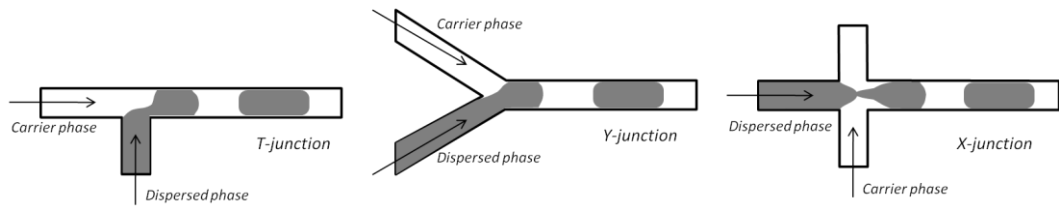


Figure 4.1: T, Y, and cross junction configurations to generate droplets.

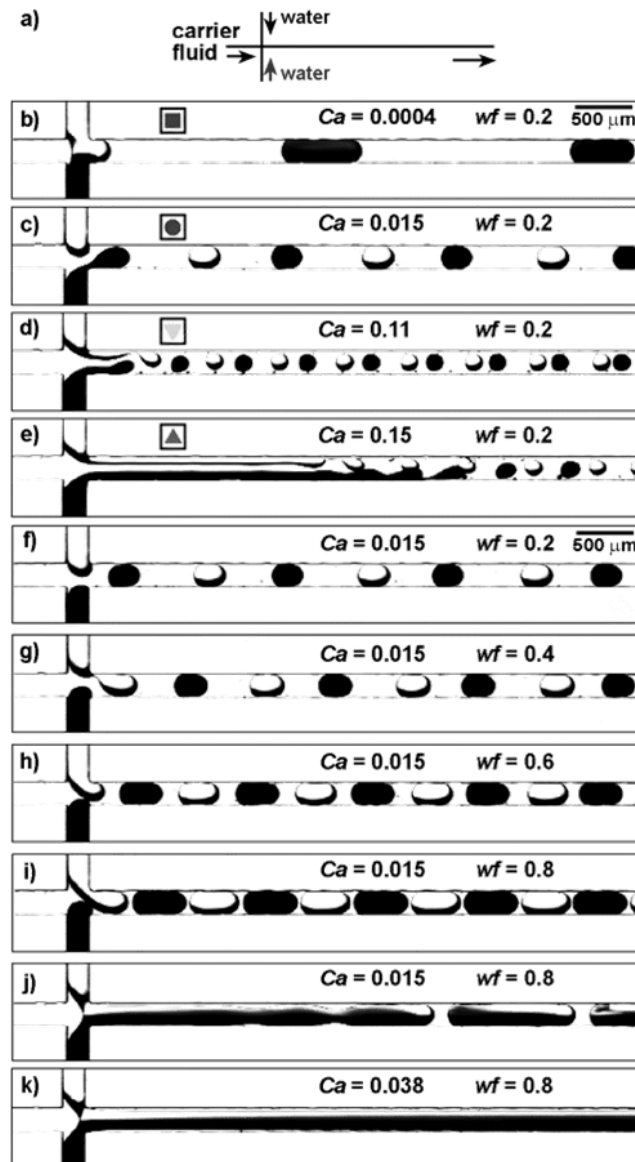
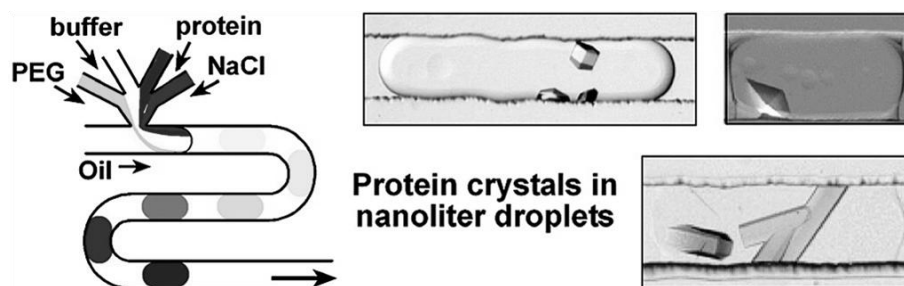


Figure 4.2: Effect of  $Ca$  and flow speed on droplet formation.  $w_f$  denotes water fraction (ratio of flow speed of water to total flow speed) [109].



Theory explained above shows that the volume and shape of the droplets could be controlled by altering the hydrophobicity of the channel surfaces or by changing relative flow rates of the phases. Regarding this conclusion, many LOC applications have been developed based on droplet microfluidics. One distinct application is proposed by Zheng et al [110]. In this application, they screened protein crystallization in droplets, which contain a solution of protein and precipitant at controlled concentrations (Figure 4.3).



**Figure 4.3: Screening of protein crystallization [110]. Varying flow rate of NaCl changes the concentration inside the droplet.**

Another application is proposed by Gong et al [5], where effect of drugs on breast cancer cells is screened. For this purpose, cells are encapsulated in a droplet of drug solution (Figure 4.4).

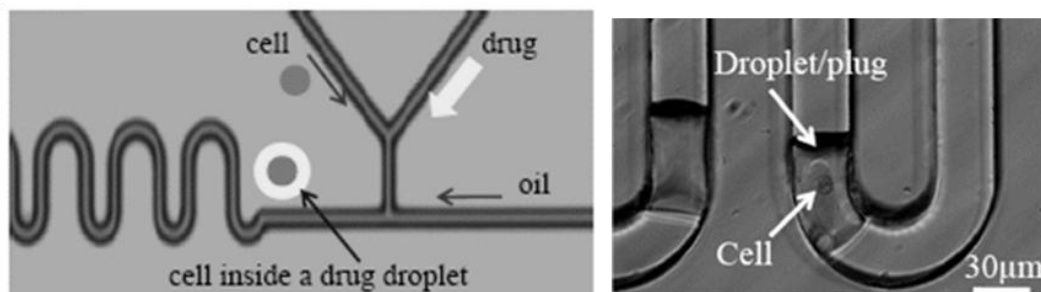


**Figure 4.4: Drug effect screening system proposed by Gong et al. [5].**

Main advantage of the above applications is significantly reduced reagent consumption. Traditionally, such analyses are carried out using robotic systems to handle small amounts of reagents. However, these expensive systems increase the cost of such analysis. Moreover, time required to carry out the analysis is relatively long in traditional methods. On the other hand, droplet based systems reduce the cost of the analysis to a single chip price. In addition, because of the reduced reaction times and high droplet generation rates, (Edd et al. reported generation rate of  $14.9 \times 10^3$  droplet/min [111]) throughput is significantly improved by droplet based systems.

In addition to these applications, microdroplets are also used to screen enzyme activity [112, 113], or polymerase chain reaction [114, 115]. These applications take the advantage of well defined control volumes, which minimize the interaction of the molecules with the boundaries.

Consequently, advantages of droplet microfluidics can be listed as:

- Increased reaction rates due to high surface area to volume ratio
- High generation rates, hence improved throughput
- Well controlled sub-nanoliter volumes
- Reduced reagent consumption

Consequently, it can be stated that droplet microfluidics is a promising scheme to carry out analyses related to chemistry and life sciences.

#### **4.2 Electrostatic Microvalve Controlled Multi-Drug Effect Analysis System**

Among the applications mentioned in section 4.1, drug effect analysis systems are especially important. Conventional drug screening techniques utilize microwell plate approach, where reagents and target molecules/cells are loaded in wells with volume in the order of 1  $\mu$ l using robotic equipment (Figure 4.5). After loading the reagents and the targets, the wells are observed following an incubation period. High cost of the equipment prevents widespread application of the method. Additionally, speed of the robotic equipment limits the throughput. Moreover, the method consumes

high volumes of reagents. Relatively high volume of the wells also introduces a scaling problem. Number of molecules that can be loaded in a 1  $\mu\text{l}$  microwell is in the order of  $10^9$ , while only one molecule can be entrapped in a 1 fl droplet [119]. Therefore, intermolecular interactions cannot be prevented in microwell plate approach. High volumes of the wells also increase the diffusion time (diffusion time is  $10^1$  min. order in microwell, while 1 ms order in a droplet [119]), which increases the reaction time in turn. This reduces the throughput rate of microwell plate approach compared to droplet based approach. Considering these facts, it is obvious that droplet microfluidics is a promising tool for drug discovery.

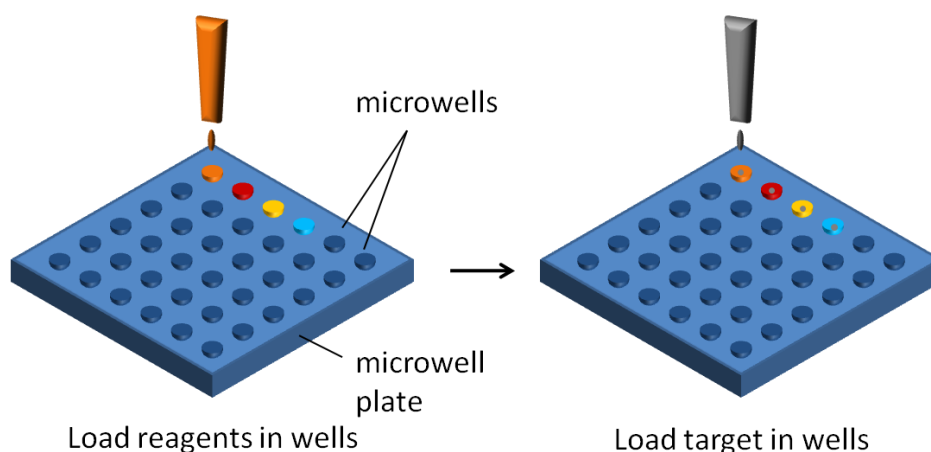


**Figure 4.5: Microwell plate approach.**

Need for fast and effective drug effect analysis devices are especially essential for cancer treatment. Cancer treatment often requires a patient-specific approach [120]. Practically, combination of drugs are tried to find the most effective chemotherapeutical treatment for the patient. However, finding the most effective combination treatment may sometimes be fatal. Therefore, development of a fast, simple to use drug effect analysis system, which enables screening of multiple drugs, is vital.

Gong et al. [5] proposed a droplet based system to screen effect of Cytochalasin D drug on MDA-MB-231 breast cancer cell (Figure 4.4). In this system, single breast cancer cells are entrapped in the drug solution with fluorescent indicator. Afterwards, viability of the cells is observed by taking fluorescence image of the cells in time. Although the system improves the throughput, it does not allow screening the effect of multiple drugs on the same chip. Wang et al. proposed a system to screen combination chemotherapeutic effect on HCT116 colorectal cancer cells [121]. The system mimics microwell plate approach instead of utilizing a droplet based technique. In the design, 64 chambers of 700  $\mu\text{m}$  x 700  $\mu\text{m}$  dimensions are filled with cell culture in drug solution of lapatinib and kinase inhibitor LY 294002 at varying concentrations. Growth of the cell culture is monitored to analyze the combination effect of the drugs. Although the system enables analysis of multiple drugs, it does not consider intercellular interactions. Common property of these systems is that they are fabricated using PDMS. However, PDMS suffers vapor permeability as mentioned in chapter 1. This may cause evaporation of the solution during incubation, which was not considered in the cited studies.

In this study a drug effect analysis device, which is capable of controlling of multiple devices on the same chip, is proposed. The system utilizes two normally closed microvalves to switch between different drugs. Selected drug meets with the cell stream at a Y-junction. Flow of the drug-cell mixture is broken by the oil flow at T-junction to generate droplets with single cells entrapped inside. Generated droplets are stored at the serpentine channel, where drug activity is monitored. Besides the operational advantages of the microvalve, structural material – parylene-C – improves the vapor permeability problem in PDMS based systems. Figure 4.6 illustrates the operation of the system.

Prototypes of the system are fabricated using the mask set, whose layout is shown in Figure A.6. For the fabrication of the prototypes, process flow explained in section 3.3.1 is used. Figure 4.7 shows fabricated prototype.

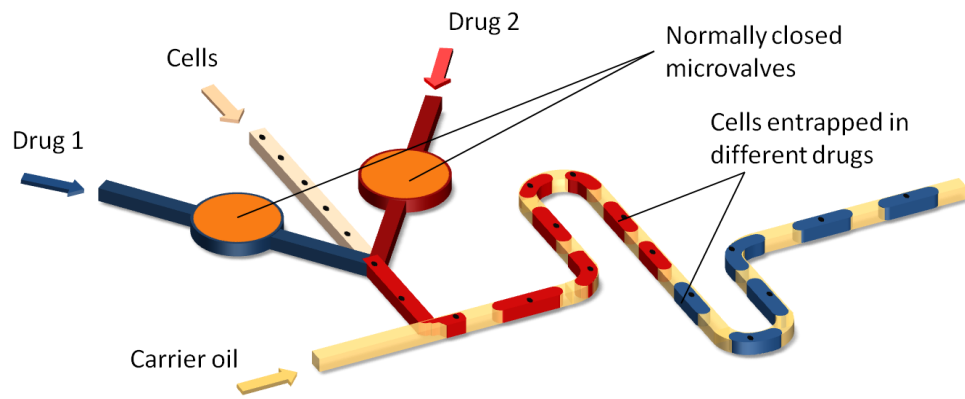


**Figure 4.6: Illustration of the drug effect analysis system**

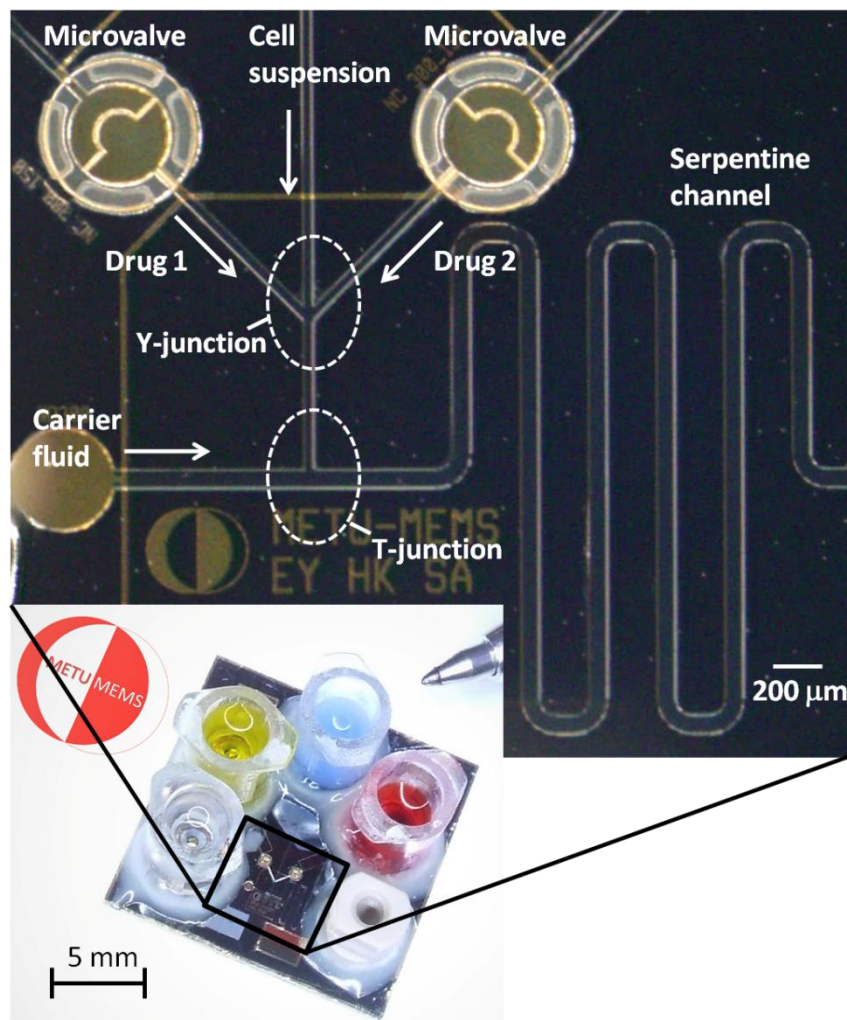


**Figure 4.7: Fabricated prototype of the drug effect analysis system.**

Fabricated devices are tested with colored DI water, micro-bead suspension, and silicone oil. DI water is colored using two different food dyes. These act as two different drugs during testing. For the micro-bead suspension, polystyrene beads of 3  $\mu\text{m}$  diameter are used. Micro-bead suspension acts as the cell solution during the tests. The suspension is prepared using DI-water, polystyrene bead mixture with concentration of  $1.68 \times 10^7$  particles/ml, regarding the vendor specifications [122]. With this concentration, assuming that the beads are homogeneously distributed in the suspension and that the flow rate of the colored water is the same with the bead suspension; single bead would be entrapped in a 120 pl droplet. During the tests, silicone oil from Dow Corning Corp. [123] is used as the carrier phase generating the droplets. For testing of the devices, negative 25 kPa pressure is applied at the outlet. To supply test liquids, reservoirs are mounted at the inlets and 0.5 ml liquid is dispensed in these reservoirs. For electrical connection, an external 2-way switch is used to apply voltage to selected microvalve. During the tests, droplet formation and encapsulation of beads in droplets are observed. Figure 4.8 illustrates the test set-up. Figure 4.9 shows the system in operation.

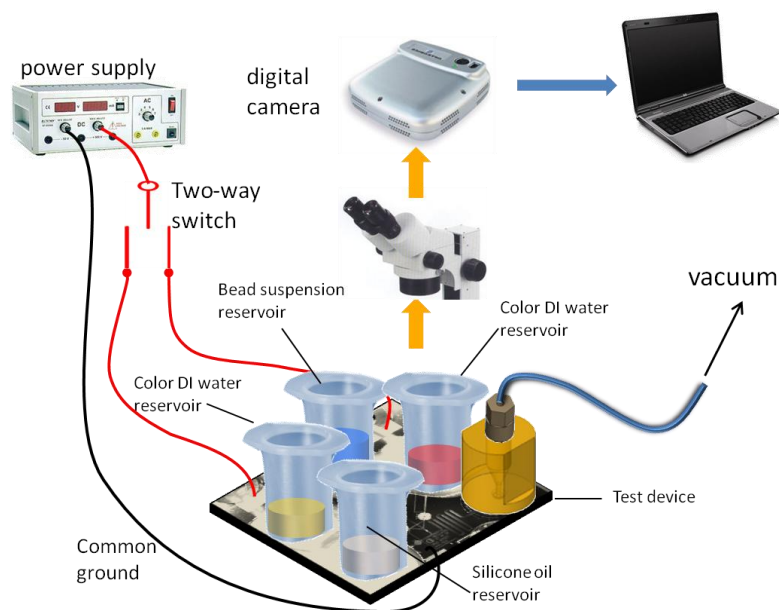


**Figure 4.8: Setup used for testing of drug effect analysis device.**

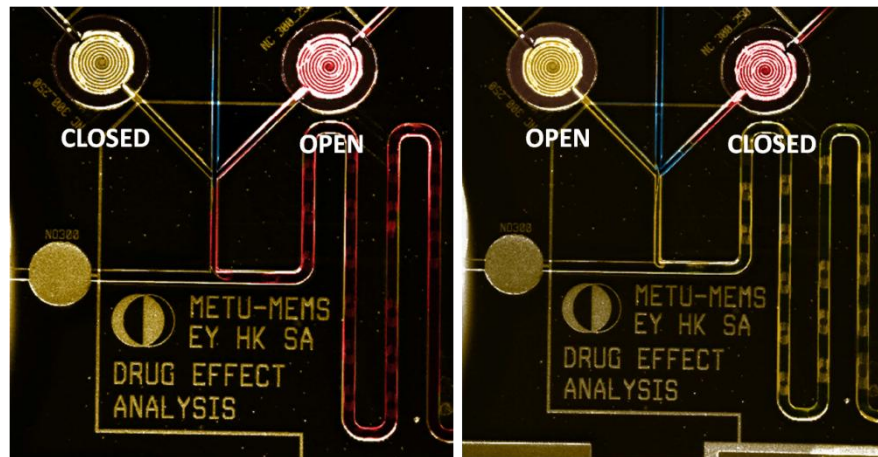


**Figure 4.9: Open and closed states of the microvalves. Figures are colorized for clarity.**

During the tests, it could be possible to obtain monodisperse droplets of 137  $\mu\text{l}$  droplets with 0.34  $\mu\text{l}$  deviation. To measure the volume of the droplets, area of each droplet is measured using ImageJ. Area found is multiplied by the channel height. Figure 4.10 shows the train of droplet in the serpentine channel and a single micro-bead entrapped in a droplet.

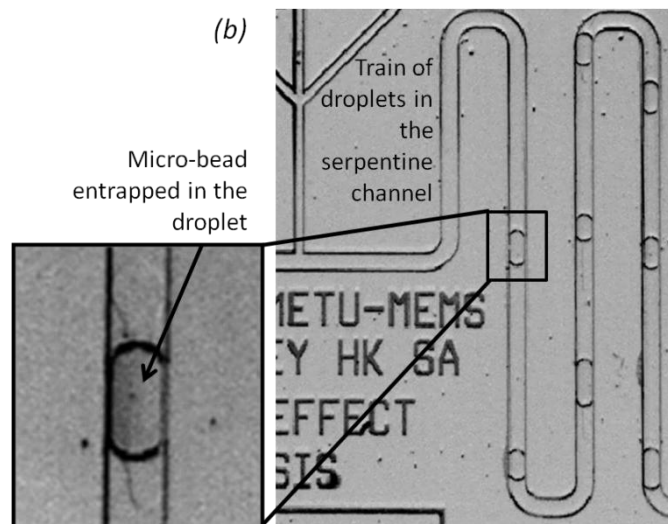


**Figure 4.10: Monodisperse droplets in the microchannel and single micro-bead entrapped in the droplet.**

The system is also tested with living yeast cells. During the tests, yeast cells could also be entrapped in the droplets. However, it is observed that more than a single cell is entrapped in some of the droplets, which is a result of cell aggregation. Figure 4.11 shows the yeast cells entrapped in a droplet.

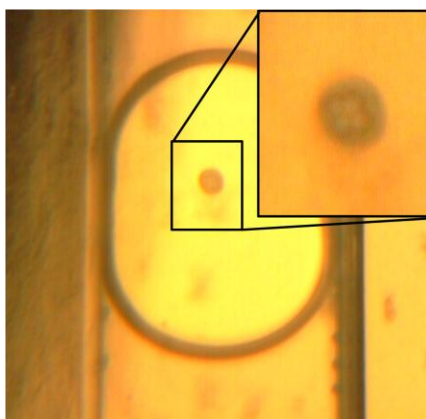


**Figure 4.11: Yeast cells entrapped in the droplet and close up view of the cells.**

Consequently, initial tests prove that the system can be used for screening effect of multiple drugs on a single type of cell. Additionally, it should be noted that number of drugs to be screened could be increased by simply increasing the number of inlet channels and the microvalves, which does not add any significant operational complexity.

The system can be improved further to facilitate mixing of the cell suspension and the drug. This can be achieved by chaotic advection after generation of the droplets [124]. Moreover, the Y-junction can be modified as a flow focusing nozzle to minimize the boundary between the phases to be mixed (Figure 4.12).

Additionally, the system can be modified by utilizing normally open electrostatic microvalve. Normally open electrostatic microvalve can be used to control the flow rate of the carrier oil, hence to tune the size of the droplets. As a result, the system



can be used for different size cells or molecules. This electrostatic microvalve controlled droplet metering technique is explained in the next section.

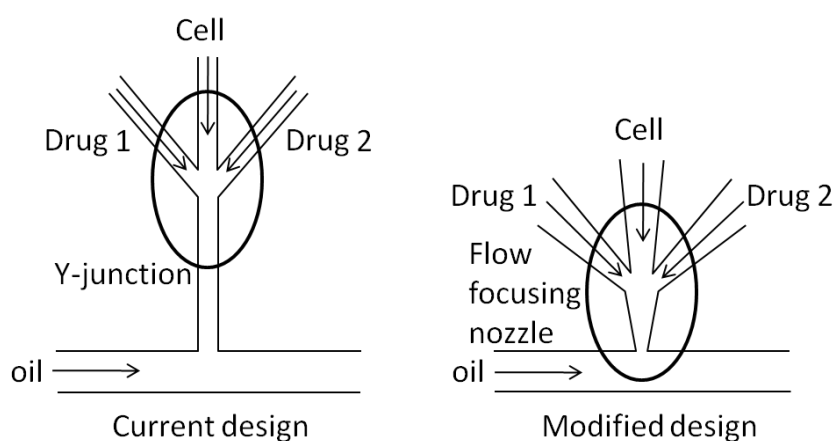


**Figure 4.12: Modification proposed for the Y-junction.**

### 4.3 Electrostatic Microvalve Controlled Droplet Metering System

There are different methods for controlling droplet sizes. However, precise metering methods utilize complicated micro-channels [116] or combination of microfluidic components such as micro-choppers and micro-switches [117]. Zeng et al. [118] proposed a simplified solution, where pneumatic microvalves are utilized to control the flow of the dispersed phase. Here, flow of the dispersed phase is switched on using the pneumatic microvalves for a controlled period. The period, where the valve is kept open, defines the volume of the droplets. Although, it could be possible to control the droplet size precisely, the application requires an off-chip vacuum pump and a precise timer for implementation.

In any case, droplet size depends on the flow rate of the phases, which is commonly controlled using syringe pumps [107]. However, relatively long stabilization time of syringe pumps prevents instantaneous control of the droplets. On-chip flow rate control is proposed as the solution of this stability problem. In chapter 2 it was

proven that the flow rate could be precisely controlled using normally open microvalves. Therefore, it can be concluded that normally open microvalves can be utilized for precise droplet metering.

Based on the aforementioned conclusions, a droplet metering system, which utilizes normally open electrostatic microvalves, is proposed. The system is implemented with a Y-junction to generate the droplets (Figure 4.13). The branches entering the junction carry the disperse phase and the carrier phase. The microvalve is located on the branch where the carrier phase flows. Flow rate of the carrier phase is controlled by changing the actuation potential as explained in chapter 2.

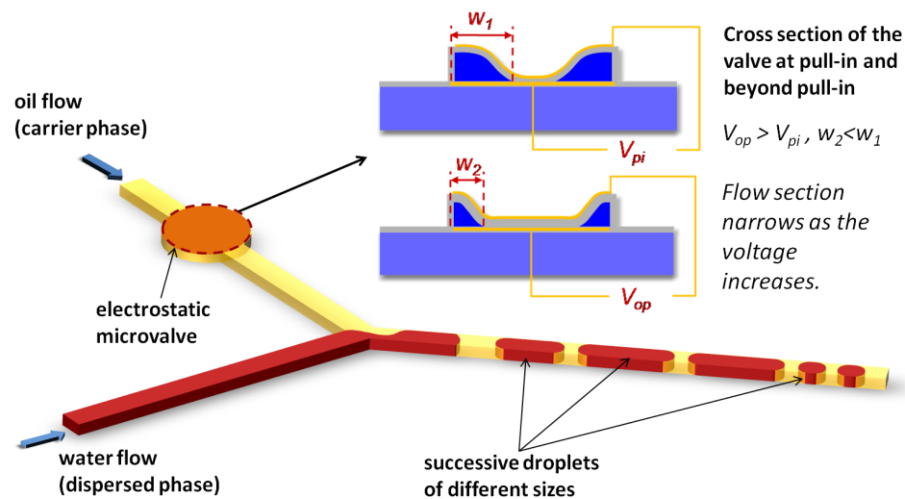


**Figure 4.13: Proposed droplet metering system using normally open electrostatic microvalve.**

The prototype of the system is fabricated using the mask set, whose layout is shown in Figure A.6. Fabrication flow explained in section 2.3 is used to manufacture the prototypes. Figure 4.14 shows the fabricated prototypes.

Fabricated prototypes are then tested with water and oil to determine the change of average droplet volume with the actuation potential. During the tests, pressurized air

(at 10 kPa) is directed to oil and water reservoirs, which are connected to inlet ports mounted on the test device. Droplet formation at Y-junction is monitored using a CCD camera mounted on a microscope. Snapshots of the droplets are analyzed to determine the droplet volumes. Figure 4.15 shows the schematic of the test setup.

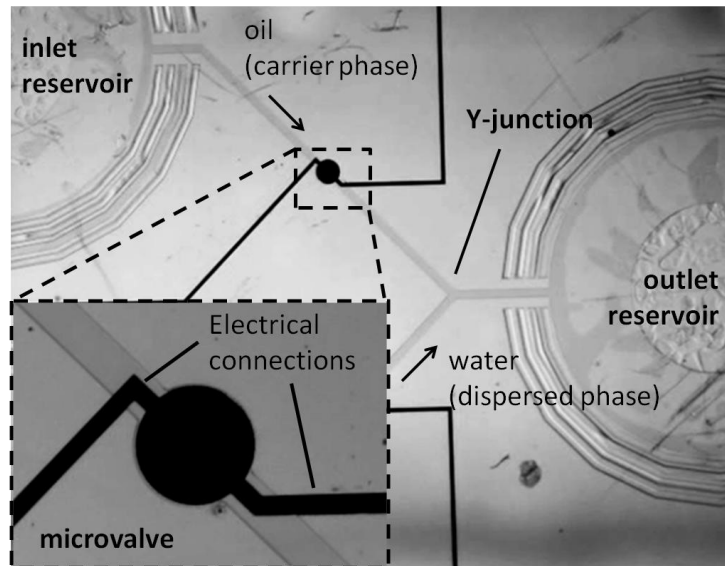


**Figure 4.14: Fabricated droplet metering system prototype.**

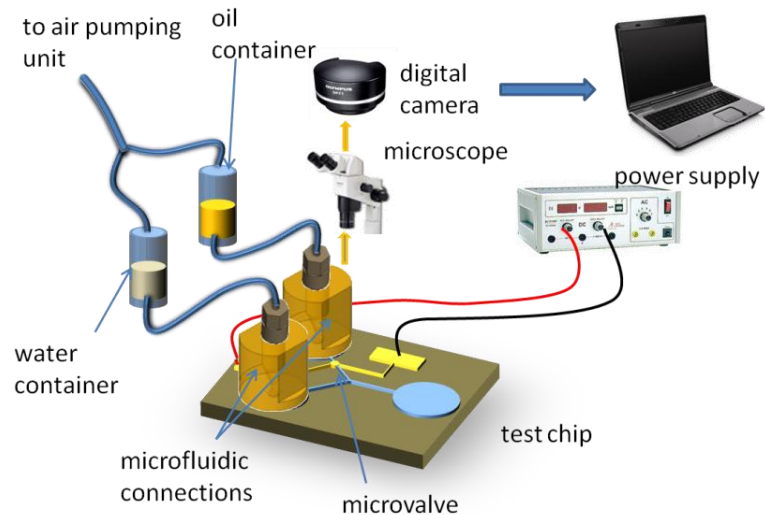


**Figure 4.15: Illustration of the test setup for droplet metering system.**

In the tests, droplets are observed at different actuation potential levels (Figure 4.16). Since the oil flow rate is significantly lower than the flow rate of the water (due to difference in viscosities), water droplets elongate during formation, resulting in plug type droplets. Snapshots of these plugs are analyzed using image processing tool; ImageJ.

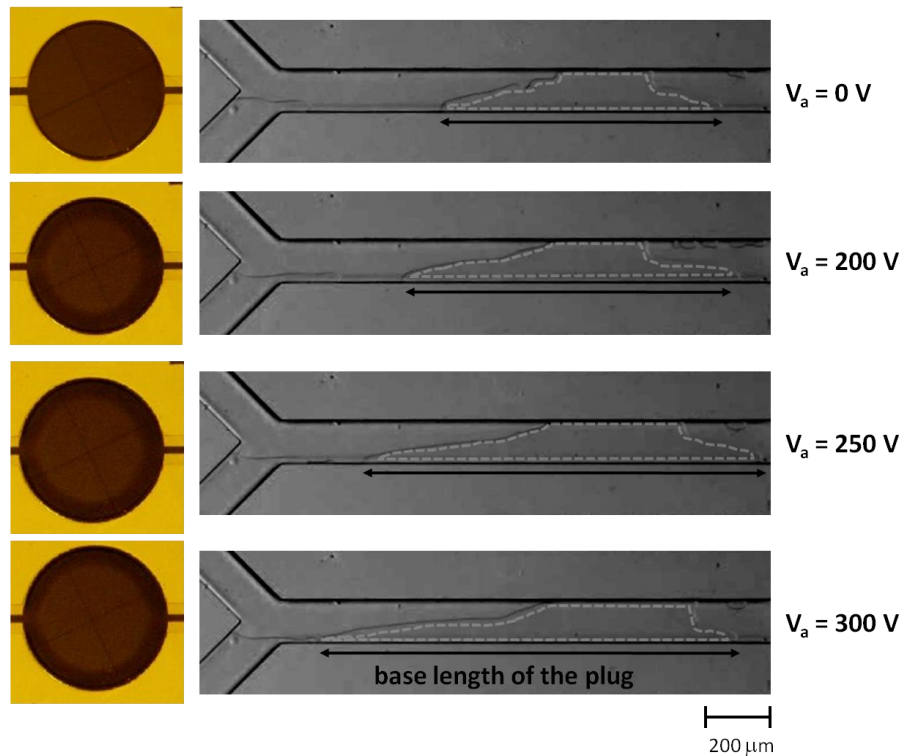


**Figure 4.16: Top views of the microvalve and generated plugs at different actuation potentials.**

Consequently, average droplet volume is found for each actuation potential level. Figure 4.17 plots the droplet volume measured at different actuation potential levels. Test results shows that, monodisperse droplets could be generated that at specified actuation potential with a deviation of 6 % in volume. Investigating Figure 4.17 shows that plug size increases significantly after pull-in. As prescribed by the theory presented in chapter 2, flow rate of the carrier phase decreases almost linearly, which

results in a linear increase in droplet volume. The slope of this line gives the voltage sensitivity of the technique, which is computed as 0.4 p/V. This result proves the precision of the proposed technique to control the droplet size.

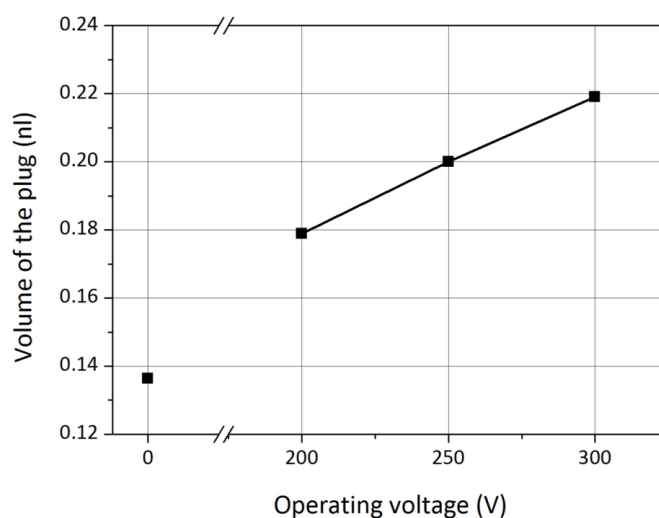


**Figure 4.17: Droplet volume versus the actuation potential.**

Although the system is implemented with Y-junction, T-junction or cross junction can also be used with this technique. To compare the droplet size in each case, junctions are modeled using COMSOL Multiphysics with the same dimensions (each branch and the main channel are 100  $\mu\text{m}$  wide, 4  $\mu\text{m}$  high). Multi-phase flow is simulated for each case at the same boundary conditions (inlet pressure 10 kPa, outlet pressure 0 kPa) with the same working fluids (water and oil). It is seen that, smaller droplets can be obtained if T or cross junctions are used (Figure 4.18). Therefore, in case smaller droplets are required in a specific application, the system should be modified to implement T or cross junctions.

As a result, it is shown that library of multiple size droplets can be obtained using the technique proposed. If the technique is implemented in multi-drug screening system presented in the previous section, different micro-reactors with varying sizes can be

obtained. This makes the technique an interesting tool to carry out multiple analyses on a single chip.

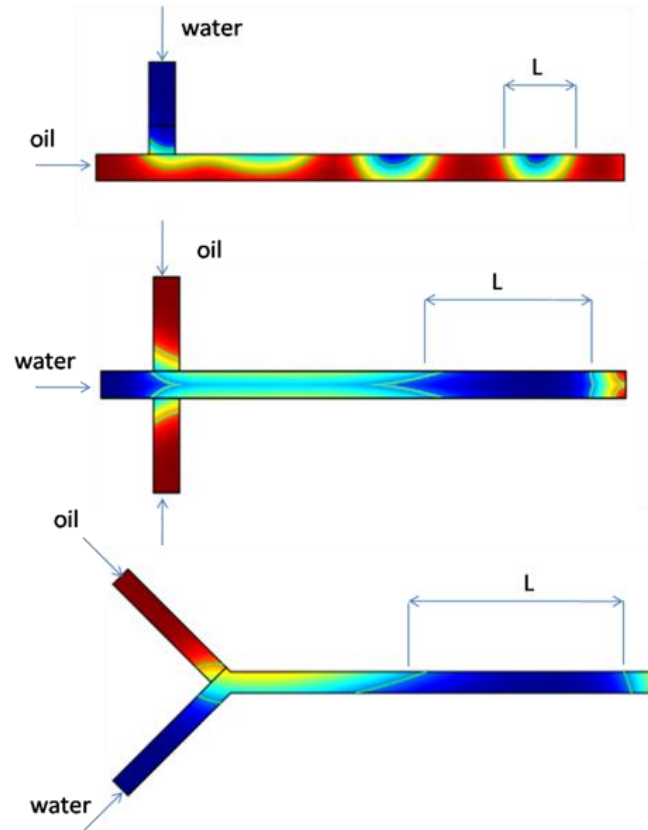


**Figure 4.18: Droplet formation simulated using T, Y, and cross junctions.**

Although the technique is demonstrated successfully, it could not be possible to implement it in the multi-drug effect analysis system presented in the previous section because of fabrication challenges. As explained in section 2.3.1, metallization of an electrode on top of a parylene layer requires a special baking procedure. During fabrication of the multi-drug effect analysis devices, this baking procedure is utilized first for metallization of the top electrodes of the normally closed microvalves. In order to create the top electrodes of the normally open microvalves, this procedure should be repeated once more. However, this results in

over-baking of the sacrificial photoresist in the actuation chamber, which was already baked. Consequently, it may not be possible to remove the sacrificial photoresist in the actuation chamber.

#### **4.4 Conclusion**

In this chapter, possible applications utilizing the microvalves are discussed. In the applications, droplet based systems are emphasized because of the advantages introduced by compartmentalization concept. Well defined sub-nanoliter volume compartments generated in a microchannel increase the reaction rates significantly in chemical analysis. Moreover, since the size of the compartments is comparable with the size of the cells or molecules, droplet microfluidics becomes preferable in life sciences.

Considering the advantages of droplet microfluidics, a normally closed electrostatic microvalve controlled multi-drug screening system is proposed. The prototype of the system is fabricated and tested. Operation of the system is demonstrated with polystyrene microbeads and living yeast cells. As an extension of the system, a normally open electrostatic microvalve controlled droplet metering system is proposed. Initial tests prove that droplet size can be controlled precisely with the proposed technique. Possible improvements of the proposed systems are also discussed in this chapter.

## CHAPTER 5

### CONCLUDING REMARKS AND FUTURE WORK

In this thesis work, analysis, design, and implementation of two different MEMS microvalves are carried out. Proposed microvalves are intended for use in lab-on-a-chip applications, which require in-plane operation in low pressure range. Considering these requirements, brief descriptions and properties of these microvalves are provided below.

1. The first microvalve design is the normally open electrostatic microvalve. The valve is composed of an in-plane diaphragm fabricated monolithically with the microchannel using parylene-C. The microvalve operates by applying voltage across two electrodes located at the bottom of the channel and at the top of the diaphragm. Pull-in of the diaphragm obstructs the flow. The microvalve can be operated at moderate voltage levels as low as 14 V with dielectric fluids. Minimum operating voltage is obtained for fluids with dielectric constant around 3-5. Although there is an inherent leakage, it can be possible to precisely control flow rate with voltage sensitivity of  $4 \times 10^{-3}$   $\mu\text{l}/\text{min}/\text{V}$ . On the other hand, it cannot be possible to operate the valve by applying dc potential with electrolytic liquids, such as water. Besides, the leakage ratio is 14 % at 10 kPa inlet pressure.

Similar microvalve design proposed before only considers problem of electrostatic actuation in liquid media [64]. It is the first time here a detailed analysis and characterization of normally open microvalve is carried out.

2. The second microvalve is the normally closed electrostatic microvalve. This microvalve is proposed for the first time in the literature. The design aims mainly to solve the leakage and actuation potential problem in the normally



open microvalve design. The valve uses an in-plane parylene diaphragm, as it was in normally open microvalve. However, in this case the diaphragm is located at the bottom of the microchannel. The diaphragm separates the channel with an actuation chamber buried in the substrate. The valve operates by applying potential across two electrodes located at the bottom of the actuation chamber and at the top of the diaphragm. As a result, the diaphragm is pulled-down on the bottom of the actuation chamber, allowing fluid flow underneath the valve seat suspending from top of the microchannel. In this design, a unique and reconfigurable valve seat is proposed to minimize the leakage. It is shown that the microvalves can be operated by applying voltages as low as 46 V for any working fluid. No detectable leakage is observed up to 20 kPa inlet pressure.

Main properties of proposed microvalves are tabulated in Table 5.1.

**Table 5.1: Main properties of the microvalves proposed in the thesis.**

	<b>Inlet pressure</b>	<b>Leakage</b>	<b>Actuation potential</b>	<b>Working fluid</b>
Normally open electrostatic microvalve	10 kPa	14 %	14-71 V dc	air, oil
Normally closed electrostatic microvalve	20 kPa	0	47-66 V dc	Any fluid (including electrolytic liquids)

Considering the properties of these microvalves, two systems utilizing the normally open microvalve and normally closed microvalve are proposed. Both of the systems rely on droplet based microfluidics. Prototypes of the systems are fabricated and initial tests are carried out. Short descriptions of the systems are provided below.

1. The first system proposed is the droplet metering system utilizing normally open microvalve. The system involves a Y-junction, where water-in-oil droplets are generated. Normally open microvalve is used to control the flow rate of the oil, hence the volume of the droplets. Initial tests show that it can be possible to generate droplets with 0.4 pL/V sensitivity.

Similar systems proposed so far make use of pneumatic microvalves and rely on precise timing [118], which complicates integration in a large scale LOC. The system proposed here provides on-chip control of droplet volume.

2. The second system is the drug effect analysis system utilizing normally closed microvalves. Combinational drug therapy is especially important in cancer treatment. The system allows screening of multiple drug effect on a single chip. Normally closed microvalves are used for switching between the drugs. Target cells are entrapped in droplets of selected drug for further analysis. During the test, it is shown that 3  $\mu\text{m}$  diameter micro beads can be entrapped in 137 nL droplets.

Similar designs proposed so far screen effect of only one drug [5]. It is the first time here a droplet based parylene system analyzing effect of multiple drugs is proposed. Moreover, previous screening devices are fabricated using PDMS, which has high vapor permeability. Here, parylene-C improves permeability problem observed in PDMS devices.

As a result, the achievements of this thesis can be summarized as:

1. Two electrostatically actuated microvalves are designed and implemented for parylene based LOC systems. Considering integration ease of electrostatic actuation and surface micromachining compatibility of parylene, the designs are believed to facilitate development of large scale LOC systems.
2. An electrostatically actuated normally open microvalve is designed, implemented, and fully characterized. It is proven that the valve can be used for precise flow regulation in pressure driven parylene based systems.

3. A new normally closed electrostatic microvalve design is introduced. The microvalve solves the problem of actuation voltage dependency on electrical properties of the working fluid, by isolating the fluid from the electric field.
4. A unique and reconfigurable valve seat design in the form of a semi-circle is introduced. The effectiveness of the seat is proven via leakage tests.
5. An electrostatic microvalve controlled precise droplet metering system is proposed. The prototypes are fabricated and tested. Possible improvements of the system are specified.
6. An electrostatic microvalve controlled multi-drug effect analysis system is proposed. The prototypes are fabricated and tested. Capabilities, shortcomings, and possible improvements are proposed.

The objectives in the thesis are previously set as:

1. To design a MEMS based in-plane microvalve with low leakage under low pressure range ( $10^1 - 10^2$  kPa),
2. To manufacture the microvalve using micromachining techniques,
3. To test the operation of the valve, including voltage and flow characterization,
4. To implement the valve on an LOC application for proof-of-concept.

Considering the achievements summarized above, it can be concluded that the objectives of the thesis are satisfied. However, there are still some issues to be improved. These points are presented below as the future work.

1. Actuation potential in both designs can be decreased further by decreasing the thickness of the capacitive parylene layer between the electrodes. This depends on the minimum achievable parylene thickness. Although deposition of 0.5  $\mu\text{m}$  thick parylene on sacrificial photoresist is possible, it could not be possible to create metal layers on top of such thin parylene layer due to

swelling problems. The problem can be solved by optimizing the baking recipe explained in Table B.2. This can be achieved by baking the sacrificial photoresist in vacuum furnace.

2. Baking sacrificial photoresist for extensive periods introduce removal problems. Ordinarily, sacrificial photoresist is removed by immersing the devices in acetone. However, removal of over-baked photoresist requires extensive periods also. To decrease removal time different photoresist removers can be tried, such as dimethylsulphoxide (DMSO) or AZ<sup>®</sup> 100 remover. During fabrication, it is observed that, parylene adhesion promoter A-174 silane (3-methacryloxypropyltrimethoxysilane) causes reflow of SPR 220-3 and 220-7, and AZ 9260 photoresists, which are used as sacrificial photoresists during fabrication. Therefore, treating the wafers in A-174 silane vapor may facilitate removal also.
3. Solving the problem of removing over-baked sacrificial photoresist will improve the drug effect analysis device. Consequently, normally open microvalve can be implemented on the system to control droplet size also.
4. As stated before, droplet metering system can be implemented using T-junction, instead of Y-junction to obtain smaller size droplets.
5. As stated before, a mixer and a flow focusing nozzle can be implemented on drug effect analysis device to enhance rapid mixing of cell suspension with the drug.
6. In normally closed electrostatic microvalve design, it is observed that the microchannel tends to bend down with underlying diaphragm. To solve this problem, the diaphragm should be clamped at its periphery. This can be achieved by embedding the air vents in the substrate, hence eliminating the extension around the diaphragm. As a result, the microchannel would sit on a rigid foundation and would not bend down with the diaphragm.

7. In fabrication of the microvalves, a major problem is the stiction of the diaphragms during release. It is proposed that methanol treatment facilitates the release. However, in practice there are still non-surviving diaphragms. To facilitate yield during release, underlying surface should be roughened. Considering that underlying layer is generally parylene, a short plasma or RIE treatment would reduce stiction problem.
8. In fabrication of the normally closed microvalves, top electrodes are isolated from the working fluid by a thin parylene layer. However, this introduces a new problem; adhesion of semi-circular wall to the diaphragm. This problem is resolved by treating each valve by 5% Micro-90, DI-water solution (MicroSoap) after patterning the sacrificial photoresist. This process can be replaced by depositing and patterning an additional layer on the diaphragm such as gold, on which parylene-C does not adhere well.
9. To improve resilience of normally open microvalves, spiral shaped top electrodes can be utilized, as it is done in normally closed microvalves.
10. In fabrication of the normally open microvalves, gold in top electrode is patterned using Transene gold etchant. Masking photoresist layer needs to be thick to cover the channel topology in this step. However, due to high hydrophobicity, etchant cannot pattern fine features on gold. To solve this problem, top electrode can be patterned using aqua regia solution, which is a mixture of nitric and hydrochloric acids.

Aforementioned future work is believed to improve the characteristics of the designs presented in this study. Additionally, it is believed that this thesis study will help design of electrostatically actuated parylene microfluidic components, such as micropumps or new microvalves. These studies are believed to accelerate the studies to develop large scale LOC system with embedded on-chip electronics.

## REFERENCES

- [1] A. Manz, N. Graber, and H. M. Widmer, "Miniaturized total chemical analysis systems: A novel concept for chemical sensing," *Sensor. Actuat. B-Chem.*, vol. 1, no.1, pp. 244-248, Jan. 1990.
- [2] S. Shoji, M. Esashi, and T. Matsuo, "Prototype miniature blood gas analyser fabricated on a silicon wafer," *Sensor. Actuator.*, vol. 14, no. 2, pp. 101-107, Jun. 1988.
- [3] H. Hufnagel, A. Huebner, C. Gülch, K. Güse, C. Abell, and F. Hollfelder, "An integrated cell culture lab on a chip: modular microdevices for cultivation of mammalian cells and delivery into microfluidic microdroplets," *Lab Chip*, vol. 9, no. 11, p. 1576-1581, Mar. 2009.
- [4] J. C. Tormos, D. Lieber, J.-C. Baret, A. El-Harrak, O. J. Miller, L. Frenz, J. Blouwolff, K. J. Humphry, S. Köster, H. Duan, C. Holtze, D. A. Weitz, A. D. Griffiths, and C. A. Merten, "Droplet-based microfluidic platforms for the encapsulation and screening of Mammalian cells and multicellular organisms," *Chem. Biol.*, vol. 15, no. 5, pp. 427-437, May 2008.
- [5] Z. Gong, H. Zhao, T. Zhang, F. Nie, P. Pathak, K. Cui, Z. Wang, S. Wong, and L. Que, "Drug effects analysis on cells using a high throughput microfluidic chip," *Biomed. Microdevices*, vol. 13, no. 1, pp. 215-219, Oct. 2010.
- [6] Z. Gong, F. Nie, T. Zhang, P. Pathak, Z. Wang, K. Cui, H. Zhao, S. Wong, and L. Que, "High throughput analysis of drug effects on single breast cancer cells using droplet-microfluidic devices," in *23rd Int. Conf. Micro Electro Mechanical Systems*, Hong Kong, China, 2010, pp. 1015–1018.
- [7] H. Andersson and A. van den Berg, "Microfluidic devices for cellomics: a review," *Sensor. Actuat. B-Chem.*, vol. 92, no. 3, pp. 315–325, Jul. 2003.

- [8] A. Grodrian, J. Metze, T. Henkel, K. Martin, M. Roth, and J. M. Kohler, "Segmented flow generation by chip reactors for highly parallelized cell cultivation," *Biosens. Bioelectron.*, vol. 19, no. 11, pp. 1421–1428, Jun. 2004.
- [9] U. Kim, C. W. Shu, K. Y. Dane, P. S. Daugherty, J. Y. J. Wang, and H. T. Soh, "Selection of mammalian cells based on their cell-cycle phase using dielectrophoresis," in *Proc. Nat. Academy of Sciences*, 2007, vol. 104, pp. 20708 - 20712.
- [10] J. Shim, L. F. Olguin, G. Whyte, D. Scott, A. Babbie, C. Abell, W. T. S. Huck, and F. Hollfelder, "Simultaneous determination of gene expression and enzymatic activity in individual bacterial cells in microdroplet compartments," *J. Am. Chem. Soc.*, vol. 131, no. 42, pp. 15251-15256, Oct. 2009.
- [11] J. Park, T. Bansal, M. Pinelis, and M. M. Maharbiz, "A microsystem for sensing and patterning oxidative microgradients during cell culture," *Lab Chip*, vol. 6, no. 5, pp. 611-622, Mar. 2006.
- [12] L. Mazutis, J. C. Baret, P. Treacy, Y. Skhiri, A. F. Araghi, M. Ryckelynck, V. Taly, and A. D. Griffiths, "Multi-step microfluidic droplet processing: kinetic analysis of an in vitro translated enzyme," *Lab Chip*, vol. 9, no. 9, pp. 2902-2908, Aug. 2009.
- [13] L. Mazutis, J. C. Baret, and A. D. Griffiths, "A fast and efficient microfluidic system for highly selective one-to-one droplet fusion," *Lab Chip*, vol. 9, no. 18, pp. 2665-2672, Jun. 2009.
- [14] C. L. Hansen, E. Skordalakes, J. M. Berger, and S. R. Quake, "A robust and scalable microfluidic metering method that allows protein crystal growth by free interface diffusion," in *Proc. Nat. Academy of Sciences*, 2002, vol. 99, pp. 16531-16536.
- [15] M. Murphy, D. Park, M. Hupert, M. Witek, B. You, P. Datta, J. Guy, J. B. Lee, S. Soper, and D. Nikitopoulos, "A titer plate-based polymer microfluidic

platform for high throughput nucleic acid purification,” *Biomed. Microdevices*, vol. 10, no. 1, pp. 21-33, Feb. 2008.

[16] Y. Schaerli, R. C. Wootton, T. Robinson, V. Stein, C. Dunsby, M. A. A. Neil, P. M. W. French, A. J. de Mello, C. Abell, and F. Hollfelder, “Continuous-flow polymerase chain reaction of single-copy DNA in microfluidic microdroplets,” *Anal. Chem.*, vol. 81, no. 1, pp. 302-306, Jan. 2009.

[17] L. Xie, S. C. Chong, C. S. Premachandran, M. Chew, and U. Raghavan, “Development of an integrated bio-microfluidic package with micro-valves and reservoirs for a DNA lab on a chip (LOC) application,” in *56th Proc. Electronic Components and Technology Conf.*, San Diego, CA, 2006, pp. 693-698.

[18] O. Stoevesandt, M. J. Taussig, and M. He, “Protein microarrays: high-throughput tools for proteomics,” *Expert Review of Proteomics*, vol. 6, no. 2, pp. 145-157, Apr. 2009.

[19] R. J. Meagher, Y. K. Light, and A. K. Singh, “Rapid, continuous purification of proteins in a microfluidic device using genetically-engineered partition tags,” *Lab Chip*, vol. 8, no. 4, pp. 527-532, Feb. 2008.

[20] B. Zheng, J. D. Tice, and R. F. Ismagilov, “Formation of arrayed droplets by soft lithography and two-phase fluid flow, and application in protein crystallization,” *Adv. Mater.*, vol. 16, no. 15, pp. 1365–1368, Aug. 2004.

[21] L. Mazutis, A. F. Araghi, O. J. Miller, J. C. Baret, L. Frenz, A. Janoshazi, V. Taly, B. J. Miller, J. B. Hutchison, D. Link, A. D. Griffiths, and M. Ryckelynck, “Droplet-based microfluidic systems for high-throughput single DNA molecule isothermal amplification and analysis,” *Anal. Chem.*, vol. 81, no. 12, pp. 4813-4821, Jun. 2009.

[22] S. Haeberle and R. Zengerle, “Microfluidic platforms for lab-on-a-chip applications,” *Lab Chip*, vol. 7, no. 9, pp. 1094–1110, Sep. 2007.



- [23] S. Hata, T. Yasuda, and Y. Nakashima, "Blood plasma separation and extraction from a minute amount of blood using dielectrophoretic and capillary forces," *Sensor. Actuat. B-Chem.*, vol. 145, no. 1, pp. 561-569, Dec. 2010.
- [24] J. S. Edgar, C. P. Pabbati, R. M. Lorenz, M. He, G. S. Fiorini, and D. T. Chiu, "Capillary electrophoresis separation in the presence of an immiscible boundary for droplet analysis," *Anal. Chem.*, vol. 78, no. 19, pp. 6948-6954, Oct. 2006.
- [25] W. Y. Lin, Y. H. Lin, and G. B. Lee, "Continuous micro-particle separation using optically-induced dielectrophoretic forces," in *22nd Int. Conf. Micro Electro Mechanical Systems*, Sorrento, Italy, 2009, pp. 47-50.
- [26] C. Iliescu, G. Xu, E. Barbarini, M. Avram, and A. Avram, "Microfluidic device for continuous magnetophoretic separation of white blood cells," *Microsyst. Technol.*, vol. 15, no. 8, pp. 1157-1162, Aug. 2009.
- [27] H. Becker, N. Hlawatsch, C. Carstens, R. Klemm, and C. Gartner, "Continuous-flow PCR using segmented flow and integrating sample preparation," in *Proc. SPIE*, San Jose, CA, 2009, p. 72070J.
- [28] L. Wei, Z. Zhujun, and Y. Liu, "Chemiluminescence microfluidic chip fabricated in PMMA for determination of benzoyl peroxide in flour," *Food Chem.*, vol. 95, no. 4, pp. 693-698, Apr. 2006.
- [29] V. Srinivasan, V. K. Pamula, and R. B. Fair, "Droplet-based microfluidic lab-on-a-chip for glucose detection," *Anal. Chim. Acta*, vol. 507, no. 1, pp. 145-150, Apr. 2004.
- [30] M. A. Unger, H. P. Chou, T. Thorsen, A. Scherer, S. R. Quake, "Monolithic microfabricated valves and pumps by multilayer soft lithography," *Science*, vol. 288, no. 5463, pp. 113-116, Apr. 2000.
- [31] F. Saeki, J. Baum, H. Moon, J. Y. Yoon, C. J. Kim, and R. L. Garrell, "Electrowetting on dielectrics (EWOD): reducing voltage requirements for microfluidics," *Polym. Mater. Sci. Eng.*, vol. 85, pp. 12-13, Jan. 2001.

- [32] M. G. Pollack, R. B. Fair, and A. D. Shenderov, "Electrowetting-based actuation of liquid droplets for microfluidic applications," *Appl. Phys. Lett.*, vol. 77, no. 11, pp. 1725-1726, Sep. 2000.
- [33] J. Ducree, S. Haeberle, S. Lutz, S. Pausch, F. von Stetten, and R. Zengerle, "The centrifugal microfluidic bio-disk platform," *J. Micromech. Microeng.*, vol. 17, no. 7, pp. S103-S115, Jul. 2007.
- [34] D. C. Duffy, H. L. Gillis, J. Lin, N. F. Sheppard, and G. J. Kellogg, "Microfabricated centrifugal microfluidic systems: characterization and multiple enzymatic assays," *Anal. Chem.*, vol. 71, no. 20, pp. 4669-4678, Oct. 1999.
- [35] L. Riegger, M. Grumann, J. Steigert, S. Lutz, C. P. Steinert, C. Mueller, J. Viertel, O. Prucker, J. Ruhe, R. Zengerle, and J. Ducree, "Single-step centrifugal hematocrit determination on a 10- $\mu$  processing device," *Biomed. Microdevices*, vol. 9, no. 6, pp. 795-799, May 2007.
- [36] T. Thorsen, S. J. Maerkl, S. R. Quake, "Microfluidic large-scale integration," *Science*, vol. 298, no. 5593, pp. 580-584, Oct. 2002.
- [37] W. H. Grover, A. M. Skelley, C. N. Liu, E. T. Lagally, and R. A. Mathies, "Monolithic membrane valves and diaphragm pumps for practical large-scale integration into glass microfluidic devices," *Sensor. Actuat. B-Chem*, vol. 89, no. 3, pp. 315-323, Apr. 2003.
- [38] B. T. C. Lau, C. A. Baitz, X. P. Dong, and C. L. Hansen, "A complete microfluidic screening platform for rational protein crystallization," *J. Am. Chem. Soc.*, vol. 129, no. 3, pp. 454-455, Jan. 2007.
- [39] S. Zeng, B. Li, X. Su, J. Qin, and B. Lin, "Microvalve-actuated precise control of individual droplets in microfluidic devices," *Lab Chip*, vol. 9, no. 10, pp. 1340-1343, Mar. 2009.

- [40] C. A. Rich and K. D. Wise, "A high-flow thermopneumatic microvalve with improved efficiency and integrated state sensing," *J. Microelectromech. S.*, vol. 12, no. 2, pp. 201-208, Apr. 2003.
- [41] J. K. Robertson and K. D. Wise, "A nested electrostatically-actuated microvalve for an integrated microflow controller," in *Proc. IEEE Workshop on Micro Electro Mechanical Systems*, Oiso, Japan, 1994, pp. 7-12.
- [42] J. Sutanto, "An electromagnetic actuated microvalve fabricated on a single wafer," Ph.D. dissertation, Mech. Eng. Dept., Georgia Tech., Atlanta, GA, 2004.
- [43] I. Fazal and M. C. Elwenspoek, "Design and analysis of a high pressure piezoelectric actuated microvalve," *J. Micromech. Microeng.*, vol. 17, no. 11, pp. 2366-2379, Oct. 2007.
- [44] J. C. McDonald, D. C. Duffy, J. R. Anderson, D. T. Chiu, H. Wu, O. J. A. Schueller, and G. M. Whitesides, "Fabrication of microfluidic systems in poly (dimethylsiloxane)," *Electrophoresis*, vol. 21, no.1, pp. 27-40, Jan. 2000.
- [45] P. Jothimuthu, A. Carroll, A. A. S. Bhagat, G. Lin, J. E. Mark, and I. Papautsky, "Photodefinable PDMS thin films for microfabrication applications," *J. Micromech. Microeng.*, vol. 19, no. 4, p. 045024, Apr. 2009.
- [46] A. A. S. Bhagat, P. Jothimuthu, and I. Papautsky, "Photodefinable polydimethylsiloxane (PDMS) for rapid lab-on-a-chip prototyping," *Lab Chip*, vol. 7, no. 9, pp. 1192-1197, Jun. 2007.
- [47] Y. S. Shin, K. Cho, S. H. Lim, S. Chung, S. J. Park, C. Chung, D. C. Han, and J. K. Chang, "PDMS-based micro PCR chip with parylene coating," *J. Micromech. Microeng.*, vol. 13, no. 5, pp. 768-774, Sep. 2003.
- [48] S. Sawano, K. Naka, A. Werber, H. Zappe, and S. Konishi, "Sealing method of PDMS as elastic material for MEMS," in *21st Int. Conf. Micro Electro Mechanical Systems*, Tucson, AZ, 2008, pp. 419-422.

- [49] E. Miller and E. Leighton, "Swelling of Parylene C," *J. Elastom. Plast.*, vol. 22, no. 1, pp. 46 -57, Jan. 1990.
- [50] J. S. Bintoro, P. J. Hesketh, and Y. H. Berthelot, "CMOS compatible bistable electromagnetic microvalve on a single wafer," *Microelectron. J.*, vol. 36, no. 7, pp. 667-672, Jul. 2005.
- [51] R. Luharuka and P. J. Hesketh, "A bistable electromagnetically actuated rotary gate microvalve," *J. Micromech. Microeng.*, vol. 18, no. 3, p. 035015, Mar. 2008.
- [52] J. Sutanto, P. J. Hesketh, and Y. H. Berthelot, "Design, microfabrication and testing of a CMOS compatible bistable electromagnetic microvalve with latching/unlatching mechanism on a single wafer," *J. Micromech. Microeng.*, vol. 16, no. 2, pp. 266-275, Feb. 2006.
- [53] A. Doll, M. Wischke, H. J. Schrag, A. Geipel, F. Goldschmidtboeing, and P. Woias, "Characterization of active silicon microvalves with piezoelectric membrane actuators," *Microelectron. Eng.*, vol. 84, no. 5, pp. 1202-1206, May 2007.
- [54] H. Kim, C. In, G. Yoon, and J. Kim, "A slim type microvalve driven by PZT films," *Sensor. Actuat. A-Phys.*, vol. 121, no. 1, pp. 162-171, May 2005.
- [55] R. H. Liu, J. Bonanno, J. Yang, R. Lenigk, and P. Grodzinski, "Single-use, thermally actuated paraffin valves for microfluidic applications," *Sensor. Actuat. B-Chem.*, vol. 98, no. 2, pp. 328-336, Mar. 2004.
- [56] P. Selvaganapathy, E. T. Carlen, and C. H. Mastrangelo, "Electrothermally actuated inline microfluidic valve," *Sensor. Actuat. A-Phys.*, vol. 104, no. 3, pp. 275-282, May 2003.
- [57] H. Takao, K. Miyamura, H. Ebi, M. Ashiki, K. Sawada, and M. Ishida, "A MEMS microvalve with PDMS diaphragm and two-chamber configuration of thermo-pneumatic actuator for integrated blood test system on silicon," *Sensor. Actuat. A-Phys.*, vol. 119, no. 2, pp. 468-475, Apr. 2005.

- [58] B. Yang and Q. Lin, "A latchable microvalve using phase change of paraffin wax," *Sensor. Actuat. A-Phys.*, vol. 134, no. 1, pp. 194-200, Feb. 2007.
- [59] J. C. Yoo, Y. J. Choi, C. J. Kang, and Y. S. Kim, "A novel polydimethylsiloxane microfluidic system including thermopneumatic-actuated micropump and paraffin-actuated microvalve," *Sensor. Actuat. A-Phys.*, vol. 139, no. 1, pp. 216-220, Sep. 2007.
- [60] T. Bansal, M. P. Chang, and M. M. Maharbiz, "A class of low voltage, elastomer metal wet actuators for use in high-density microfluidics," *Lab Chip*, vol. 7, no. 2, pp. 164-166, Dec. 2007.
- [61] W. van der Wijngaart, H. Ask, P. Enoksson, and G. Stemme, "A high-stroke, high-pressure electrostatic actuator for valve applications," *Sensor. Actuat. A-Phys.*, vol. 100, no. 2, pp. 264-271, Sep. 2002.
- [62] L. Yobas, M. A. Huff, F. J. Lisy, and D. M. Durand, "A novel bulk micromachined electrostatic microvalve with a curved-compliant structure applicable for a pneumatic tactile display," *J. Microelectromech. S.*, vol. 10, no. 2, pp. 187-196, Jun. 2001.
- [63] J. Xie, J. Shih, and Y. C. Tai, "Integrated surface-micromachined mass flow controller," in *16th Int. Conf. Micro Electro Mechanical Systems*, Kyoto, Japan, 2003, pp. 20- 23.
- [64] M. P. Chang and M. M. Maharbiz, "Electrostatically-driven elastomer components for user-reconfigurable high density microfluidics," *Lab Chip*, vol. 9, no. 9, pp. 1274-1281, Feb. 2009.
- [65] A. Luque, J. M. Quero, C. Hibert, P. Flückiger, A. M. G. Calvo, "Integrable silicon microfluidic valve with pneumatic actuation," *Sensor. Actuat. A-Phys.*, vol. 118, no. 1, pp. 144-151, Jan. 2005.

- [66] K. Hosokawa and R. Maeda, "A pneumatically-actuated three-way microvalve fabricated with polydimethylsiloxane using the membrane transfer technique," *J. Micromech. Microeng.*, vol. 10, no. 3, pp. 415-420, Sep. 2000.
- [67] Z. Hua, O. Srivannavit, Y. Xia, and E. Gulari, "A compact chemical-resistant microvalve array using parylene membrane and pneumatic actuation," in *Proc. Int. Conf. MEMS, Nano and Smart Systems*, Alberta, Canada, 2004, pp. 72-76.
- [68] J. S. Go and S. Shoji, "A disposable, dead volume-free and leak-free in-plane PDMS microvalve," *Sensor. Actuat. A-Phys.*, vol. 114, no. 2, pp. 438-444, Sep. 2004.
- [69] K. W. Oh and C. H. Ahn, "A review of microvalves," *J. Micromech. Microeng.*, vol. 16, no. 5, pp. R13-R39, May 2006.
- [70] K. Yoshida, M. Kikuchi, J. H. Park, and S. Yokota, "Fabrication of micro electro-rheological valves (ER valves) by micromachining and experiments," *Sensor. Actuat. A-Phys.*, vol. 95, no. 2, pp. 227-233, Jan. 2002.
- [71] A. Ezkerra, L. J. Fernandez, K. Mayora, and J. M. R. Lopez, "A microvalve for lab-on-a-chip applications based on electrochemically actuated SU8 cantilevers," *Sensor. Actuat. B-Chem.*, vol. 155, no. 2, pp. 505-511, Jul. 2011.
- [72] E. Meng, X. Q. Wang, H. Mak, and Y. C. Tai, "A check-valved silicone diaphragm pump," in *13th Int. Conf. Micro Electro Mechanical Systems*, Miyazaki, Japan, 2000, pp. 62-67.
- [73] M. Hu, H. Du, S. F. Ling, Y. Fu, Q. Chen, L. Chow, and B. Li, "A silicon-on-insulator based micro check valve," *J. Micromech. Microeng.*, vol. 14, no. 3, pp. 382-387, Mar. 2004.
- [74] B. Yang and Q. Lin, "Planar micro-check valves exploiting large polymer compliance," *Sensor. Actuat. A-Phys.*, vol. 134, no. 1, pp. 186-193, Feb. 2007.

- [75] P. J. Chen, D. C. Rodger, M. S. Humayun, and Y. C. Tai, "Floating-disk parylene microvalve for self-regulating biomedical flow controls," in *21st Int. Conf. Micro Electro Mechanical Systems*, Tucson, AZ, 2008, pp. 575-578.
- [76] A. Gliere and C. Delattre, "Modeling and fabrication of capillary stop valves for planar microfluidic systems," *Sensor. Actuat. A-Phys.*, vol. 130, pp. 601-608, Aug. 2006.
- [77] H. Cho, H. Y. Kim, J. Y. Kang, and T. S. Kim, "How the capillary burst microvalve works," *J. Colloid Interf. Sci.*, vol. 306, no. 2, pp. 379-385, Feb. 2007.
- [78] T. Gerlach, "Microdiffusers as dynamic passive valves for micropump applications," *Sensor. Actuat. A-Phys.*, vol. 69, no. 2, pp. 181-191, Aug. 1998.
- [79] H. Andersson, W. van der Wijngaart, P. Nilsson, P. Enoksson, and G. Stemme, "A valveless diffuser micropump for microfluidic analytical systems," *Sensor. Actuat. B-Chem.*, vol. 72, no. 3, pp. 259-265, Feb. 2001.
- [80] I. Izzo, D. Accoto, A. Menciassi, L. Schmitt, and P. Dario, "Modeling and experimental validation of a piezoelectric micropump with novel no-moving-part valves," *Sensor. Actuat. A-Phys.*, vol. 133, no. 1, pp. 128-140, Jan. 2007.
- [81] D. E. Angelescu. *Highly integrated microfluidics design*. Norwood, MA: Artech House, 2011, pp. 61-68.
- [82] H. Takao, K. Miyamura, H. Ebi, M. Ashiki, K. Sawada, and M. Ishida, "A MEMS microvalve with PDMS diaphragm and two-chamber configuration of thermo-pneumatic actuator for integrated blood test system on silicon," *Sensor. Actuat. A-Phys.*, vol. 119, no. 2, pp. 468-475, Apr. 2005.
- [83] X. Yang, C. Grosjean, and Y. C. Tai, "A low power MEMS silicone/parylene valve," in *Solid-State Sensor and Actuator Workshop*, Hilton Head, SC, 1998, pp. 316-319.

- [84] E. T. Carlen and C. H. Mastrangelo, "Surface micromachined paraffin-actuated microvalve," *J. Microelectromech. S.*, vol. 11, no. 5, pp. 408-420, Oct. 2002.
- [85] P. Dubois, B. Guldemann, M. A. Gretillat, and N. F. de Rooij, "Electrostatically actuated gas microvalve based on a Ta-Si-N membrane," in *14th Int. Conf. Micro Electro Mechanical Systems*, Interlaken, Switzerland, 2001, pp. 535-538.
- [86] J. A. Potkay and K. D. Wise, "An electrostatically latching thermopneumatic microvalve with closed-loop position sensing," in *18th Int. Conf. Micro Electro Mechanical Systems*, Miami, FL, 2005, pp. 415-418.
- [87] K. S. Ryu, X. Wang, K. Shaikh, E. Goluch, P. Mathias, and C. Liu, "Design and prototyping of a surface micromachined parylene microvalve with hybrid actuation scheme: on-chip thermopneumatic initiation and electrostatic latching," in *9th Int. Conf. Miniaturized Systems for Chemistry and Life Sciences*, Boston, MA, 2005, pp. 9-13.
- [88] T. L. Sounart, T. A. Michalske, and K. R. Zavadil, "Frequency-dependent electrostatic actuation in microfluidic MEMS," *J. Microelectromech. S.*, vol. 14, no. 1, pp. 125-133, Feb. 2005.
- [89] N. T. Nguyen, "Micropumping and microvalving," in *Methods in Bioengineering: Biomicrofabrication and Biomicrofluidics*. J. D. Zahn Ed., Artech House, 2010, p. 34.
- [90] A. S. Rollier, B. Legrand, D. Collard, and L. Buchaillot, "The stability and pull-in voltage of electrostatic parallel-plate actuators in liquid solutions," *J. Micromech. Microeng.*, vol. 16, no. 4, pp. 794-801, Apr. 2006.
- [91] Multiphysics Solutions from MSC.Software, Last access date: 5 Sep. 2011. Available from: <http://www.mscsoftware.com/Solutions/Applications/Multiphysics.aspx>



- [92] ANSYS Multiphysics Software for Engineering Analysis, Last access date: 5 Sep. 2011. Available from: <http://www.ansys.com/Products/Simulation+Technology/Multiphysics/ANSYS+Multiphysics>
- [93] Multiphysics Modeling and Simulation Software COMSOL, Last access date: 5 Sep. 2011. Available from: <http://www.comsol.com/>
- [94] A. Eriksson, "Mechanical Model of Electrostatically Actuated Shunt Switch.", in *COMSOL Multiphysics User's Conf.*, Stockholm, Sweden, 2005.
- [95] J. R. Gilbert, G. K. Ananthasuresh, and S. D. Senturia, "3D modeling of contact problems and hysteresis in coupled electromechanics," in *Proc. 9th Int. Workshop Micro Electro Mechanical Systems*, San Diego, CA, 1996, pp. 127-132.
- [96] L. A. Rocha, E. Cretu, and R. F. Wolffenbuttel, "Analysis and analytical modeling of static pull-in with application to MEMS-based voltage reference and process monitoring," *J. Microelectromech. S.*, vol. 13, no. 2, pp. 342-354, Apr. 2004.
- [97] J. Wang, *Analytical Electrochemistry*. Hoboken, NJ: John Wiley and Sons, 2006, p. 21.
- [98] N. Tas, T. Sonnenberg, H. Jansen, R. Legtenberg, and M. Elwenspoek, "Stiction in surface micromachining," *J. Micromech. Microeng.*, vol. 6, no. 4, pp. 385-397, Dec. 1996.
- [99] Specialty Coating Systems, Parylene properties, Last access date: 05 Sep. 2011. Available from: [http://www.scscoatings.com/parylene\\_knowledge/specifications.aspx](http://www.scscoatings.com/parylene_knowledge/specifications.aspx)
- [100] T. P. Weihs, S. Hong, J. C. Bravman, and W. D. Nix, "Mechanical deflection of cantilever microbeams: a new technique for testing the mechanical properties of thin films," *J. Mater. Res.*, vol. 3, no. 5, pp. 931-942, Sep. 1988.
- [101] P. F. Man, D. K. Jones, and C. H. Mastrangelo, "Microfluidic plastic capillaries on silicon substrates: a new inexpensive technology for bioanalysis

chips,” in *Proc. 10th Annu. Int. Workshop on Micro Electro Mechanical Systems*, Nagoya, Japan, 1997, pp. 311-316.

[102] K. Walsh, J. Norville, and Y. C. Tai, “Photoresist as a sacrificial layer by dissolution in acetone,” in *14th Int. Conf. Micro Electro Mechanical Systems*, Interlaken, Switzerland, 2001, pp. 114-117.

[103] W. H. Ko and Q. Wang, “Touch mode capacitive pressure sensors,” *Sensor. Actuat. A-Phys.*, vol. 75, no. 3, pp. 242-251, Jun. 1999.

[104] S. Timoshenko and S. Woinowsky-Krieger, *Theory of plates and shells*. New York: McGraw Hill, 1959, p. 414.

[105] W. Young, R. Budynas, and A. Sadegh, *Roark's Formulas for Stress and Strain*, 7th ed. New York: McGraw Hill, 2002, pp. 427-525.

[106] S. Y. Teh, R. Lin, L. H. Hung, and A. P. Lee, “Droplet microfluidics,” *Lab Chip*, vol. 8, no. 2, pp. 198-220, Jan. 2008.

[107] L. Shui, J. C. T. Eijkel, and A. van den Berg, “Multiphase flow in micro and nanochannels,” *Sensor. Actuat. B-Chem.*, vol. 121, no. 1, pp. 263-276, Jan. 2007.

[108] K. V. Sharp and R. J. Adrian, “Transition from laminar to turbulent flow in liquid filled microtubes,” *Exp. Fluids*, vol. 36, no. 1, pp. 741-747, Feb. 2004.

[109] B. Zheng, J. D. Tice, and R. F. Ismagilov, “Formation of droplets of alternating composition in microfluidic channels and applications to indexing of concentrations in droplet-based assays,” *Anal. Chem.*, vol. 76, no. 17, pp. 4977-4982, Sep. 2004.

[110] B. Zheng, L. S. Roach, and R. F. Ismagilov, “Screening of protein crystallization conditions on a microfluidic chip using nanoliter-size droplets,” *J. Am. Chem. Soc.*, vol. 125, no. 37, pp. 11170-11171, Sep. 2003.

- [111] J. F. Edd, D. D. Carlo, K. J. Humphry, S. Köster, D. Irimia, D. A. Weitz, and M. Toner, "Controlled encapsulation of single-cells into monodisperse picolitre drops," *Lab Chip*, vol. 8, no. 8, pp. 1262-1264, Aug. 2008.
- [112] Z. Han, W. Li, Y. Huang, and B. Zheng, "Measuring rapid enzymatic kinetics by electrochemical method in droplet-based microfluidic devices with pneumatic valves," *Anal. Chem.*, vol. 81, no. 14, pp. 5840-5845, Jul. 2009.
- [113] Y. Liu, S. Y. Jung, and C. P. Collier, "Shear-driven redistribution of surfactant affects enzyme activity in well-mixed femtoliter droplets," *Anal. Chem.*, vol. 81, no. 12, pp. 4922-4928, Jun. 2009.
- [114] S. Mohr, Y. H. Zhang, A. Macaskill, P. J. R. Day, R. W. Barber, N. J. Goddard, D. R. Emerson, and P. R. Fielden, "Numerical and experimental study of a droplet-based PCR chip," *Microfluid. Nanofluid.*, vol. 3, no. 5, pp. 611-621, Feb. 2007.
- [115] F. Wang and M. A. Burns, "Performance of nanoliter-sized droplet-based microfluidic PCR," *Biomed. Microdevices*, vol. 11, no. 5, pp. 1071-1080, May 2009.
- [116] H. Boukellal, S. Selimovic, Y. Jia, G. Cristobal, and S. Fraden, "Simple, robust storage of drops and fluids in a microfluidic device," *Lab Chip*, vol. 9, no. 2, pp. 331-338, Oct. 2008.
- [117] C. W. Lai, Y. H. Lin, and G. B. Lee, "A microfluidic chip for formation and collection of emulsion droplets utilizing active pneumatic micro-choppers and micro-switches," *Biomed. Microdevices*, vol. 10, no. 5, pp. 749-756, Oct. 2008.
- [118] S. Zeng, B. Li, X. Su, J. Qin, and B. Lin, "Microvalve-actuated precise control of individual droplets in microfluidic devices," *Lab Chip*, vol. 9, no. 10, pp. 1340-1343, Mar. 2009.
- [119] P. S. Dittrich and A. Manz, "Lab-on-a-chip: microfluidics in drug discovery," *Nat. Rev. Drug Discov.*, vol. 5, no. 3, pp. 210-218, Mar. 2006.

- [120] K. H. R. Tkaczuk, N. S. Tait, O. Ioffe, M. Tan, O. G. Goloubeva, S. A. Lesko, S. F. Deamond, D. Zhou, Z. P. Lum, M. J. Sutula, D. V. Echo, and P. O. P. Tso, "Computer assisted quantitative immunofluorescence of tumor tissue marker expression and clinical outcome to chemotherapy in advanced breast cancer patients," *Discov. Med.*, vol. 12, no. 62, pp. 33-40, Jul. 2011.
- [121] H. Wang, J. Kim, A. Jayaraman, M. Cypert, J. Hua, M. Bittner, and A. Han, "A high-throughput fully-automated microfluidic live cell array for combination drug treatment analysis of colorectal cancer cells," in *16th Int. Solid-State Sensors, Actuators and Microsystems Conf.*, Beijing, China, 2011, pp. 2148-2151.
- [122] Polysciences Inc., Polybead® Microspheres 3.00µm, Last access date: 05 Sep. 2011. Available from: [http://www.polysciences.com/Catalog/Department/Product/98/categoryId\\_\\_373/productId\\_\\_824/](http://www.polysciences.com/Catalog/Department/Product/98/categoryId__373/productId__824/)
- [123] Dow Corning Corp., XIAMETER Product Detail, Last access date: 05 Sep. 2011. Available from: <https://www.xiameter.com/EN/Products/Pages/ProductDetail.aspx?pid=01013165&lir=X73>
- [124] H. Song, M. R. Bringer, J. D. Tice, C. J. Gerdtts, and R. F. Ismagilov, "Experimental test of scaling of mixing by chaotic advection in droplets moving through microfluidic channels," *Appl. Phys. Lett.*, vol. 83, no. 12, p. 4664-4666, Dec. 2003.

# APPENDIX A

## MASK LAYOUTS

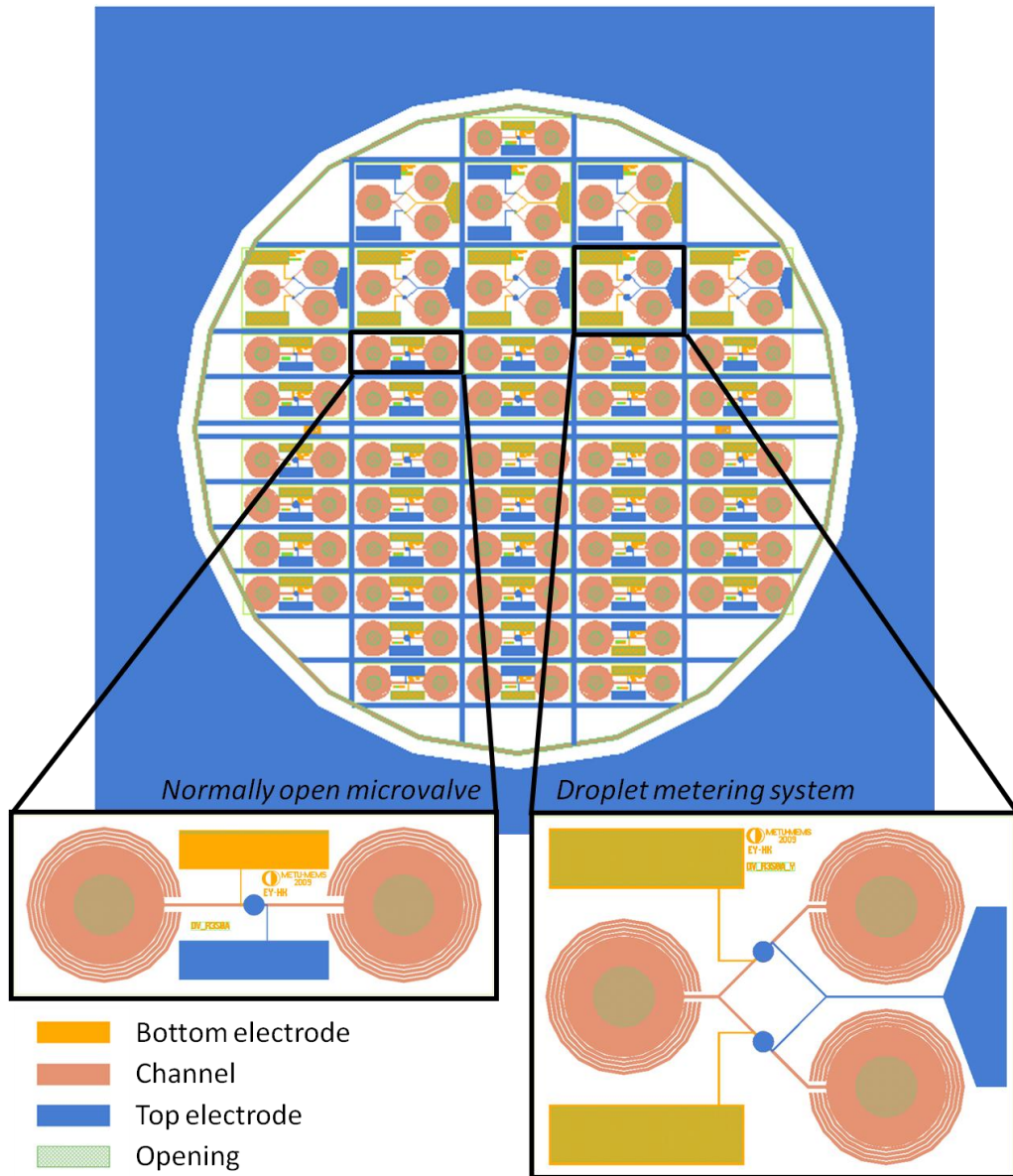


**Figure A. 1: Mask layout for fabrication of normally open electrostatic microvalves and droplet metering systems on 4" radius substrate.**

**Table A.1: Definition of the masks used in fabrication of normally open microvalves.**

	<b>Mask Name</b>	<b>Type</b>	<b>Notes</b>
1.	Bottom electrode	Clear field	Used for metallization of bottom electrodes
2.	Channel	Clear field	Used for fabrication of microchannels, reservoirs, and valve diaphragms
3.	Top electrode	Clear field	Used for metallization of top electrodes
4.	Opening	Dark field	Used for etching parylene on top of the reservoirs and electrical contact pads

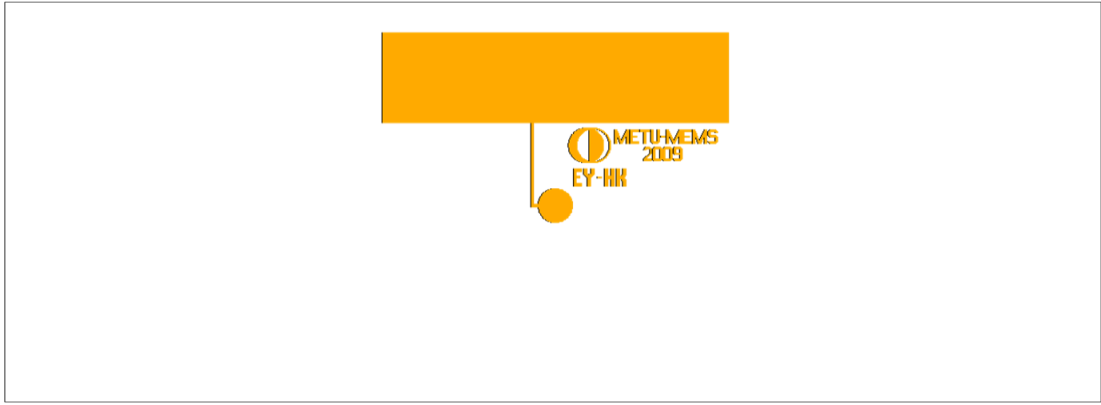


**Figure A.2: Bottom electrode mask layout for normally open electrostatic microvalves.**

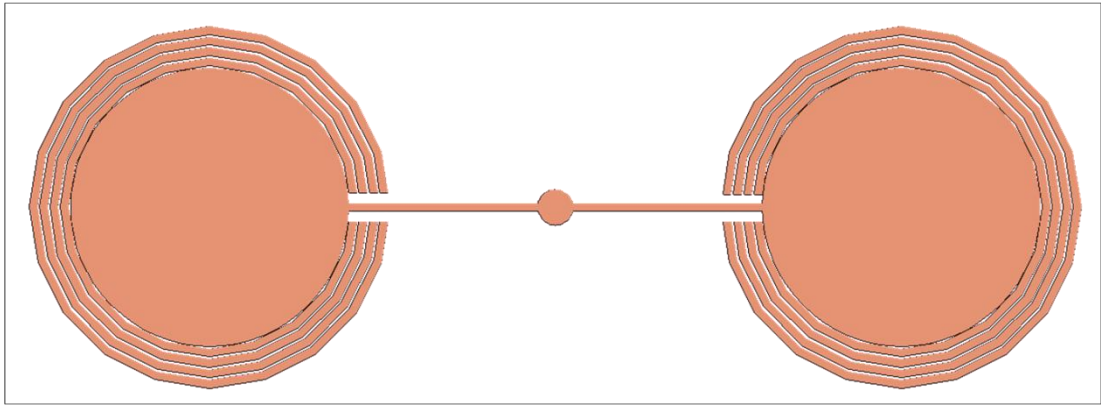


**Figure A.3: Channel mask layout for normally open electrostatic microvalves.**

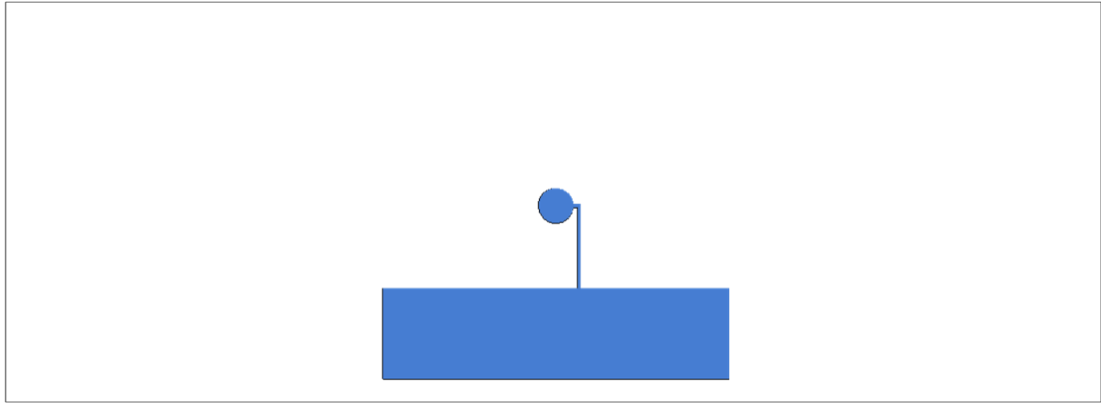


**Figure A.4: Top electrode mask layout for normally open electrostatic microvalves.**

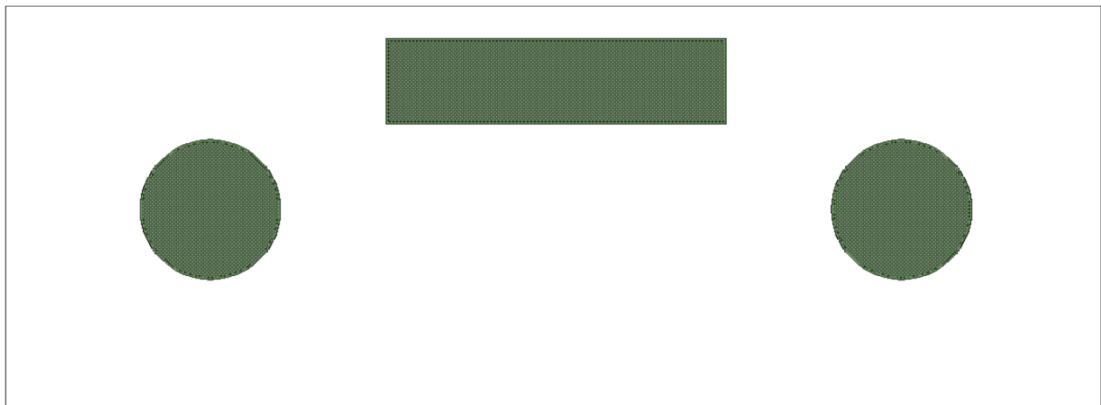


**Figure A.5: Opening mask layout for normally open electrostatic microvalves.**



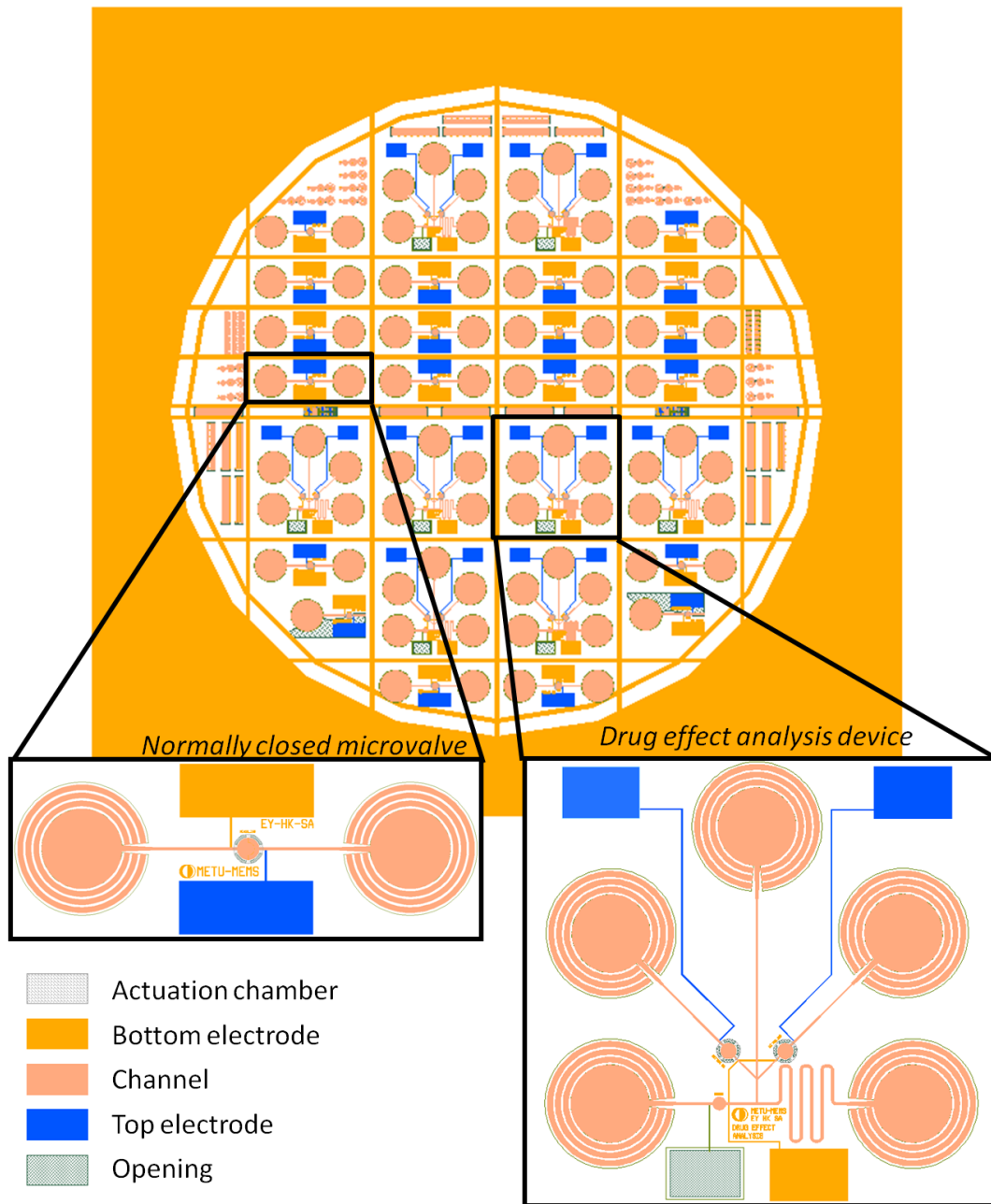


**Figure A.6: Mask layout for fabrication of normally closed electrostatic microvalves and droplet metering systems on 4" radius substrate.**

**Table A.2: Definition of the masks used in fabrication of normally closed microvalves.**

	<b>Mask Name</b>	<b>Type</b>	<b>Notes</b>
1.	Actuation chamber	Clear field	Used for fabrication of the actuation chambers
2.	Bottom electrode	Clear field	Used for metallization of bottom electrodes
3.	Channel	Clear field	Used for fabrication of microchannels, reservoirs, and valve diaphragms
4.	Top electrode	Clear field	Used for metallization of top electrodes
5.	Opening	Dark field	Used for etching parylene on top of the reservoirs and electrical contact pads

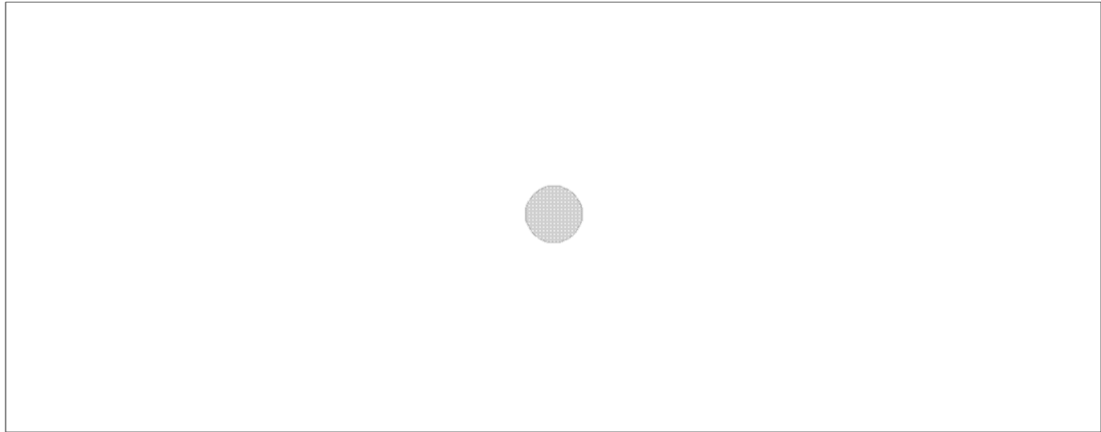


**Figure A.7: Actuation chamber mask layout for normally closed electrostatic microvalves.**



**Figure A.8: Bottom electrode mask layout for normally closed electrostatic microvalves.**

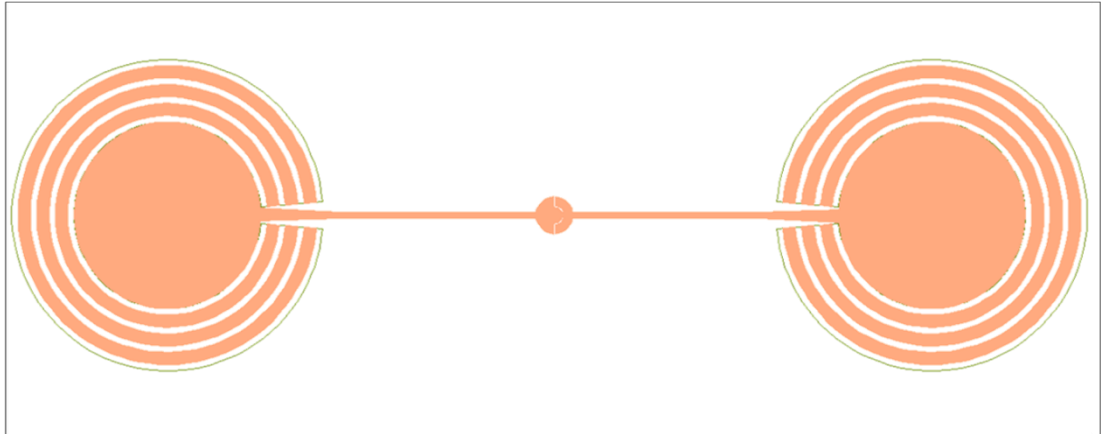


**Figure A.9: Channel mask layout for normally closed electrostatic microvalves.**

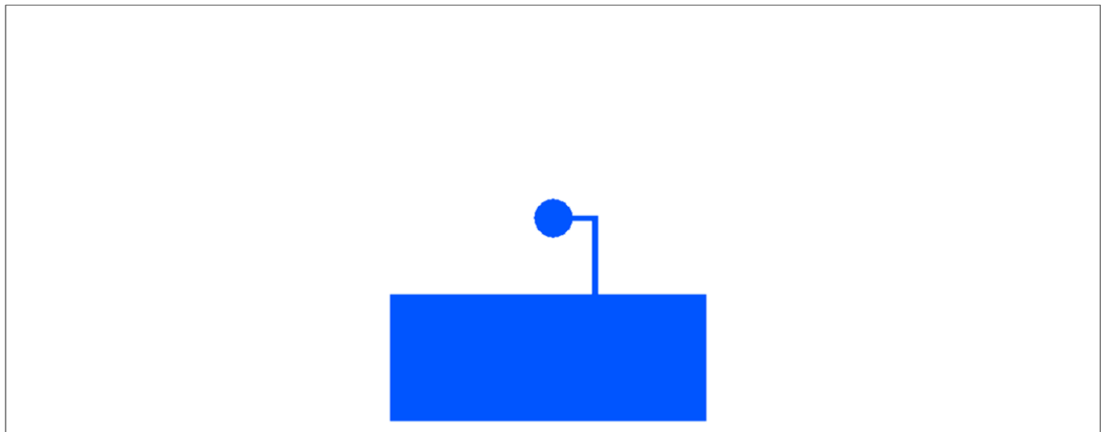


**Figure A.10: Top electrode mask layout for normally closed electrostatic microvalves.**

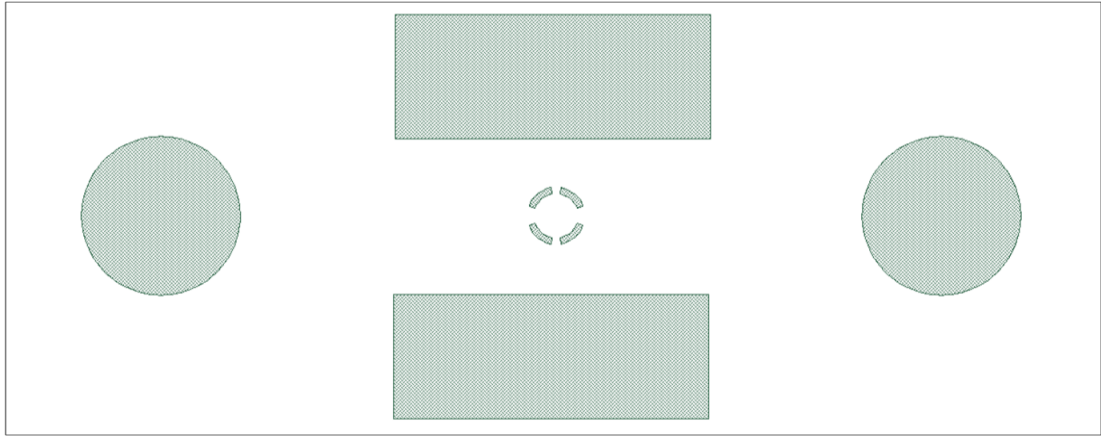


**Figure A.11: Opening mask layout for normally closed electrostatic microvalves.**

## APPENDIX B

### FABRICATION PROCESS RECIPES

**Table B.1: Process recipes for fabrication of normally open electrostatic microvalves.**

1.	Bottom Electrode Metallization  Mask: Bottom Electrode, clear field	<ul style="list-style-type: none"><li>a. 3 <math>\mu\text{m}</math> of parylene deposition using A174 silane</li><li>b. Sputter 20 nm Ti, 200 nm Au at 300 W.</li><li>c. Spin HMDS at 1000 rpm for 30 sec.</li><li>d. Spin S1813 at 4000 rpm for 30 sec.</li><li>e. Soft bake for 70 sec. on 115°C hot plate</li><li>f. Expose using bottom electrode mask for 7 sec. at 12 mW/sec</li><li>g. Develop for 70 sec. using MF319.</li><li>h. Rinse twice for 60 sec. each using DI-water.</li><li>i. N<sub>2</sub> dry</li><li>j. Inspect</li><li>k. Etch Au, using Transene gold etchant for 2:30 min.</li><li>l. Rinse</li><li>m. Etch Ti, using 100:5 diluted Ti etchant (8:1:1 H<sub>2</sub>O:HF:H<sub>2</sub>O<sub>2</sub>)</li><li>n. Rinse</li><li>o. N<sub>2</sub> dry</li><li>p. Inspect</li><li>q. Strip photoresist using acetone</li></ul>
----	---	---

**Table B.1: Process recipes for fabrication of normally open electrostatic microvalves.  
(continued)**

		<ul style="list-style-type: none"> <li>r. N<sub>2</sub> dry</li> <li>s. Inspect</li> </ul>
2.	<p>Microchannel formation</p> <p>Mask: Channel, clear field</p>	<ul style="list-style-type: none"> <li>a. Dehydration at 90°C for 10 min.</li> <li>b. Cooling under N<sub>2</sub> flow.</li> <li>c. Spin HMDS at 1000 rpm for 30 sec.</li> <li>d. Spin SPR220-3 at 2000 rpm for 30 sec.</li> <li>e. Soft bake for 70 sec. on 115°C hot plate</li> <li>f. Expose using channel mask for 12 sec. at 12 mW/sec</li> <li>g. Develop for 70 sec. using MF24-A.</li> <li>h. Rinse twice for 60 sec. each using DI-water.</li> <li>i. N<sub>2</sub> dry</li> <li>j. Inspect</li> <li>k. Keep in vacuum less than 30 mTorr for 1 hr.</li> <li>l. Hard bake at 110°C for 3 hrs (ramp starting from room temperature)</li> <li>m. Cooling under N<sub>2</sub> flow.</li> <li>n. 3 μm of parylene deposition (without silane)</li> </ul>
3.	<p>Top electrode metallization</p> <p>Mask: Top electrode, clear field</p>	<ul style="list-style-type: none"> <li>a. Sputter 20 nm Ti, 100 nm Au at 75 W.</li> <li>b. Spin HMDS at 1000 rpm for 30 sec.</li> <li>c. Spin SPR220-3 at 2000 rpm for 30 sec.</li> <li>d. Soft bake for 70 sec. on 115°C hot</li> </ul>

**Table B.1: Process recipes for fabrication of normally open electrostatic microvalves.  
(continued)**

		<p>plate</p> <p>e. Expose using bottom electrode mask for 12 sec. at 12 mW/sec</p> <p>f. Develop for 70 sec. using MF24-A.</p> <p>g. Rinse twice for 60 sec. each using DI-water.</p> <p>h. N<sub>2</sub> dry</p> <p>i. Inspect</p> <p>j. Etch Au, using Transene gold etchant for 2:30 min.</p> <p>k. Rinse</p> <p>l. Etch Ti, using 100:5 diluted Ti etchant (8:1:1 H<sub>2</sub>O:HF:H<sub>2</sub>O<sub>2</sub>)</p> <p>m. Rinse</p> <p>n. N<sub>2</sub> dry</p> <p>o. Inspect</p> <p>p. Strip photoresist using acetone</p> <p>q. N<sub>2</sub> dry</p> <p>r. Inspect</p>
4.	<p>Formation of reservoir and contact pad openings</p> <p>Mask: Opening, dark field</p>	<p>a. Dehydration at 90°C for 10 min.</p> <p>b. Cooling under N<sub>2</sub> flow.</p> <p>c. Spin HMDS at 1000 rpm for 30 sec.</p> <p>d. Spin SPR220-7 at 2000 rpm for 30 sec.</p> <p>e. Soft bake for 70 sec. on 115°C hot plate</p> <p>f. Expose using opening mask for 45 sec. at 12 mW/sec</p> <p>g. Develop for 70 sec. using MF24-A.</p>



**Table B.1: Process recipes for fabrication of normally open electrostatic microvalves.  
(continued)**

		<ul style="list-style-type: none"> <li>h. Rinse twice for 60 sec. each using DI-water.</li> <li>i. N<sub>2</sub> dry</li> <li>j. Inspect</li> <li>k. Hard bake at 90°C for 20 min. (ramp starting from room temperature)</li> <li>l. RIE under O<sub>2</sub> and CF<sub>4</sub> flow for 15 min.</li> <li>m. Inspect</li> </ul>
5.	Release of the prototypes	<ul style="list-style-type: none"> <li>a. Dicing</li> <li>b. Immerse dies in still acetone, wait for 1 day.</li> <li>c. Sequential IPA, methanol treatment.</li> <li>d. Vaporize methanol on 60°C hot plate.</li> </ul>

**Table B.2: Process recipes for fabrication of normally closed microvalves.**

<p>1.</p>	<p>Fabrication of the actuation chamber</p> <p>Mask: Actuation chamber, clear field</p>	<p>a. Dehydration at 90°C for 10 min.</p> <p>b. Cooling under N<sub>2</sub> flow.</p> <p>c. Spin HMDS at 1000 rpm for 30 sec.</p> <p>d. Spin AZ 5214 at 4000 rpm for 30 sec.</p> <p>e. Prebake for 60 sec. on 115°C hot plate</p> <p>f. Expose using actuation chamber mask for 7 sec. at 12 mW/sec</p> <p>g. Post exposure bake for 2 min. on 120°C hot plate (critical)</p> <p>h. Flood expose for 15 sec. at 12 mW/sec (image reversal).</p> <p>i. Develop for 70 sec. using MF319.</p> <p>j. Rinse twice for 60 sec. each using DI-water.</p> <p>k. N<sub>2</sub> dry</p> <p>l. Inspect</p> <p>m. Final bake for 3 min. on 120°C hot plate</p> <p>n. 1 μm of parylene deposition (with silane).</p> <p>o. Inspect using profiler.</p>
<p>2.</p>	<p>Bottom Electrode Metallization</p> <p>Mask: Bottom Electrode, clear field</p>	<p>a. Sputter 20 nm Ti, 200 nm Au at 300 W (target distance is 130 mm).</p> <p>b. Spin HMDS at 1000 rpm for 30 sec.</p> <p>c. Spin S1813 at 2000 rpm for 30 sec.</p> <p>d. Soft bake for 70 sec. on 115°C hot plate</p>

**Table B.2: Process recipes for fabrication of normally closed microvalves.  
(continued)**

		<ul style="list-style-type: none"> <li>e. Expose using bottom electrode mask for 8 sec. at 12 mW/sec</li> <li>f. Develop for 70 sec. using MF319.</li> <li>g. Rinse twice for 60 sec. each using DI-water.</li> <li>h. N<sub>2</sub> dry</li> <li>i. Inspect</li> <li>j. Etch Au, using Transene gold etchant for 2:30 min.</li> <li>k. Rinse</li> <li>l. Etch Ti, using 100:5 diluted Ti etchant (8:1:1 H<sub>2</sub>O:HF:H<sub>2</sub>O<sub>2</sub>)</li> <li>m. Rinse</li> <li>n. N<sub>2</sub> dry</li> <li>o. Inspect</li> <li>p. Strip photoresist using acetone</li> <li>q. N<sub>2</sub> dry</li> <li>r. Inspect</li> </ul>
3.	<p>Filling of actuation chamber</p> <p>Mask: Actuation chamber</p>	<ul style="list-style-type: none"> <li>a. Dehydration at 90°C for 10 min.</li> <li>b. Cooling under N<sub>2</sub> flow.</li> <li>c. Spin HMDS at 1000 rpm for 30 sec.</li> <li>d. Spin SPR220-7 at 4000 rpm for 30 sec.</li> <li>e. Soft bake for 70 sec. on 115°C hot plate</li> <li>f. Expose using channel mask for 45 sec. at 12 mW/sec with vacuum contact.</li> <li>g. Develop for 70 sec. using MF24-A.</li> </ul>

**Table B.2: Process recipes for fabrication of normally closed microvalves.  
(continued)**

		<ul style="list-style-type: none"> <li>h. Rinse twice for 60 sec. each using DI-water.</li> <li>i. N<sub>2</sub> dry</li> <li>j. Inspect</li> <li>k. Keep in vacuum less than 30 mTorr for 1 hr.</li> <li>l. Hard bake at 110°C for 3 hrs (ramp starting from room temperature)</li> <li>m. Cooling under N<sub>2</sub> flow.</li> <li>n. 2.5 μm of parylene deposition (without silane)</li> </ul>
4.	<p>Top electrode metallization</p> <p>Mask: Top electrode, clear field</p>	<ul style="list-style-type: none"> <li>a. Sputter 20 nm Ti, 100 nm Au at 75 W.</li> <li>b. Spin HMDS at 1000 rpm for 30 sec.</li> <li>c. Spin S1813 at 2000 rpm for 30 sec.</li> <li>d. Soft bake for 70 sec. on 115°C hot plate</li> <li>e. Expose using bottom electrode mask for 8 sec. at 12 mW/sec</li> <li>f. Develop for 70 sec. using MF319.</li> <li>g. Rinse twice for 60 sec. each using DI-water.</li> <li>h. N<sub>2</sub> dry</li> <li>i. Inspect</li> <li>j. Etch Au, using Transene gold etchant for 2:30 min.</li> <li>k. Rinse</li> <li>l. Etch Ti, using 100:5 diluted Ti etchant (8:1:1 H<sub>2</sub>O:HF:H<sub>2</sub>O<sub>2</sub>)</li> </ul>

**Table B.2: Process recipes for fabrication of normally closed microvalves.**  
(continued)

		<ul style="list-style-type: none"> <li>m. Rinse</li> <li>n. N<sub>2</sub> dry</li> <li>o. Inspect</li> <li>p. Strip photoresist using acetone</li> <li>q. N<sub>2</sub> dry</li> <li>r. Inspect</li> <li>s. 1 μm insulating parylene deposition (without silane)</li> </ul>
5.	<p>Microchannel formation</p> <p>Mask: Channel, clear field</p>	<ul style="list-style-type: none"> <li>a. Dehydration at 90°C for 10 min.</li> <li>b. Cooling under N<sub>2</sub> flow.</li> <li>c. Spin HMDS at 1000 rpm for 30 sec.</li> <li>d. Spin SPR220-7 at 1500 rpm for 30 sec.</li> <li>e. Soft bake for 70 sec. on 115°C hot plate</li> <li>f. Expose using channel mask for 55 sec. at 12 mW/sec</li> <li>g. Develop for 70 sec. using MF24-A.</li> <li>h. Rinse twice for 60 sec. each using DI-water.</li> <li>i. N<sub>2</sub> dry</li> <li>j. Inspect</li> <li>k. 10 μm of parylene deposition (without silane)</li> </ul>
6.	<p>Formation of reservoir and contact pad openings</p> <p>Mask: Opening, dark field</p>	<ul style="list-style-type: none"> <li>a. Dehydration at 90°C for 10 min.</li> <li>b. Cooling under N<sub>2</sub> flow.</li> <li>c. Spin HMDS at 750 rpm for 30 sec.</li> <li>d. Spin AZ9260 at 750 rpm for 30 sec.</li> <li>e. Pre bake for 3 min. on 110°C hot</li> </ul>

**Table B.2: Process recipes for fabrication of normally closed microvalves.  
(continued)**

		<p>plate.</p> <p>f. 15 min. of relaxation in horizontal cassette.</p> <p>g. Edge bead removal at 1000 rpm.</p> <p>h. Soft bake in 90 °C oven for 60 min. (ramp starting from room temperature.)</p> <p>i. Rehydration for 1 hr in vapor of 9 ml water in wafer cassette.</p> <p>j. Expose using opening mask for 45 sec. at 12 mW/sec</p> <p>k. Develop for 30 min. using AZ826-MIF developer.</p> <p>l. Rinse twice for 60 sec. each using DI-water.</p> <p>m. N<sub>2</sub> dry</p> <p>n. Inspect</p> <p>o. RIE under O<sub>2</sub> and CF<sub>4</sub> flow for 45 min. (20 min. + 15 min. + 10 min.)</p> <p>p. Inspect</p>
7.	Release of the prototypes	<p>a. Dicing</p> <p>b. Immerse dies in still acetone, wait for 1 day.</p> <p>c. Sequential IPA, methanol treatment.</p> <p>d. Vaporize methanol on 60°C hot plate.</p>

# CURRICULUM VITAE

## PERSONAL INFORMATION

**Surname, Name:** Yıldırım, Ender

**Nationality:** Turkish (T.C.)

**Date and Place of Birth:** 17 November 1979, Aydın/TURKEY

**Phone:** +90 536 563 8410

**email:** endery@cankaya.edu.tr

## EDUCATION

### **Degree, Institution, Year of Graduation**

M.Sc., Middle East Technical University Mechanical Engineering, 2005

B.Sc., Middle East Technical University Mechanical Engineering, 2002

## WORK EXPERIENCE

### **Year, Place, Enrollment**

2010-..., Cankaya University Mechanical Engineering Department, Instructor

2008-2010, Cankaya University Industrial Engineering Department, Instructor

2004-2008, Cankaya University Industrial Engineering Department, Expert

2002-2004, METU Mechanical Engineering Department, Teaching Assistant

## FOREIGN LANGUAGES

English

## **PUBLICATIONS**

### **Conference Papers**

1. E. Yıldırım, A. Koyuncuođlu, and H. K÷lah, “An electrostatic parylene microvalve for controlling in-plane flow” in *the 13th International Conference on Miniaturized Systems for Chemistry and Life Sciences ( $\mu$ TAS 2009)*, Jeju, Korea, Nov. 2009, pp. 1034-1036.
2. E. Yıldırım, A. Koyuncuođlu, and H. K÷lah, “An electrostatic parylene microvalve for lab-on-a-chip applications,” in *the 15th National Biomedical Engineering Meeting (BIYOMUT)*, Antalya, Apr. 2010, pp. 365–368 (in Turkish).
3. E. Yıldırım, M. A. S. Arıkan, and H. K÷lah, “Design and leakage characterization of a microvalve for parylene based lab-on-a-chip systems”, in *the 4th National Symposium on Engineering and Technology*, Ankara, Apr. 2011, pp. 632-637 (in Turkish).
4. E. Yıldırım, M. A. S. Arıkan, and H. K÷lah, “An electrostatically actuated parylene microvalve for lab-on-a-chip applications,” in *the 16th International Solid-State Sensors, Actuators and Microsystems Conference*, Beijing, China, June 2011, pp. 250-253.

### **Journal Articles**

1. E. Yıldırım and H. K÷lah, “Analysis and characterization of an electrostatically actuated in-plane parylene microvalve”, *J. Micromech. Microeng.*, vol. 21, p. 105009, Oct. 2011.

## **HOBBIES**

Playing and listening music, Painting.